Universität Rostock

Traditio et Innovatio

Physics-based Discrete Modelling and Digital Control Design for Grid-Side Inverters for Renewable Energy

Dissertation
zur
Erlangung des akademischen Grades
Doktor-Ingenieur (Dr.-Ing.)
der Fakultät für Informatik und Elektrotechnik
der Universität Rostock

vorgelegt von
M.Sc. Michael Schütt
aus Rostock

Rostock, 24.06.2022

https://doi.org/10.18453/rosdok_id00004119

1. Gutachter:
   Prof. Dr.-Ing Hans-Günter Eckel
   Institut für Elektrische Energietechnik, Universität Rostock
2. Gutachter:
   Prof. Dr.-Ing Sibylle Dieckerhoff
   Institut für Energie- und Automatisierungstechnik, Technische Universität Berlin

Datum der Einreichung: 24. Juni 2022
Datum der Verteidigung: 10. November 2022

Acknowledgment

I want to take this opportunity first to thank my academic mentors. Already during my studies, Professor Eckel captivated me with his outstanding lectures and won me over to power electronics. This trend continued when he became my boss and direct mentor during my time as a Ph.D. student. He always motivated me and also gave me the necessary freedom to enter and explore new academic paths. Special mention must be made here of my greatest role model in control engineering. Professor Lorenz forever tied me to control engineering during my time at WEMPEC with his unsurpassable lectures. I think I speak for all WEMPECers when I say that we miss you, and your legacy of physics-based control will live on in us - Rest in Peace!

I would also like to thank my colleagues, and good friends from the Department of Power Electronics and Electrical Drives Till-Mathis Plötz, Cord Prignitz, Daniel Lexow, Florian Störmer, Christian Grünbaum, and Christian Neumann. I had a great time with you, and also, the stimulating discussions were always part of this work. I would also like to thank Gyanendra Kumar Sah and Vishwas Acharya Nayampalli. They already played a major role in the experimental setup as students and are now a vital extension of the team.

I would also like to thank distant colleagues at WEMPEC for great memories and an irreplaceable treasure trove of experiences: Seth Avery, Tyler Brauhn, Bryan Dow, Brent Gagas, Tyler Graf, Dan Ludois, Timothy Slininger, Marc Petit, Boru Wang, Teng Wu.

Last but probably most important, I would like to thank my family. Possibly my most outstanding role models − my parents − made all of this possible for me. They put academics in my cradle and spared no expense or effort in guiding me on the right path. In the same sense, I thank my brother, who was always with me and supported me during all my stays abroad, and always visited me. However, my most significant support in life is my beloved better half, Alina. She is always there for me and fills me with love. She also gave me my precious son Colin, who brings so much joy into our lives.

Abstract

This work lays out the methodology of the analysis and consequent control design for the LC filter application on the example of a 5 MW wind turbine. The chapters progress sequentially through the different complexity steps from the continuous analysis to the discrete-space modeling to control algorithm design, integrated into a microcontroller-based hardware setup. The methods in each complexity step illustrate the process, starting with the identification of the control issue, through the control solutions, and ending with the evaluation using dynamic analysis.

This paper presents a coherent method for direct discrete modeling of the LC plant. The developed models are the basis for the z-domain control design with active damping and observer structures used to compensate for the system's delays. The simulation results are evaluated via a low-voltage test bench at the University of Rostock. The experimental chapter presents the scaling process and the limits of such low-voltage test benches.

The problem of active damping via capacitor current feedback is straightforward and benign in the continuous space. However, the discrete space presents many additional challenges such as delays, the inability to modulate continuous signals, and the warped z-domain space that alters eigenvalue placements. The proposed strategies tackle these challenges and exhibit similar dynamic properties compared to the continuous reference.

Zusammenfassung

In dieser Arbeit wird die Methodik der Analyse und des anschließenden Regelungsentwurfs für die LC-Filteranwendung am Beispiel einer 5 MW Windturbine dargelegt. Die Kapitel führen nacheinander durch die verschiedenen Komplexitätsstufen von der kontinuierlichen Analyse über die Modellierung im diskreten Raum bis hin zum Entwurf des Regelalgorithmus, der in eine mikrocontrollerbasierte Hardware integriert ist. Die Methoden in jedem Komplexitätsschritt veranschaulichen den Prozess, beginnend mit der Identifizierung des Regelungsproblems, über die Regelungslösungen und endend mit der Bewertung mittels dynamischer Analyse.

In diesem Beitrag wird eine kohärente Methode zur direkten diskreten Modellierung der LC-Anlage vorgestellt. Die entwickelten Modelle bilden die Grundlage für den Regelungsentwurf im Z-Bereich mit aktiver Dämpfung und Beobachterstrukturen, die zur Kompensation der Systemverzögerungen eingesetzt werden. Die Simulationsergebnisse werden mit Hilfe eines Niederspannungsprüfstandes an der Universität Rostock ausgewertet. Das experimentelle Kapitel stellt den Skalierungsprozess und die Grenzen solcher Niederspannungsprüfstände dar.

Das Problem der aktiven Dämpfung durch Kondensatorstromrückführung ist im kontinuierlichen Raum einfach und unproblematisch. Der diskrete Raum stellt jedoch viele zusätzliche Herausforderungen dar, wie z. B. Verzögerungen, die Unfähigkeit, kontinuierliche Signale zu modulieren, und der verzerrte z-Bereich, der die Eigenwertplatzierungen verändert. Die vorgeschlagenen Strategien meistern diese Herausforderungen und weisen ähnliche dynamische Eigenschaften auf wie die kontinuierliche Referenz.

Author

Michael Schütt received the B.Sc. and the M.Sc. degrees in electrical engineering from the University of Rostock, Rostock, Germany, in 2011 and 2014, respectively.

From October 2011 to January 2012, he was a Visiting Researcher at the University of Limerick, Limerick, Ireland. He did his research for his B.Sc. degree at the Victoria University of Wellington, Wellington, New Zealand, in the spring of 2012 funded by the ICI ECP. From September 2013 to April 2014, he conducted his research for his M.Sc. degree at the University of Wisconsin, Madison, USA. He was a DAAD-promoted Visiting Scholar at the University of Wisconsin, Madison, USA, from August 2015 to May 2016.

Since 2015, he has been a research assistant and doctoral candidate at the Institute of Electrical Power Engineering at the University of Rostock, Rostock, Germany. His topics of interest include control systems, digital signal processing, power semiconductors, and inverter technology for drives and energy conversion. He is one of the co-founders of the company *Rostocker Kompetenzzentrum für Leistungselektronik* (2022).

Table of Contents

List of Figures

List of Abbreviations

AC	Alternating Current
AD	Active Damping
CT	Command Tracking
CCSFb	Cross-Coupling State Feedback
DCCSFb	Decoupling Cross-Coupling State Feedback
DSFb	Decoupling State Feedback
DIC	Disturbance Input Coupling
DID	Disturbance Input Decoupling
DC	Direct Current
DS	Dynamic Stiffness
DSP	Digital Signal Processor
EV	Eigenvalue
FPGA	Field Programmable Gate Array
FRF	Frequency Response Function
FwP	Forward-Path
IGBT	Insulated-Gate Bipolar Transistor
MOSFET	Metal Oxide Semiconductor Field-Effect Transistor)
MIC	Manipulated Input Coupling
MID	Manipulated Input Decoupling
P	Proportional (controller)
PI	Proportional-Integral (controller)

PCC	Point of Common Coupling
PT1	first-order lag element
PLL	Phase-Locked Loop
RMS	Root Mean Square
RTF	Ferrite core material
RTN	Nanocrystal core material
RTP	Powder core material
PWM	Pulse-Width Modulation
SFb	State Feedback
ZOH	Zero-Order Hold

List of Symbols

Parameter and Variables

B, $\lvert B \rvert$	Magnitude of the magnetic flux density
C	Capacitor
C_c	First capacitive component of the cable equivalent circuit (Figure 1.1)
C_c'	Second capacitive component of the cable equivalent circuit (Figure 1.1)
C_f	Filter capacitor
δ	zero of the PI-controller
f_{ar} or ω_{ar}	Anti-resonant frequency – in Hz or rad/s, $\omega_{ar} = 2\pi f_{ar} = \sqrt{1/(L_f C_f)}$
f_{br} or ω_{br}	Break frequency/EV in Hz or rad/s
f_{Res} or ω_{Res}	Resonant frequency in Hz or rad/s, $\omega_{Res} = 2\pi f_{Res} = \sqrt{(L_f + L_G)/(L_f L_G C_f)}$
ω_0	Grid Resonant frequency in rad/s $\omega_0^2 = (L_G C_f)^{-1}$
J, $\lvert J \rvert$	Magnitude of the current density
j	Imaginary unit: $j^2 = -1$
K, α, β	Steinmetz parameter: K – proportional component, α – frequency component exponent, β – magnetic field strength component exponent
K	PI-controller overall gain
K_i	Integral gain of a controller
K_p	Proportional gain of a controller
$[k]$	Sampling instance $k - f[k] = f(t = k \cdot T)$
L	Inductance
L_c	First inductance component of the cable equivalent circuit (Figure 1.1)
L_c'	Second inductance component of the cable equivalent circuit (Figure 1.1)
L_c''	Third inductance component of the cable equivalent circuit (Figure 1.1)
L_f	Filter inductance
L_G	Grid inductance
L_t	Transformer inductance
P_{Co}	Copper losses (conductor losses – $P_r + P_s + P_p$)

P_r	Power loss due to pure resistance of the coils (DC)
P_p	Power loss due to proximity effect (AC)
P_s	Power loss due to skin effect (AC)
P_Fe	Iron losses (core losses – P_ed + P_hys)
P_ed	Power loss due to eddy currents in the core (AC)
P_hys	Power loss due to hysteresis effects of the core material (AC)
p_n	poles in the pole-zero plot (x denotes poles in pole-zero plots)
$\hat{R}$, $\hat{L}$, $\hat{C}$	Estimated parameters
R	Resistance
R_f	Filter resistance
R_Co	Equivalent resistance representing the inductor's copper losses
R_Fe	Equivalent resistance representing the inductor's iron losses
R_G	Grid resistance
R_t	Transformer resistance
R_vir	Virtual resistance for active damping
s	Laplace-variable: $s = \sigma + \mathrm{j}\omega$
T	Sampling time
τ	Time constant: inductive load: $\tau_\mathrm{RL} = L/R$; resonant LC-load: $\tau_\mathrm{LC} = \sqrt{LC}$
V_max	Amplitude of voltage signal
ξ	damping coefficient
z_n	poles in the pole-zero plot (o denotes poles in pole-zero plots)
z	z-variable: $z = \mathrm{e}^{T \cdot s}$

Variables and Parameter Definitions for Scaling

A_Fe	Cross-sectional area of the inductor's core of the original wind turbine
$A_\mathrm{Fe,m}$	Cross-sectional area of the inductor's core of the test bench
A_w	Cross-sectional area of the inductor's windings of the original wind turbine
$A_\mathrm{w,m}$	Cross-sectional area of the inductor's windings of the test bench
C	Capacitance of the original wind turbine
C_m	Capacitance of the test bench
δ_B	Magnetic flux density scaling (Figure 6.9)
δ_Fe	Core radius scaling (Figure 6.9)
δ_lFe	Core length scaling (Figure 6.9)
δ_N	Number of windings scaling (Figure 6.9)
δ_w	Conductor radius scaling (Figure 6.9)

δ_x	Iron loss scaling to power scaling ratio (Figure 6.9)
E_C	Nominal stored energy in the capacitor of the original wind turbine
$E_{C\text{-}m}$	Nominal stored energy in the capacitor of the test bench
I_n	Nominal current of the original wind turbine
$I_{n\text{-}m}$	Nominal current of the test bench
i_0	Relative (no-load) capacitive current of the original wind turbine
$i_{0\text{-}m}$	Relative (no-load) capacitive current of the test bench
u	Geometric scaling factor
L	Inductance of the original wind turbine
L_m	Inductance of the test bench
l_w	Length of the inductor's windings of the original wind turbine
$l_{w,m}$	Length area of the inductor's windings of the test bench
λ_ρ	Conductivity ratio (Figure 6.9)
m	Mass of the inductor of the original wind turbine
m_m	Mass of the inductor of the test bench
n_i	Current scaling factor (from test bench to original wind turbine)
n_u	Voltage scaling factor (from test bench to original wind turbine)
P	Nominal power of the original wind turbine
P_m	Nominal power of the test bench
P_{loss}	Nominal power dissipation of the inductor of the original wind turbine
$P_{loss,m}$	Nominal power dissipation of the inductor of the test bench
R	Resistance of the original wind turbine
R_m	Resistance of the test bench
R_{DS}	On-state resistance of the MOSFET (Drain-Source resistance)
S	Nominal apparent Power of the original wind turbine
S_m	Nominal apparent Power of the test bench
u_k	Relative (short-circuit) inductive voltage drop of the original wind turbine
$u_{k\text{-}m}$	Relative (short-circuit) inductive voltage drop of the test bench
V_{CE}	Nominal collector-emitter voltage of the original wind turbine
$V_{DS\text{-}m}$	Nominal drain-source voltage of the test bench
V_n	Nominal voltage of the original wind turbine
$V_{n\text{-}m}$	Nominal voltage of the test bench

Matrices and Coefficients

A_{tn}	Plant coefficients of the discrete-time difference equation of the inverter current (reduced-state vector)
B_{tn}	Plant coefficients of the discrete-time difference equation of the capacitor voltage (reduced-state vector)
C_n	Plant coefficients of the numerator of the open-loop z-transform of the inverter ($I_{inv}(z)/V_{inv}(z)$) with AD of the full-state vector model
D_n	Plant coefficients of the denominator of the open-loop z-transform of the inverter ($I_{inv}(z)/V_{inv}(z)$) with AD of the full-state vector model
$\mathbf{A}$	System matrix in continuous space
$\mathbf{B}_{inv}$	Input matrix in continuous space
$\mathbf{B}_g$	Disturbance matrix in continuous space
$\mathbf{C}_c$	System matrix in continuous and discrete space
$\mathbf{\Phi}$	System matrix in discrete space
ϕ_{nm}	Coefficients of discrete system matrix in discrete space
$\mathbf{\Gamma}_{inv}$	Input matrix in discrete space
ϕ_{invn}	Coefficients of discrete input matrix in discrete space
$\mathbf{\Gamma}_g$	Disturbance Matrix in discrete space
ϕ_{gn}	Coefficients of discrete disturbance matrix in discrete space
H_n	Help/substitution coefficients for the voltage and current difference equation/coefficients A_{tn} and B_{tn} (see Table 4.1)

Functions:

Time domain/frequency domain definitions:

$f(t)$	Function of time (continuous-time space)
$f[k]$	Function of time (discrete-time space)
$F(s)$	Function in frequency domain (continuous Laplace-domain)
$F(z)$	Function in discrete frequency domain
$f^*(t)$	Command/reference

Example:

$v(t)$	Voltage as time signal
$v_{\alpha\beta}(t)$	Voltage in αβ-reference-frame
$v_{dq}(t)$	Voltage in dq-reference-frame

$v_{inv}(t)$	Inverter voltage as time signal
$V_{inv}(s)$	Inverter voltage in frequency domain
$V_{inv}(z)$	Inverter voltage in discrete frequency domain
$i^*_{dq}(t)$	dq-current reference
$i^*_{dq}(t)$	dq-current reference

Functions of Time and Frequency:

$A_n(s)$	Functions of the Laplace-transform of the inverter current equation (reduced state-vector)
$B_n(s)$	Functions of the Laplace-transform of the capacitor voltage equation (reduced state-vector)
$B(t)$	Magnetic field density
$f(t)$ or $\omega(t)$	Frequency in Hz or rad/s
$\hat{F}(s)$	Estimated state information (observer)
$G(s)$	Transfer Function
$G_{PI}(s)$	Transfer Function of the PI-controller
$i(t)$	Current
$i_{inv}(t)$	Inverter current
$i_C(t)$	Capacitor current
$i_G(t)$	Grid current
$v_G(t)$	Grid voltage
$v_{DC}(t)$	DC-link voltage
$v_C(t)$	Capacitor voltage
$\omega_G(t)$	Grid frequency in rad/s

Operators:

$\lvert x \rvert$	Magnitude of x
$< x$	Phase angle of x
$x \propto y$	x is proportional to y
dx/dt	Time derivative of x
$\mathrm{Im}(x)$	Imaginary part of complex variable x
$\mathrm{Re}(x)$	Real part of complex variable x
$e^{\mathbf{A}}$	Matrix exponential of the matrix $\mathbf{A}$

1. Introduction

In March 2014, a fire started on the converter platform BorWin 1 of the wind farm Bard Offshore 1. Consequently, the operators shut down the 400 MW North Sea offshore wind farm for months due to technical problems. The transmission system operator TenneT, the wind farm operator Ocean Breeze, and the converter manufacturer ABB commissioned the independent third-party Task Force to investigate. This platform failure led to a loss of income of up to a three-digit million euro sum. Further, this fiasco raised the question of whether this was a problem in the grid connection or the transmission technology and left the rest of the industry worrying. Officials informed the press that harmonics caused fluctuation in the grid. These fluctuations caused an overload of the substation of BorWin 1. [1, 2]

In [3], TenneT provides an analysis of the harmonics of BorWin 1. TenneT focuses in [3] on the impedance resonances of small islanded offshore grids dominated by cables, converters, and auxiliary systems. The installed lines in the case of BorWin 1 have high capacitance per km. Further, the overall system is very low resistive. This combination leaves powerful resonances within the whole system. The converter hardware and control design had to include these resonant issues to secure stable operation. Unfortunately, this opportunity was missed within the planning phase of BorWin 1 / Bard Offshore.

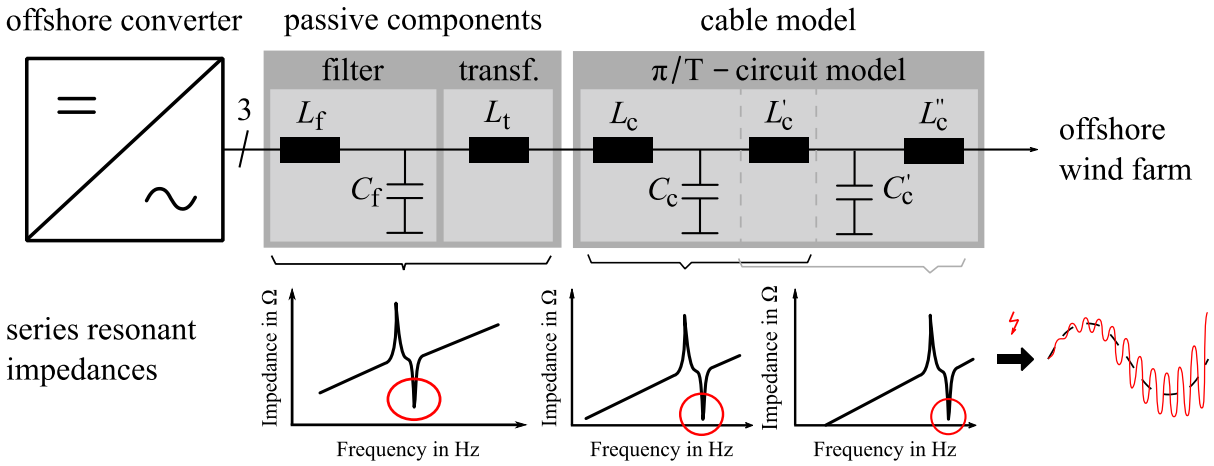

Figure 1.1: Possible resonances within the structure of an offshore wind farm due to various LC components.

Damping

However, resonant-impedance issues are not just a subject of converters connected to island grids. Likewise, onshore wind turbines or photovoltaic plants face similar problems when implementing LC-filters. LC-filters or LCL-filters are second-order low pass filters that achieve grid-code compliant harmonics with smaller passive components and thus cheaper installation costs compared to the first-order L-filter counterpart, with the inductor dominating the overall costs for such systems.

A comprehensive approach to overcoming the associated resonant problem is the usage of damping resistors within the converter output filter [4, 5]. This solution is state of the art for wind turbine converters. A viable scenario and explanation of the BorWin 1 incident are connected to overheating of these damping resistors, causing a chain of destruction. Small voltage excitation of the resonances of the offshore-grid could have induced strong currents through the installed damping resistors causing this overheating issue. In general, such damping resistors have to be separately cooled in some cases, increasing the overall effort.

Moreover, the stress on these resistors is not known for all operational cases, which leaves the potential for severe destructive cases such as the described scenario. The associated grid-impedances that influence the resonance are unknown. Hence the dimensioning becomes precarious. Finally, the dissipated energy in these resistors also reflects a loss of income.

Active Damping

Another promising approach to tackle the LC-resonance issue can be found via control design. Substantial research went into controlling algorithms to overcome the LC-resonance problem [4–18]. These techniques can be divided into two main categories: *State Feedback-based* (SFb-based) [6, 8–11, 13–16, 18] and *Forward-Path-based* (FwP-based) methods [7, 12, 17]. The term *Active Damping* (AD) encompasses all of these methods. Table A.3 (appendix) provides a systematic overview of all these AD papers indicating the type of technique, the utilized state information, and limits of the respective strategies. A summary of the gaps in these references is given in the following subchapter.

The state feedback-based methods utilize information on the inverter current, the grid current, the capacitor current, capacitor voltage, or a combination to manipulate the system's overall behavior. The state information is used to decouple the resonance or to implement a virtual damping coefficient. When decoupling the capacitor voltage, as shown in Figure 1.2.d, the plant seen from the converter becomes a first-order L-filter for the inverter

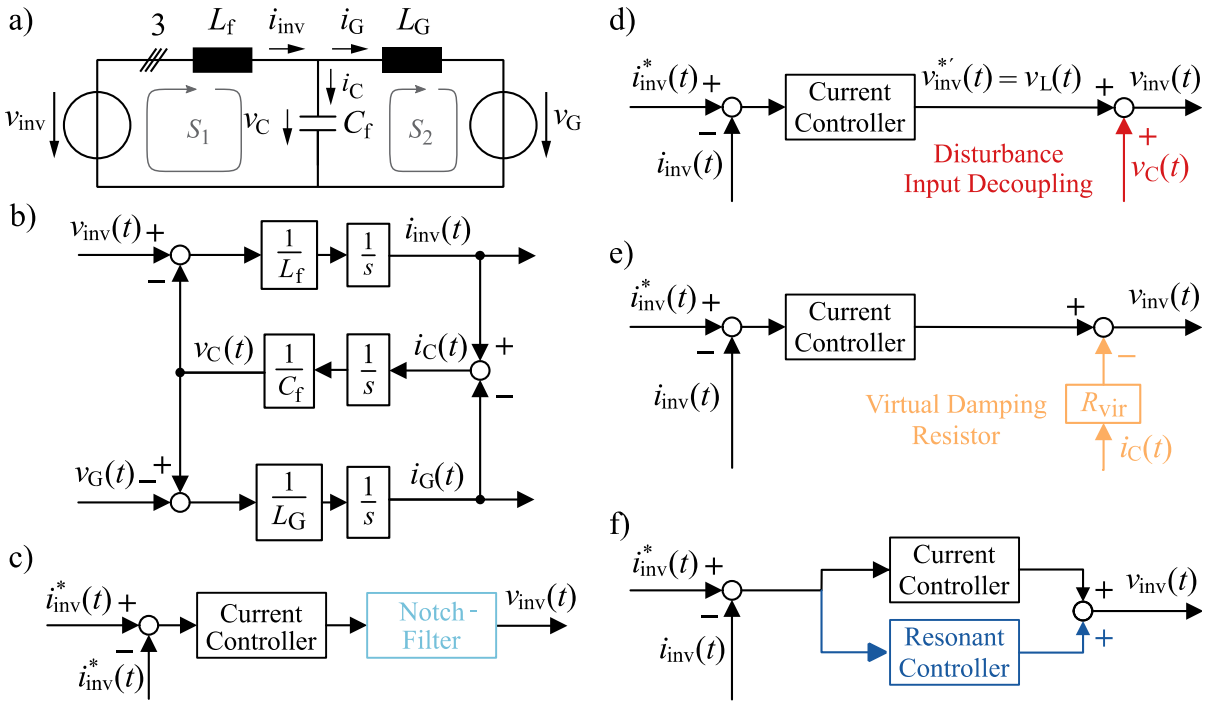

Figure 1.2: Overview of AD algorithms: a) LCL-topology, b) block-diagram of LCL, c) Notch-Filter based AD, d) Voltage-Decoupling based AD, e) virtual impedance damping, f) resonant controller based AD.

current control (loop S_1). Decoupling the capacitor voltage is mathematically the same as a short over the capacitor. Therefore, the capacitor itself, the grid-impedance, and the grid-voltage no longer affect the current control.

Figure 1.2.e, in contrast, uses an active state-feedback of the capacitor current and introduces a virtual resistance similar to a damping resistor. However, this virtual impedance is only modulated in v_{inv}, and thus its influence is only present for loop S_1 and consequently is dynamically not the same as a damping resistor – which would produce a voltage drop in both loops S_1 and S_2.

Both state feedback-based active damping approaches need accurate state information (v_C or i_{inv}) but are intrinsically not very sensitive to grid impedance.

The forward-path-based solutions either implement a notch-filter (Figure 1.2.c) within the controller or introduce a resonant controller (Figure 1.2.f) tuned to the LCL-resonance. These forward-path-based algorithms require accurate estimation of the resonance and, thus, of the grid impedance. Further, the notch-filter-based solution only prevents the converter from exciting the resonance but disables the converter to dampen the resonance once excited. In other words, a notch-filter-based solution provides no input impedance for the

grid at the selected resonant frequency. Thus, the converter will show a strong current reaction when the grid excites at that frequency. On the other hand, the resonant-controller solution will provide a very strong impedance at the selected resonant frequency. However, when the grid-impedance-based resonance changes, the controller offers its high damping impedance at the wrong frequency, failing to dampen the critical oscillations.

The Gap in Literature – Active Damping

As previously discussed, active damping methods need accurate state information or precise information about the load. In the case of an LC-resonance, this information is most crucial at relatively high frequencies. Thus, continuous space control solutions cannot perform adequately on existing systems. A computational delay between sampling and voltage update is inevitable on today's most common *Digital Signal Processor*-based (DSP-based) controller boards. A typical example of 3 kHz wind turbine converters is an LC-filter with a break frequency of around 700 Hz. The computational delay, in this case, can yield a phase of 84 degrees. The approaches of Figure 1.2.d and Figure 1.2.e would not dampen in this case due to the incorrect phase.

Table A.3 in the appendix chapter categorizes the mentioned active damping references and analyzes the remaining gaps in the respective research. In summary, the cited papers fail to provide a coherent method to shape the input impedance of the inverter to dampen resonances in varying grid-impedance situations. Most procedures do not include the discrete nature of a digital PWM-based system and its inherent delay properties. The main focus is solely put on the command tracking attributes for almost all of the studied active damping approaches or, in other words, on the excitation part of the inverter – overlooking the actual damping of the system completely. In contrast, the primary goal should be the input impedance and the robustness regarding the grid-impedance.

The Gap in Literature – PWM

Pulse-Width Modulation-based (PWM-based) converters cannot produce continuous voltage nor discrete step-shaped voltages. Instead, block-shaped voltages are modulated to match the desired voltage in an average manner. This raises the question regarding the dynamic representation of the PWM. A discrete step-shaped voltage is a ZOH. As shown in [19], if sampling and updating are done synchronously with the PWM, the PWM can be modeled as a *Zero-Order Hold* (ZOH), as well (for inductive loads).

Another common approach is the modeling of the PWM as a delay with the length of half a sampling period [20].

Figure 1.3 shows a simple simulation to illustrate the dynamic properties of the PWM. In Figure 1.3 a-e, a digital PWM-based system (ZOH for the A/D-sampling and the PWM itself) tries to negate a reference signal. The output is integrated to evaluate the difference between the two paths on average (a – PWM vs. ZOH, b – PWM vs. continuous, c – PWM with phase correction vs. continuous dynamically), d – PWM vs. delayed continuous, e – PWM vs. delayed continuous dynamically).

Figure 1.3 shows that the mentioned delay representation of the PWM falsely represents the system dynamics. On average, the PWM signal does not introduce a phase (Figure 1.3.a) that would be present for that proposed delay approach. When comparing a continuous signal with a discrete PWM representation, i.e., during voltage decoupling, the PWM can only match the continuous signal on average. Delaying the continuous signal by half a

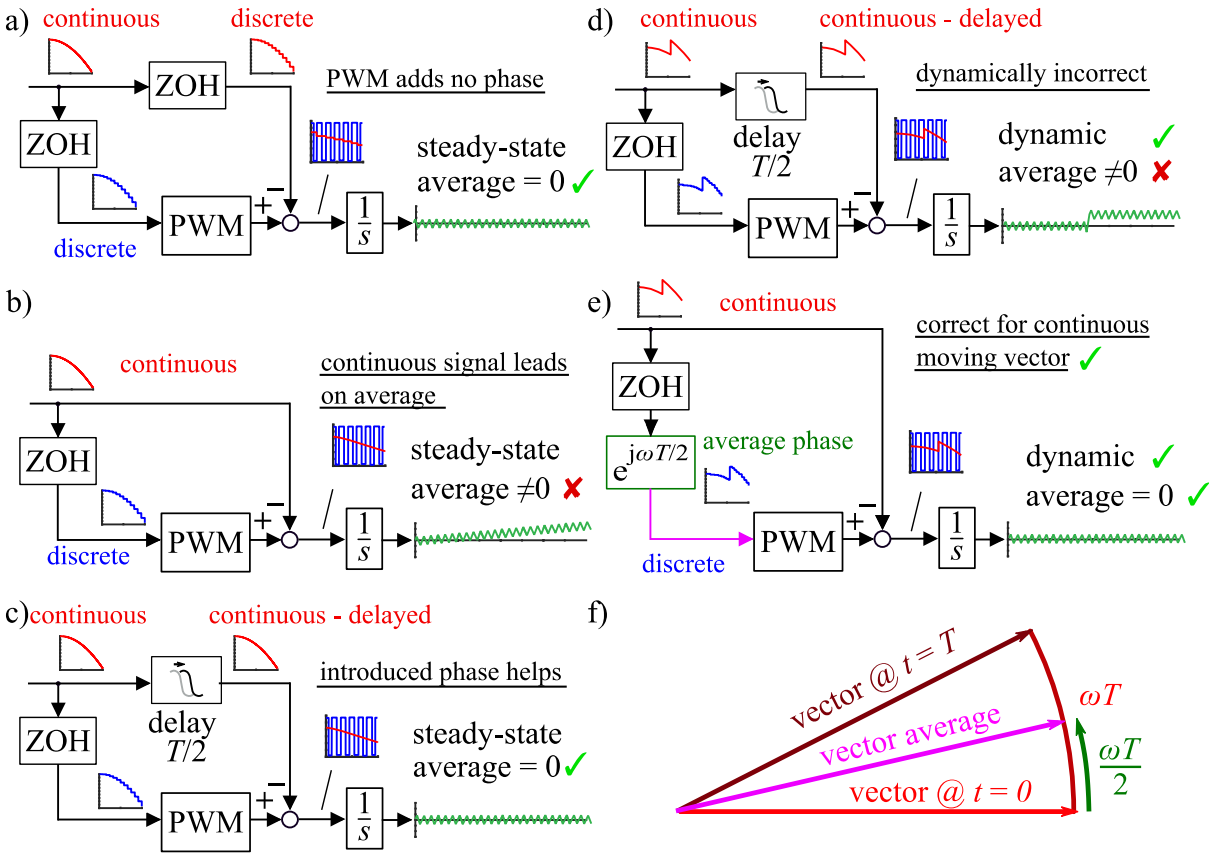

Figure 1.3: Comparison of PWM modelling techniques for different events: (a) discrete PWM represented by a zero-order hold (ZOH), (b) difference of discrete PWM to continuous signal, (c) average-based discrete PWM compared to continuous signal at dynamic event, (d) delay representation of PWM with sinusoidal signal compared to continuous case, (e) delay representation of PWM with sinusoidal signal at dynamic event compared to continuous case, (f) vector average of sinusoidal signal.

sampling period results in an average match for the case of a perfect sinusoidal signal (Figure 1.3.c) and thus might lead to the erroneous assumption to model the PWM as a delay. Figure 1.3.a shows in isolation that the PWM itself does not introduce any phase to the discretized signal on average.

Figure 1.3.f illustrates the moving vector of the continuous signal between samples (starting at $t = 0$ in red to $t = T$ in brown). The average of this moving vector is between the sampled values of the continuous signal (indicated in pink). Consequently, the PWM input should be set to the vector average (pink) rather than the sample instant values (red or brown) to decouple the continuous moving vector (on average). The vector average is obtained for a sinusoidal signal by increasing the angle by $\omega T/2$, as shown in Figure 1.3.e.

A dynamic event illustrates the difference between modeling the PWM as a delay of half a sampling period (Figure 1.3.d) or just as a zero-order hold and introducing average signal math for decoupling techniques (Figure 1.3.e). The continuous moving vector leads the sampled vector between each sampling point and thus creating the illusion of a delay caused by the PWM. However, the erroneous delay model of the PWM still leads to the correct phase correction for the decoupling of continuous signals – such as the decoupling of the grid voltage of grid-connected inverters. On the other hand, this phase correction is also applied very commonly to the discrete signals of the current control. This false applied phase correction can lead to dynamic problems.

The Gap in Literature – Discrete Modelling

To overcome the limitation of the continuous space, approximation models such as Tustin or Forward Euler are commonly used to achieve discrete system models [21]. These approximation models are accurate only to a certain extent. Especially in high frequencies relative to the sampling frequency, as is the case for most grid resonances, these approximation models fail to represent the system attributes accurately, as shown in the simulation example of Figure 1.4.

The Gap in Literature – Summary and Goals

To handle the LC-problem effectively, a cohesive direct discrete model-based solution has to be found. Further, a coherent solution for delay compensation is essential. Comparing state feedback-based and forward-path-based solutions, the state feedback-based solutions provide a more practical method due to their robustness regarding the grid impedance information.

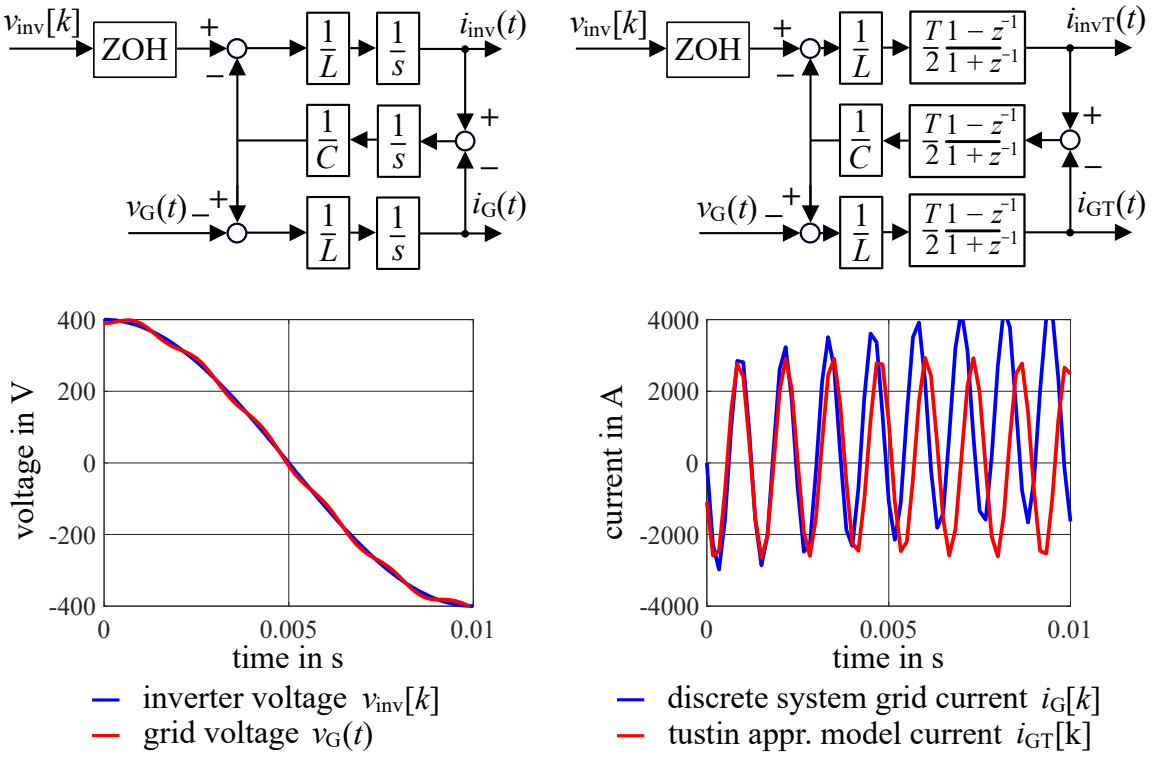

Figure 1.4: Comparison of the discrete voltage source system dynamics: *Up-Left*: Reference-model in continuous time with zero-order hold ("discrete system"), *Up-Right*: Discrete plant model with the Tustin approximation; *Bottom-Left*: Grid voltage and inverter voltage time plot for both models; *Bottom-Right*: Resulting sampled grid currents for the two models.

Outline

This work will outline a consistent analytical approach to achieving the previously set goals. Some parts of the presented material were already published in [22–25]. Further, this paper consecutively presents the different complexity levels and the related control problems from a continuous design to an implementation-space design on a DSP for the LC-filter problem. A 5 MW wind turbine with a 3 kHz converter is used as an example. All parameters are provided in Table A.1 (Appendix). A down-scaled version of the said converter is designed and presented as an experimental setup.

The introduction outlines the LC resonance problem and highlights its significance in the example of the BorWin 1 incident. This chapter further summarizes the current state of literature and outlines an analysis regarding the literature gaps as a fundamental basis of this work.

Chapter 2 presents the general control design and evaluation methods used in this paper. This chapter briefly describes pole-zero placement techniques and the matrices used to evaluate command tracking capability, disturbance rejection, and robustness. This chapter further emphasizes the importance of designing the disturbance rejection attributes such that the converter resembles a dynamically well-behaved impedance seen from the grid. The described state-of-the-art of current control solutions and the general concepts of the methods and metrics are closely oriented toward the references [19, 26]. The related publications to this work [22, 23, 25] reveal additional insights on problems of the state-of-the-art solutions and are showcased in chapter 2, as well. These issues mainly concern harmonic impedance resonant effects caused by forward-path-based solutions. The chapter offers possible solutions both in continuous and discrete space.

Chapter 3 outlines the definition of the control problem, continuous modeling, and control design. The methods shown in section 2 will be the basis for this design. This chapter offers an analysis unique to this work for the LC- and LCL-control problem. These analyses encompass the influence of virtual damping on dynamic stiffness, command tracking with block diagrams, pole-zero plots, and frequency response function plots. Further, the difference between different decoupling techniques is described. Finally, this chapter shows the design of capacitor voltage and current observers for the LC- and LCL-plant yielding sensorless capacitor current information without deriving the capacitor voltage. These concepts are the reference for the discrete design of the following chapters.

Chapter 4 elaborates on chapter 3 by converting the ideas of chapter 3 into the discrete domain. This chapter highlights the issues that are unique to the z-domain. First, the discrete

modeling approach of the University of Rostock [24] is discussed and compared to the solution of the Aalto-University [11]. The reduced state-vector model is also compared to the actual system with frequency response function analysis. The chapter follows up with the control design, the observer structure in the discrete domain, and dynamic robustness analysis.

Chapter 5 shows the transition from the discrete domain into the implementation space. This chapter consequently introduces the PWM, the switches, and the system's delays. The harmonic problems due to the PWM are discussed, and possible solutions from the literature are discussed. Further, the unique issue of the misalignment of the voltage sampling for conventional sampling is discussed. Finally, the discrete-state observer structure for delay compensation is discussed in detail. The final control structure and dynamic robustness analysis in simulations are addressed at the end of the chapter.

Chapter 6 illustrates the experimental setup and measurement methods. This chapter will lay out the process for scaling the original converter to a low-voltage experimental setup. This part of the thesis will outline issues unique to the low-voltage design. The closing experimental dynamic analysis is discussed at the end.

2. Methods and Metrics

This chapter will lay out the methods and matrices used to design and evaluate control systems. These methods can be applied for continuous and discrete systems, but they change in complexity.

The design space, implementation space, and evaluation processes are not interchangeable. The design space offers more degrees of freedom than can be evaluated in the existing system. For instance, a pole-zero map can be designed accurately in the design space but cannot be measured. Actual measurements can fit results to a presumptive model yielding a reverse-engineered pole-zero map. However, this hypothetical model is a crucial source of error. This chapter, consequently, is split into the design space methods and the respective implementation space methods. Further, the last section will lay out the different complexity steps of this thesis's control problem.

2.1. Design Space

The design process of any system demands key metrics for evaluation. In this work, these critical attributes for control design are reference tracking capability, disturbance rejection, and robustness. Design choices often only evaluate reference tracking capability and robustness [7, 19, 26–36]. The papers [22, 23], which have been published in connection with this work, show severe dynamic disturbance response problems that can consequently get neglected, as discussed in chapter 2.1.4.

The primary metrics for reference tracking and disturbance rejections are pole-zero maps on the one side [37–40] and *Frequency Response Functions* (FRFs) [41–44] on the other side. As discussed previously, the pole-zero map is a tool of the design space. Frequency response functions, in contrast, can be used in both the design and implementation space.

While robustness analysis works well for both methods, subtle differences will be more apparent in frequency response function plots. This paper uses overlaid pole-zero maps and frequency response function plots to evaluate robustness.

2.1.1. Reference Tracking

Figure 2.1.a illustrates a continuous voltage source connected via a simple R/L load to the grid. Figure 2.1.c shows the state block diagram of this system. Equation (2.1), Figure 2.1.e, and Figure 2.1.d represent the relation between the input voltage and the output current as a transfer function, frequency response function plot, and pole-zero map, respectively. Both metrics reveal the *Eigenvalue* (EV) at – R/L.

$$\frac{I(s)}{V(s)} = \frac{1}{Ls + R} = \frac{1}{L\left(s + \frac{R}{L}\right)} \tag{2.1}$$

The pole-zero map reveals the attributes of each pole of a given system. The vector between the origin and the pole represents damping with the cosine of the angle of the vector, i.e., the real part and speed characteristics via the magnitude. Further, instability would occur for EVs on the right side of the imaginary axis. In this case, one eigenvalue of the plant is perfectly damped.

The frequency response function plot shows the same attributes. One break frequency (or eigenvalue) with a smooth transition in both angle and magnitude is present. Neither the frequency response function nor the pole-zero map seems to provide additional information over the other.

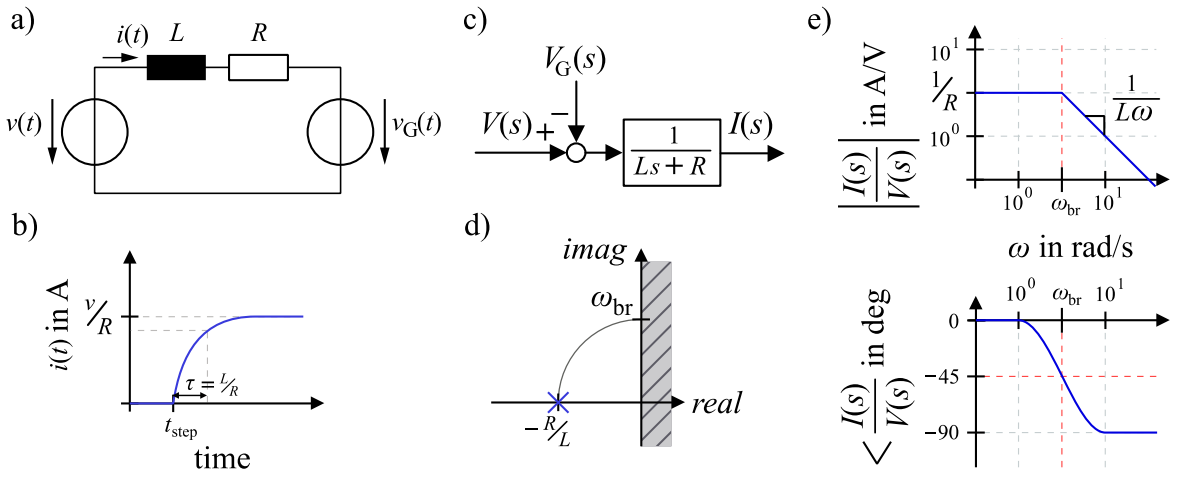

Figure 2.1: Continuous voltage source connected to the grid via R/L load. a) circuit diagram, b) step response, c) state block diagram, d) pole-zero map, and e) $I(s)/V(s)$ frequency response function magnitude (*top*) and phase (*bottom*).

Command Tracking

In this step, the control will be designed for reference tracking attributes. In the following steps, this work presents why this is not always the optimal approach. However, designing for tracking is the most common control design strategy [7, 12, 26, 45–50]. The transfer function of the system $I(s)/I^*(s)$ will be used throughout the paper for reference tracking evaluation. This frequency response function is referred to as *Command Tracking* (CT) [19, 23–26, 42, 43, 51].

$$\frac{I(s)}{I^*(s)} = \frac{K_\mathrm{p}}{Ls + K_\mathrm{p} + R}\,;\ \ \mathrm{EV}\colon \mathrm{p}_1 = -\frac{R + K_\mathrm{p}}{L} \tag{2.2}$$

$$\text{for } s \triangleq \mathrm{j}\omega \text{ and } \omega = 0\colon \left|\frac{I(\mathrm{j}\omega)}{I^*(\mathrm{j}\omega)}\right| = \frac{K_\mathrm{p}}{K_\mathrm{p} + R} \neq 1 \tag{2.3}$$

Figure 2.2.a shows the block diagram for the controlled system. Equation (2.2), Figure 2.2.d, and Figure 2.2.c show the command tracking for a pure *Proportional* controller (P-controller) as a transfer function, frequency response function plot, and pole-zero map, respectively. Both the frequency response function and the pole-zero map show a perfectly damped system. The break frequency is proportional to the gain of the P-controller. However, the frequency response function plot further reveals an offset error

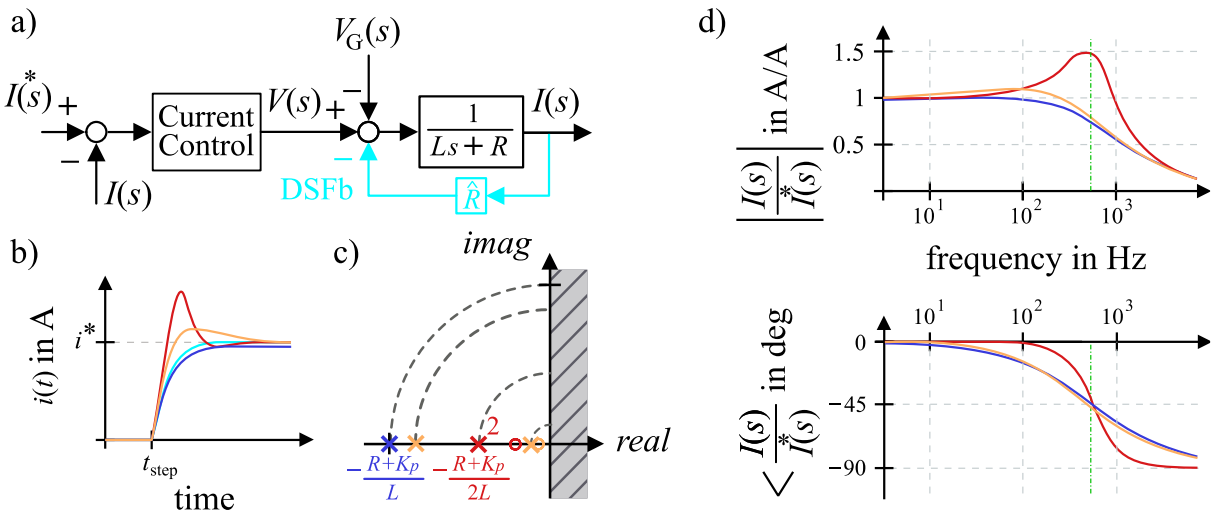

Legend: P-controller P-controller /w DSFb PI-controller /w close EVs PI-controller /w separated EVs

Figure 2.2: Continuous current control design: a) state block diagram, b) step response, c) pole-zero map, and d) command tracking plot − magnitude (*top*) and phase (*bottom*).

within the controller's bandwidth. Equation (2.3) shows that the natural state-feedback of the system − the resistance − causes this offset. Figure 2.2.b (teal) shows the influence of Decoupling State Feedback (DSFb – see also Figure 2.2.a – teal).

$$\frac{I(s)}{I^{*}(s)} = \frac{K_\mathrm{p} \cdot s + K_\mathrm{i}}{L \cdot s^2 + (K_\mathrm{p} + R) \cdot s + K_\mathrm{i}};\ \text{EVs: } p_{1/2} = -\frac{R + K_\mathrm{p}}{2L} \pm \sqrt{\left(\frac{R + K_\mathrm{p}}{2L}\right)^2 - \frac{K_\mathrm{i}}{L}} \tag{2.4}$$

$$\mathrm{Im}(\mathrm{EVs}) = 0 \text{ for: } \frac{K_\mathrm{i}}{L} \leq \left(\frac{R + K_\mathrm{p}}{2L}\right)^2 \tag{2.5}$$

$$\text{for } s \triangleq \mathrm{j}\omega \text{ and } \omega = 0\text{: } \left|\frac{I(\mathrm{j}\omega)}{I^{*}(\mathrm{j}\omega)}\right| = \frac{K_\mathrm{i}}{K_\mathrm{i}} = 1 \tag{2.6}$$

Equation (2.4), Figure 2.2.d, and Figure 2.2.c further show the command tracking for *Proportional-Integral* controllers (PI-controller) as a transfer function, frequency response function plot, and pole-zero map, respectively. The two eigenvalues can be seen in both the frequency response function equation and the pole-zero map. However, the second eigenvalue is not apparent in the frequency response function plot. Equation (2.5) shows the restriction for the gains. The eigenvalues move off the real axis with decreasing K_p or increasing K_i, and oscillations occur. Figure 2.2.b, however, shows that even within the restrictions of (2.5), overshoots and oscillatory behavior can occur. This is because two eigenvalues in close proximity represent a resonance.

The frequency response function plot in Figure 2.2.b, Figure 2.2.d illustrates the impact of separating these two eigenvalues on the dynamic behavior in the frequency domain and time domain, respectively. The effect of the separation and the extent to which the dynamic performance meets the requirements is difficult to evaluate on the pole-zero map. The frequency response function plots offer a more straightforward evaluation process in comparison. In contrast to the P-controller, the PI-controller does not cause any offset error, as shown in (2.6).

2.1.2. Disturbance Rejection

Dynamic Stiffness

In this step, the control will be evaluated regarding disturbance rejection. The inverse of the disturbance transfer function of the system $V_\mathrm{G}(s)/I(s)$ will be used throughout the paper for disturbance rejection evaluation. This frequency response function is referred to as *Dynamic*

Stiffness (DS) [19, 26, 52–57] (the name of this metric originates from mechanical systems and machine controls [58–60]). The unit of the dynamic stiffness of the current controller is Ω. The dynamic stiffness represents the output impedance of the controlled system seen from the grid. Consequently, for the dynamic stiffness analysis, the grid current is defined in the direction of the grid voltage. Dynamically well-behaved output impedances ensure stable parallel operation of multiple systems. Control designs aim to maximize this metric at the important frequencies with reasonable resulting energy demand.

The papers [61] and [62] explain the concept of passivity in the context of converter control. Further historical references of the concept can be found regarding the general theory in [63–65] and specifically for controls in [66, 67] and more recently in [68]. In essence, a component is passive if it absorbs energy from disturbances at any given frequency. Consequently, if the real portion of the dynamic stiffness (another denotation for dynamic stiffness is harmonic impedance [61]) was positive for all frequencies, the controlled system can be considered passive. Similarly, if the angle of the dynamic stiffness (harmonic impedance) was between -90 and 90 degrees, the system is passive. The concept of passivity further implies that the overall system is always passive in cases where all participants are passive. To summarize, any system with multiple participants will be stable and well-damped if all participants are designed to be passive (passivity is a sufficient metric but it is not necessary to ensure this behavior). Moreover, this also implies all participants provide active damping attributes for the overall system for any given resonance.

$$\frac{V_\mathrm{G}(s)}{I(s)} = Ls + K_\mathrm{p} + R;\ \text{EV: } \delta = -\frac{R + K_\mathrm{p}}{L} \tag{2.7}$$

$$\text{for } s \triangleq \mathrm{j}\omega \text{ and } \omega = 0\text{: } \left|\frac{V_\mathrm{G}(\mathrm{j}\omega)}{I(\mathrm{j}\omega)}\right| = K_\mathrm{p} + R \neq \infty \tag{2.8}$$

Equation (2.7), Figure 2.3.c, and Figure 2.2.a show the dynamic stiffness for a P-controller as a transfer function, frequency response function plot, and pole-zero map, respectively. The dynamic stiffness experiences the same characteristical break frequency as observed for the command tracking. The controlled system resembles a harmonic output impedance of a resistor with a value of $K_\mathrm{p} + R$ and the series inductor L. Therefore, low- and mid-frequency voltage disturbances only get rejected by a factor of $(K_\mathrm{p} + R)^{-1}$. Figure 2.3.b illustrates the consequent offset error for DC disturbances (see also (2.8)). The phase of the harmonic impedance seen from the grid is always between 90° and −90°. Thus, the system is passive.

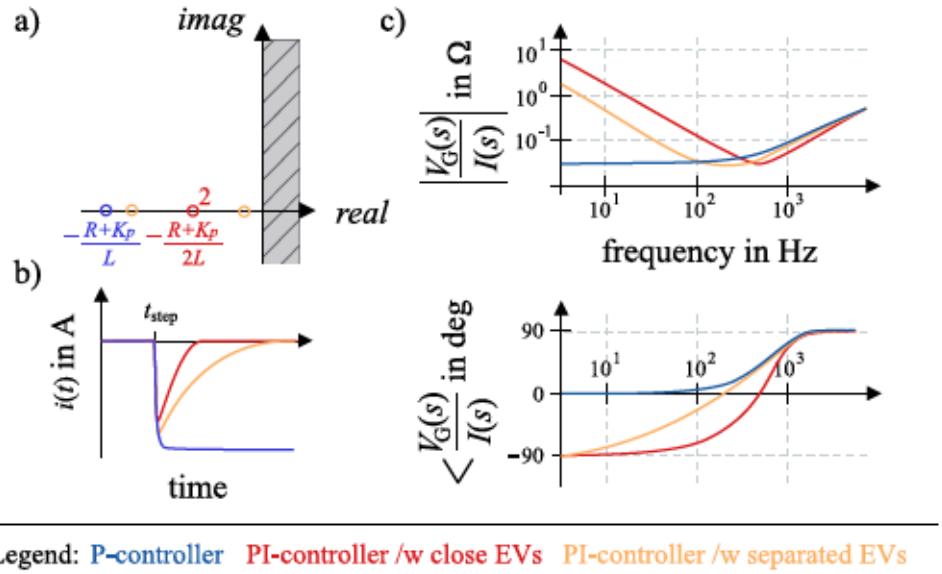

Legend: P-controller PI-controller /w close EVs PI-controller /w separated EVs

Figure 2.3: Continuous current control design: a) pole-zero map of the dynamic stiffness, b) load step response, c) dynamic stiffness plot – magnitude (*top*) and phase (*bottom*).

Equation (2.9), Figure 2.3.c, and Figure 2.3.a show the dynamic stiffness for a PI-controller as a transfer function, an overlaid frequency response function plot, and an overlaid pole-zero map, respectively. The PI-controller resembles an impedance containing a resistor with a value of $K_\mathrm{p} + R$, a series capacitor with a value of K_i^{-1}, and a series inductor with a value of L.

$$\frac{V_\mathrm{G}(s)}{I(s)} = Ls + (K_\mathrm{p} + R) + K_\mathrm{i}/s; \quad \text{EVs: } \delta_1 \approx -\frac{R + K_\mathrm{p}}{L},\ \delta_2 \approx -\frac{K_\mathrm{i}}{R + K_\mathrm{p}} \tag{2.9}$$

$$\text{for } s \mathrel{\hat{=}} \mathrm{j}\omega \text{ and } \omega = 0\text{:} \left|\frac{V_\mathrm{G}(\mathrm{j}\omega)}{I(\mathrm{j}\omega)}\right| = \infty \tag{2.10}$$

The controller with two close eigenvalues shows the strongest disturbance rejection at low- to mid-frequencies but slightly lower dynamic stiffness at high frequencies (see also Figure 2.3.c). Both PI-controllers show passive behavior, though. Two very close eigenvalues represent a resonance. The controller with separated eigenvalues demonstrates a slower phase transition, which yields lower resonant properties. Equation (2.10) indicates that the dynamic stiffness at very low frequencies becomes infinite. Thus, PI-controllers decouple DC disturbances entirely (see also Figure 2.3.b).

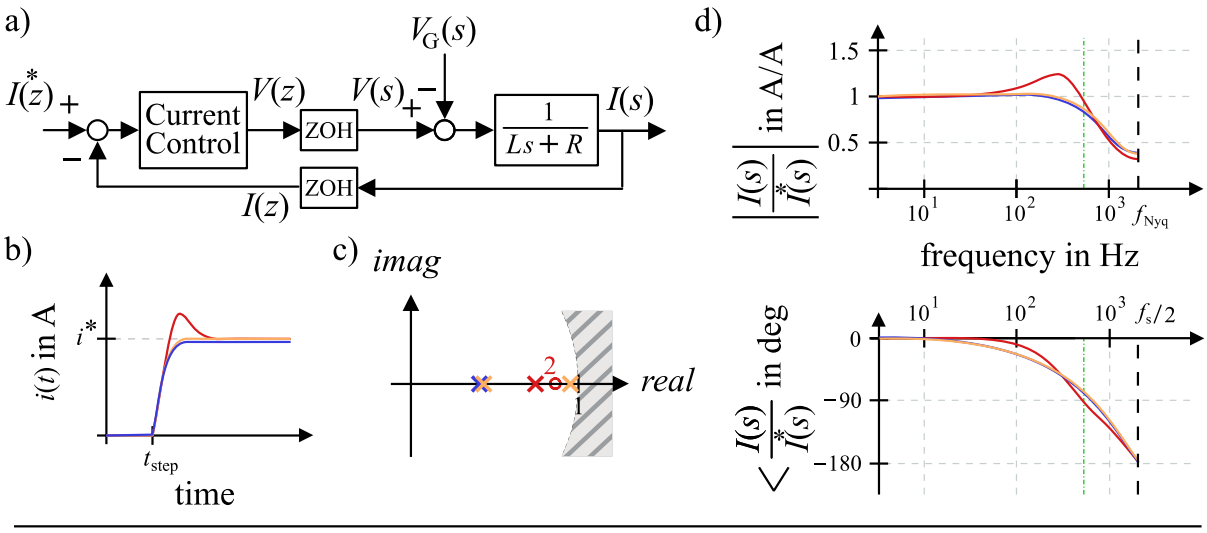

Legend: P-controller PI-controller /w close EVs PI-controller /w separated EVs

Figure 2.4: Discrete current control design: a) state block diagram, b) step response, c) pole-zero map, and d) command tracking plot − magnitude (*top*) and phase (*bottom*).

2.1.3. Discrete-Design

The publications in [19, 45] and the paper [23], which is connected to this work, provide a systematic approach for direct discrete modeling. Equation (2.11) shows the discrete model of the L-filter topology. The integrator of the PI-structure in the discrete domain can be expressed by using the Tustin, the Forward Euler, or the time-weighted accumulation approximation. However, all of these structures yield a total gain K, a pole at 1, and a zero at δ, as shown in (2.12). The equations (2.12) and (2.13) illustrate the controlled system's open-loop and closed-loop transfer functions, respectively. The eigenvalues are located, as shown in (2.14). In this case, increasing δ or decreasing K separates the eigenvalues.

Figure 2.4.c and Figure 2.4.a show the overlaid dynamic stiffness for a PI-controller as a frequency response function plot and pole-zero map. The attributes of the discrete control design are very similar to the continuous structure. Since sampling warps the discrete frequency domain into a circle, the magnitude never falls off to zero, and the phase approaches −180° at the Nyquist frequency in contrast to the −90° in the continuous case.

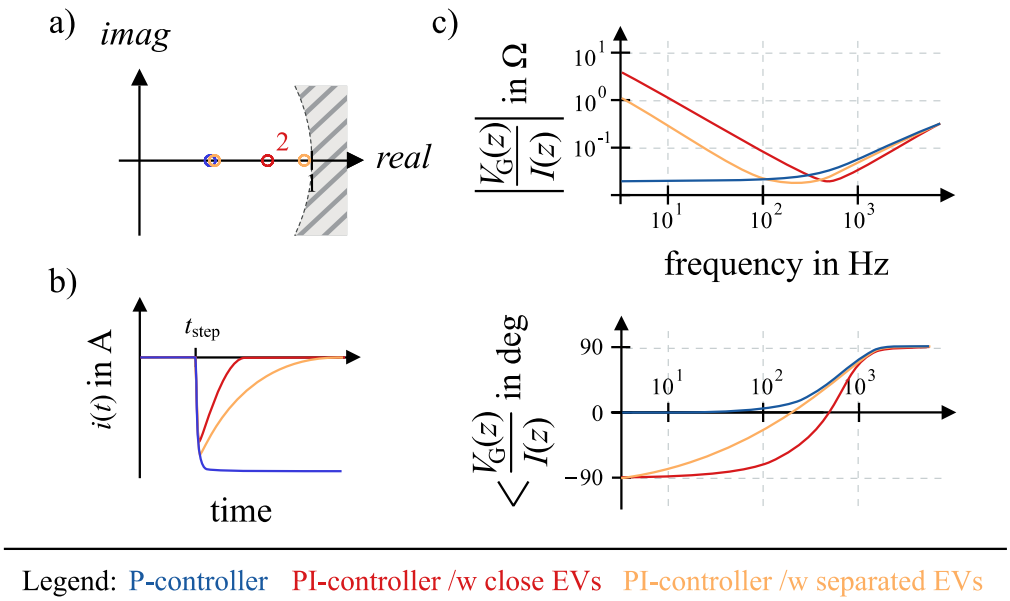

Figure 2.5: Discrete current control design: a) pole-zero map of the dynamic stiffness, b) load step response, c) dynamic stiffness plot − magnitude (*top*) and phase (*bottom*).

Figure 2.5 similarly illustrates the disturbance rejection of the discrete control system. The results are almost identical to the continuous design.

$$\frac{I(z)}{V(z)} = \frac{\left(1 - \mathrm{e}^{-T/\tau}\right) z^{-1}}{R\left(1 - \mathrm{e}^{-T/\tau} z^{-1}\right)} = \frac{A_1 z^{-1}}{1 - B_1 z^{-1}} \tag{2.11}$$

$$\left.\frac{I(z)}{I^*(z)}\right|_{\text{open loop}} = K \frac{1 - \delta z^{-1}}{1 - z^{-1}} \frac{\left(1 - \mathrm{e}^{-T/\tau}\right) z^{-1}}{R\left(1 - \mathrm{e}^{-T/\tau} z^{-1}\right)} \tag{2.12}$$

$$\frac{I(z)}{I^*(z)} = K \frac{(z - \delta) A_1}{z^2 + z(A_1 K - 1 - B_1) + B_1 - K\delta A_1} \tag{2.13}$$

$$\text{EVs: } p_{1/2} = -\frac{A_1 K - 1 - B_1}{2} \pm \sqrt{\left(\frac{A_1 K - 1 - B_1}{2}\right)^2 - B_1 + A_1 K \delta} \tag{2.14}$$

2.1.4. Design for Dynamic Stiffness or Command Tracking

Current control both for machine and grid applications is commonly done in the synchronous dq-reference-frame [26, 69–76]. The advantages of this reference frame are the clear distinction between the reactive and active portion of the current and that the

commands operate in a DC- instead of an AC-steady-state-system. Thus, no phase nor magnitude error will be present for a PI-controlled system during a steady state. The paper [26] further shows that the usage of this reference frame introduces a cross-coupling between the d- and q-current. The work of [26] also presents two techniques to overcome this issue.

On the one hand, the cross-coupling can be decoupled as feedback (see Figure 2.6.a). On the other hand, the cross-coupling can be canceled through the forward path (see Figure 2.6.b). The results in [26] suggest that the forward path solution shows superior dynamic attributes with far less parameter sensitivity regarding the inductance value.

The paper [22], which was published in connection with this work, illustrates the stronger command tracking robustness regarding L for the forward path solution, as well (compare Figure 2.7.a and Figure 2.7.b). However, that paper [22] provided evidence that the forward path solution can cause resonance issues at high synchronous speed. This resonant issue is observable primarily in the dynamic stiffness but not in the command tracking shown in Figure 2.7 – compare c) and d).

The same affiliated research groups of [26] extended their work in [19] towards a discrete control design with a forward path solution for the cross-coupling of the d- and q-current (see Figure 2.6.d). Analog to the continuous case, the forward path approach provides high robustness for command tracking. The paper [23], which was published in connection with

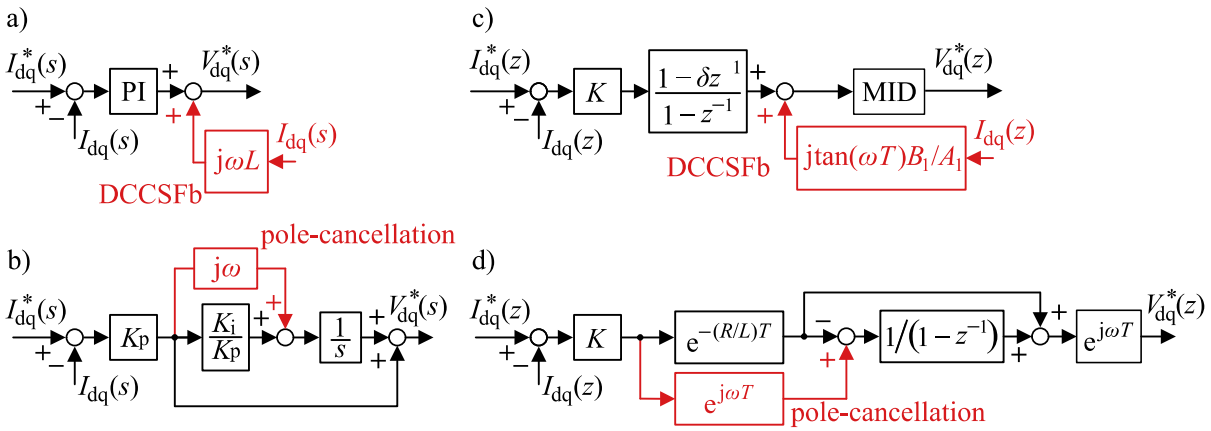

Figure 2.6: Decoupling techniques of the dq-current cross-coupling: a) continuous decoupling cross-coupling via active state feedback (DCCSFb) [22], b) continuous pole-cancelation via complex zero in the forward path [22], c) discrete decoupling cross-coupling (DCCSFb) w/ MID – *Manipulated Input Decoupling* [24] (connected to this work), d) discrete pole-cancelation via complex zero in the forward path [19]. The non-complex version of this figure is displayed in the appendix in Figure 9.4.

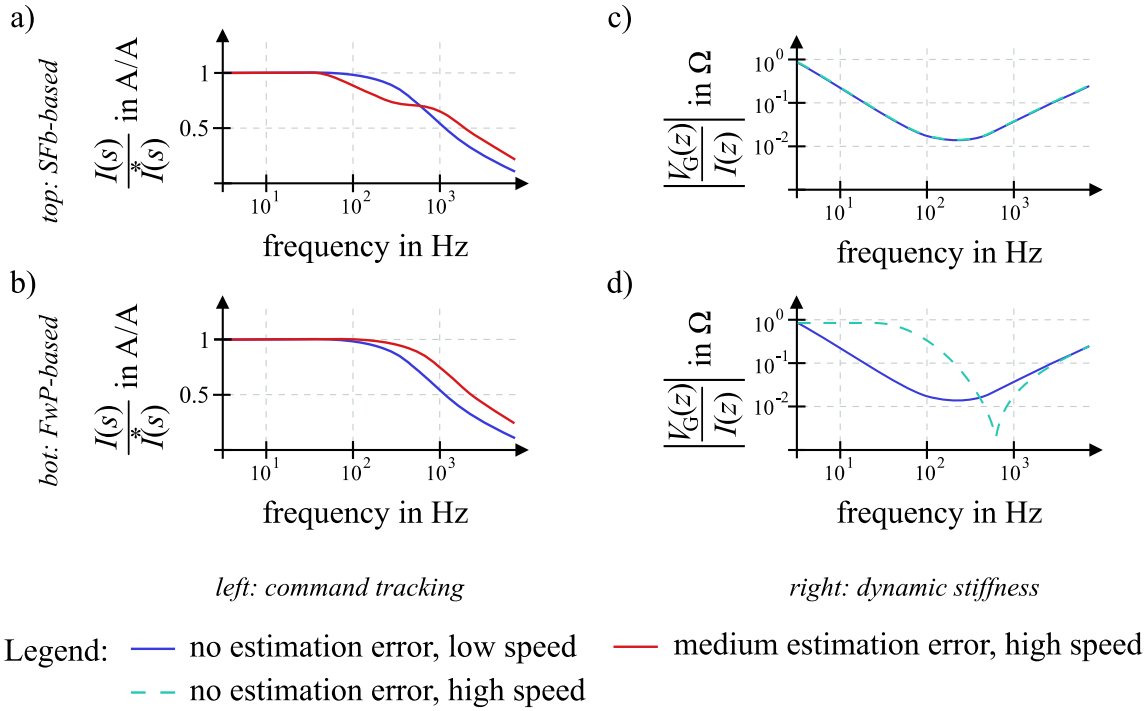

Figure 2.7: Comparison of dynamic performance of two different decoupling techniques of the dq-current cross-coupling for different L estimation errors and synchronous speeds ω (low = 50 Hz, high = 500 Hz). *Top*: Feed forward path-based [24]/[19], *Bottom*: State feedback-based [25]/[22], *Left*: Command tracking (no estimation error at high speed overlaps with no estimation error at low speed), *Right*: Dynamic stiffness (estimation error affects D.S. very little – not included) .

this work, presents a discrete decoupling technique via feedback (see Figure 2.6.c). The work in [23] further reveals the same resonant problems for the discrete forward path solution at high synchronous speed/slow sampling/slow switching.

This example highlights the importance of designing for both dynamic stiffness and command tracking. For stability and passivity, dynamic stiffness seems to be the most crucial metric for large intertwined systems.

2.2. Implementation Space

Implementation Design

The final complexity step in design in this paper is referred to as the implementation space. This complexity step has to be in the discrete domain due to the implementation on a DSP/FPGA setup. Moreover, this complexity step allows only real-life applicable design

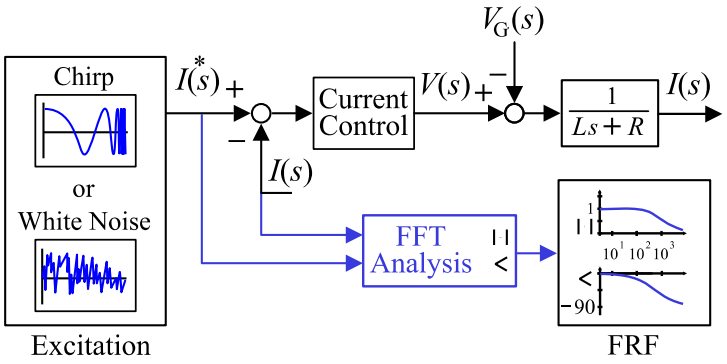

Figure 2.8: Frequency response estimation process for command tracking.

tools. The model at this complexity contains further effects such as delays, dead times, the actual PWM, switching times, noise, and overload issues.

Control Design and Evaluation

The design and evaluation tools of the implementation space are limited compared to the design space. As mentioned previously, the pole-zero map cannot be measured. Dynamic measurements can be used to fit results to a model yielding a reverse-engineered pole-zero map. Through false assumptions, this approach can lead to wrong findings, though.

Dynamic frequency response function plots are obtainable in the design and implementation space, such as command tracking and dynamic stiffness. A common approach to extracting these dynamic plots is made via test signals. The test signals excite the system. The relation between the excitement and the system's response provides the information needed for a frequency response estimation. [77]

A fast and widely implemented method is the excitement with signals that contain components with a range of frequencies – such as white noise or chirp signals. The frequency analysis of the input and output signal directly provides the frequency response function plot. [77]

Another approach is the so-called single-sine test. In this test, a single sinewave is used to obtain the magnitude and phase information of the frequency response function for one specific frequency. Consequently, only multiple single-sine wave tests provide a range of frequency information for a full frequency response estimation.

The test signals are applied to the reference to obtain a command tracking plot. Figure 2.8 shows the conceptual estimation process of the frequency response.

For a dynamic stiffness test, on the other hand, a dynamic disturbance is needed that contains a wide range of frequencies, as shown in Figure 2.9.a. In many applications, achieving such disturbance excitation is very challenging. In some cases, a very long observed time frame ensures enough detected frequency components through random disturbance similar to white noise, thus yielding appropriate frequency response estimation. In other cases, this might never occur.

Virtual Disturbance

Another way to achieve dynamic disturbances over a wide range of frequencies is the usage of the control itself. Figure 2.9.b. shows the implementation of a virtual disturbance for the first order R/L system. Adding a virtual disturbance to the manipulated input has very similar effects on the system compared to an actual disturbance yielding accurate frequency response estimation, as well.

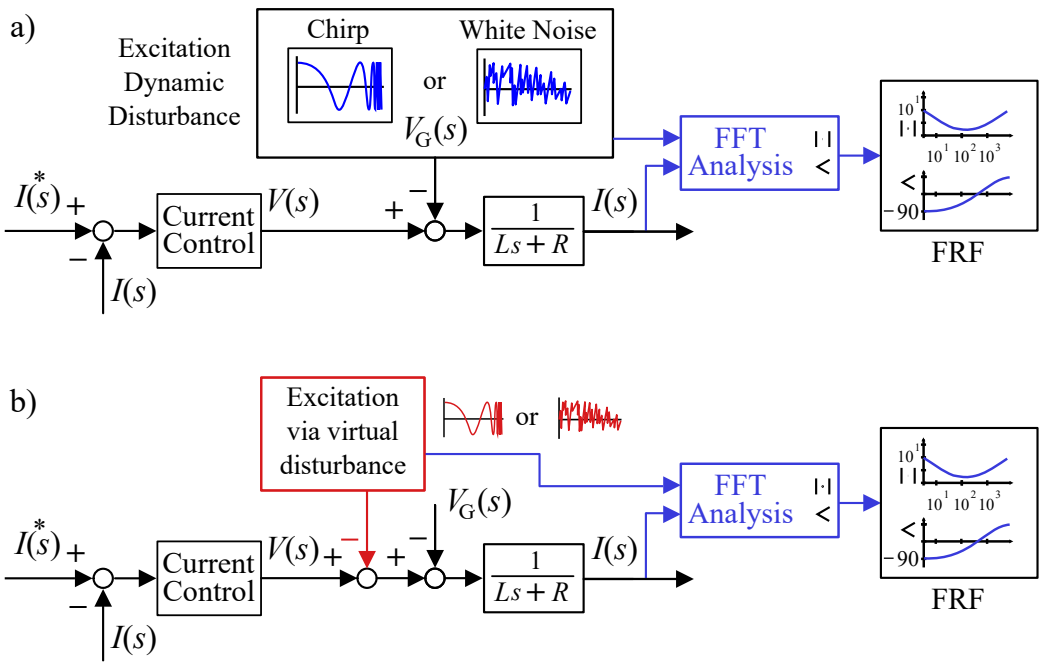

Figure 2.9: Frequency response estimation process or dynamic stiffness: a) with a dynamic disturbance and b) with a virtual disturbance.

2.3. Complexity Steps of the Control Design

This work performs different design methods for the presented LCL problem at consecutively increasing complexity levels.

Starting with the continuous design helps to achieve a general approach and provides crucial insight into the main issues of the control problem. The discrete design's subsequent conversion will highlight problems in the discrete world (close to implementation space). The design models the inverter as a discrete voltage source at this complexity step. The implementation space depicts the inverter with actual switches introducing delays, the PWM, and dead times.

Chapter 1 discusses the opportunity to decouple the capacitor voltage, consequently transforming the problem into a simple first-order R/L system – see also Figure 1.2.d. The following chapter presents the complete current control design and remaining control issues of the LC structure.

3. Continuous Design

This chapter defines the continuous control problem of this work, lays out the control design, and closes with dynamic analyses. Although the implementation space is in the discrete domain, everything but the converter itself still operates in the continuous-time frame. Thus, analyzing the system in the continuous environment offers crucial insights into the control problem. The concepts of this first design and analysis are the basis of the consecutive design steps at the different complexity levels.

The definition of the control problem contains the assumptions and approximations used as a first model. Further, this step discusses the dynamic attributes of the plant and demonstrates the options of control topologies.

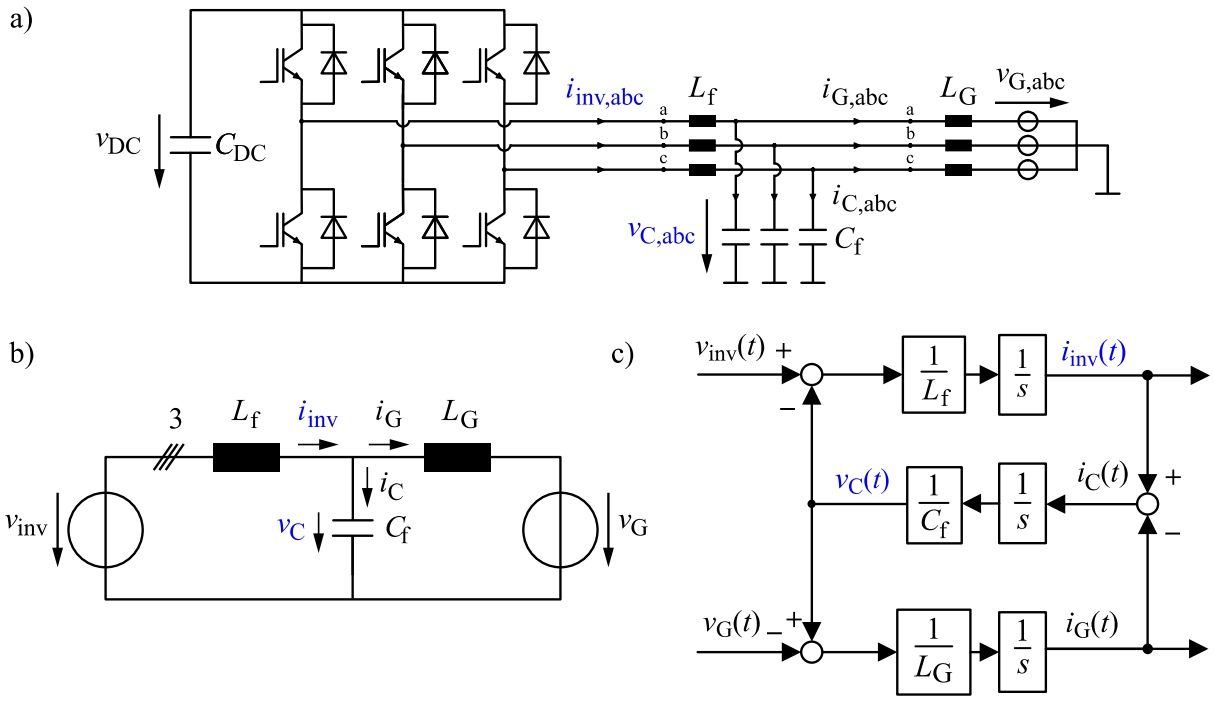

Figure 3.1: Three-phase two-level inverter connected to the grid via an LC-filter. a) circuit diagram – blue depicts the measurements for the LC-topology (inverter current i_{inv} and capacitor voltage v_C), b) first-order equivalent model (continuous voltage source representation), and c) state block diagram of the first-order model. For clarity resistances are neglected here.

The control design and dynamic analysis utilize the methods of chapter 2 to achieve a dynamically well-behaved system. The 5 MW 3 kHz wind turbine converter of Table A.1 (Appendix) is used for all plots in this chapter.

3.1. Control Problem

3.1.1. Analysis

Figure 3.1 and Figure 3.2 depict the control problem – a three-phase inverter connected to the grid via a second-order LC or LCL filter, respectively. Figure 3.1.b shows the first-order approximation of the inverter as a continuous voltage source. Equations (3.1), (3.2), and Figure 3.1.c present the transfer function between inverter voltage and grid current, and between grid current and grid voltage (harmonic impedance) for the LC filter configuration. The resonance occurs at $\omega_{\mathrm{Res}} = 2\pi f_{\mathrm{Res}} = \sqrt{(L_{\mathrm{f}} + L_{\mathrm{G}})/(L_{\mathrm{f}} L_{\mathrm{G}} C_{\mathrm{f}})}$ and the anti-resonance at $\omega_{\mathrm{ar}} = 2\pi f_{\mathrm{ar}} = \sqrt{1/(L_{\mathrm{f}} C_{\mathrm{f}})}$ for the LC-filter. The resonance frequency of such systems is usually designed to be well below the switching frequency and above the bandwidth to avoid strong excitation by the inverter. [78]

$$\frac{I_{\mathrm{G}}(s)}{V_{\mathrm{inv}}(s)} = \frac{1}{L_{\mathrm{f}} L_{\mathrm{G}} C_{\mathrm{f}} \cdot s} \quad \frac{1}{s^2 + \omega_{\mathrm{Res}}^2} \tag{3.1}$$

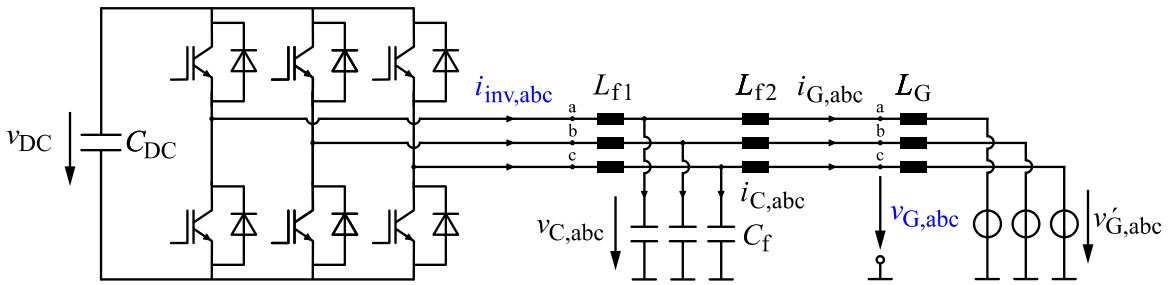

Figure 3.2:Three-phase two-level inverter connected to the grid via an LCL-filter – blue depicts the measurements for the LCL-topology (inverter current $i_{\mathrm{inv,abc}}$ and PCC-voltage $v_{\mathrm{G,abc}}$). For clarity resistances are neglected here.

$$\frac{I_G(s)}{V_G(s)} = \frac{1}{L_G \cdot s} \frac{s^2 + \omega_{ar}^2}{s^2 + \omega_{Res}^2} \tag{3.2}$$

Figure 3.3 (red) illustrates the frequency behavior of the impedance seen from the grid. The impedance of the plant drops to the combined series resistance of the plant at the resonance frequency. This impedance is orders of magnitude lower than the grid impedance.

As the impedance of the plant becomes virtually zero at the resonance frequency, a conventional PI-controller is not capable of forcing the plant to track at this frequency without any decoupling. However, as shown in Figure 3.3 (blue), the P-portion of a current controller (K_p) provides similar attributes to series resistance, thus decreasing the resonance effect. However, increasing the K_p further does not yield significantly improved resonance damping. Higher K_p implies an increased bandwidth of the controller. Reduced damping is observed once the bandwidth exceeds the resonance (see Figure 3.4).

The well-damped harmonic impedance seen in Figure 3.3 and Figure 3.4 is only valid without voltage decoupling. However, voltage decoupling is essential for any current

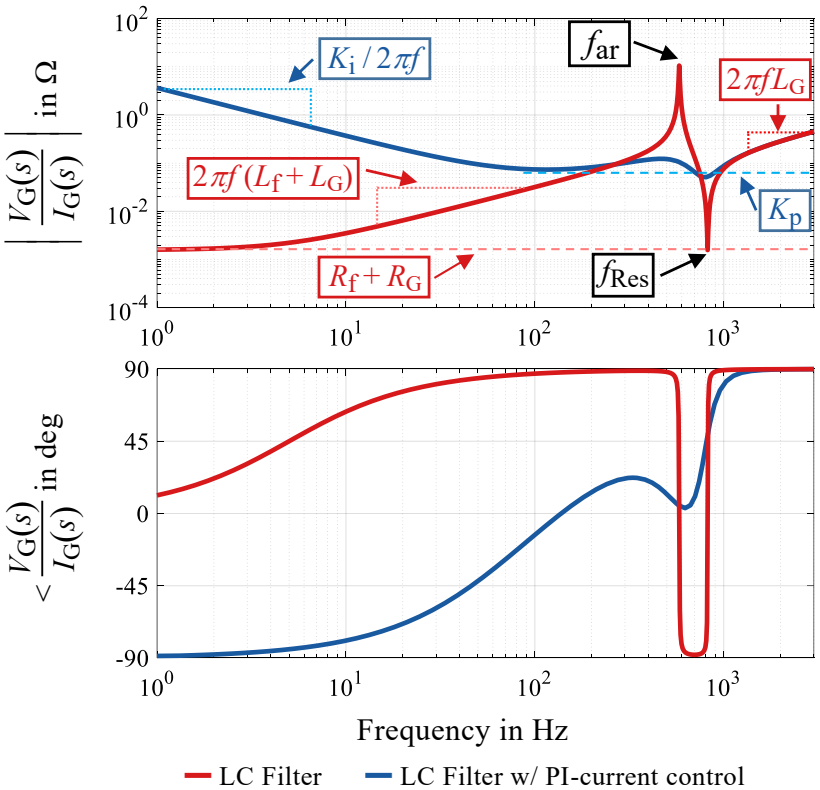

Figure 3.3: Dynamic stiffness of the LCL problem. red: Impedance of LCL-structure seen from the grid w/o control, blue: Impedance of LCL-structure seen from the grid w/ PI-current control (LC/LCL-topology – w/o voltage decoupling).

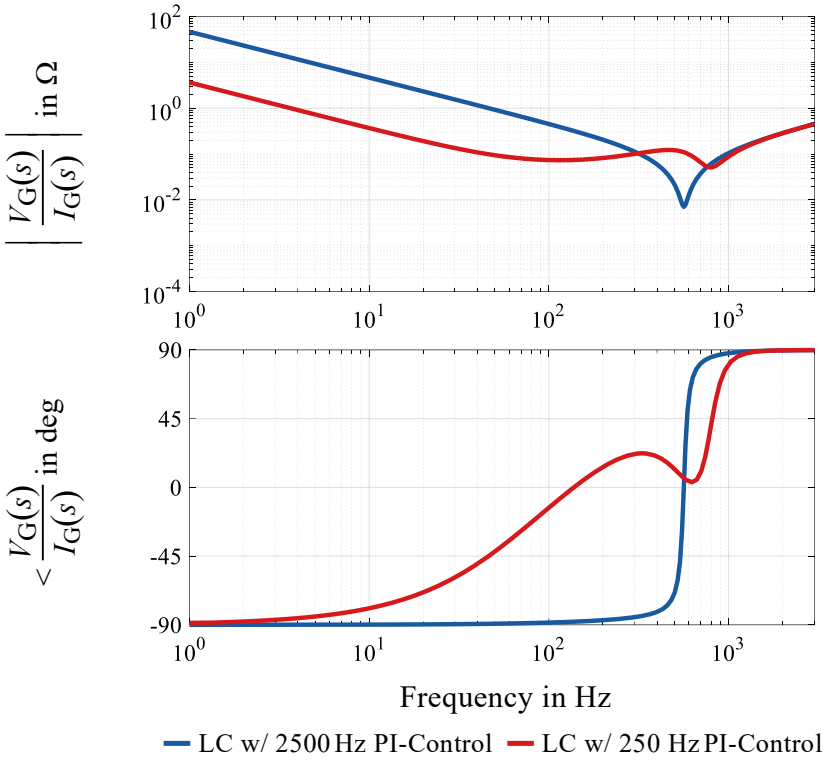

Figure 3.4: Impedance seen from the grid for the LC-filter topology for different tuning of the current PI-controller. *Blue*: 2500 Hz bandwidth, *Red*: 250 Hz bandwidth (LC/LCL-topology – w/o voltage decoupling).

controller since it defines the plant until the decoupled voltage vastly increases robustness regarding the grid impedance. Without this decoupling, the current controller needs accurate information about the entire grid impedance, making the current control concept very challenging to implement. In most applications, such grid information is not feasible to attain. Further, the grid impedance changes over time. Therefore, the control has to be robust regarding the grid state.

As lined out in chapter 1, the notch filter and the resonant control approach have major setbacks within parameter sensitivity regarding the grid impedance—however, the decoupling of the capacitor voltage and implementation of a virtual resistance display promising attributes. If the capacitor voltage was entirely decoupled, the controlled plant – seen from the converter – would shrink to a first-order problem without any resonance. The implementation of a virtual resistance, on the other hand, would limit the resonance effect seen from the grid.

Both strategies rely on state information that might not be available for every application. Further, only a continuous control environment can correctly represent a virtual resistance

and fully decouple a continuous disturbance. Tackling these issues is the key objective of the upcoming chapters.

There is a wide variety of possible topologies regarding filter and measurement setups. This chapter discusses two very common topologies. The LC-topology is the LC-filter with measurements for the inverter current i_{inv} and the capacitor voltage v_C (see Figure 3.1). The LCL-topology is the LCL-filter setup with sensors for the inverter current i_{inv} and the *Point of Common Coupling*-voltage v_G (PCC-voltage) – see Figure 3.2.

3.1.2. Decoupling State Feedback vs. Disturbance Input Decoupling

The previous chapters introduced various decoupling techniques. These decoupling techniques can be broadly separated into decoupling state feedback (DSFb – *Decoupling State Feedback* and DCCSFb – *Decoupling Cross-Coupling State Feedback*) and *Disturbance Input Decoupling* (DID). This subchapter analyzes the system's sensitivity regarding these two forms of decoupling.

Figure 3.5.a shows the implementation of the capacitor voltage decoupling and a state feedback decoupling of the filter resistance of an LC-resonance. Figure 3.5.c illustrates the

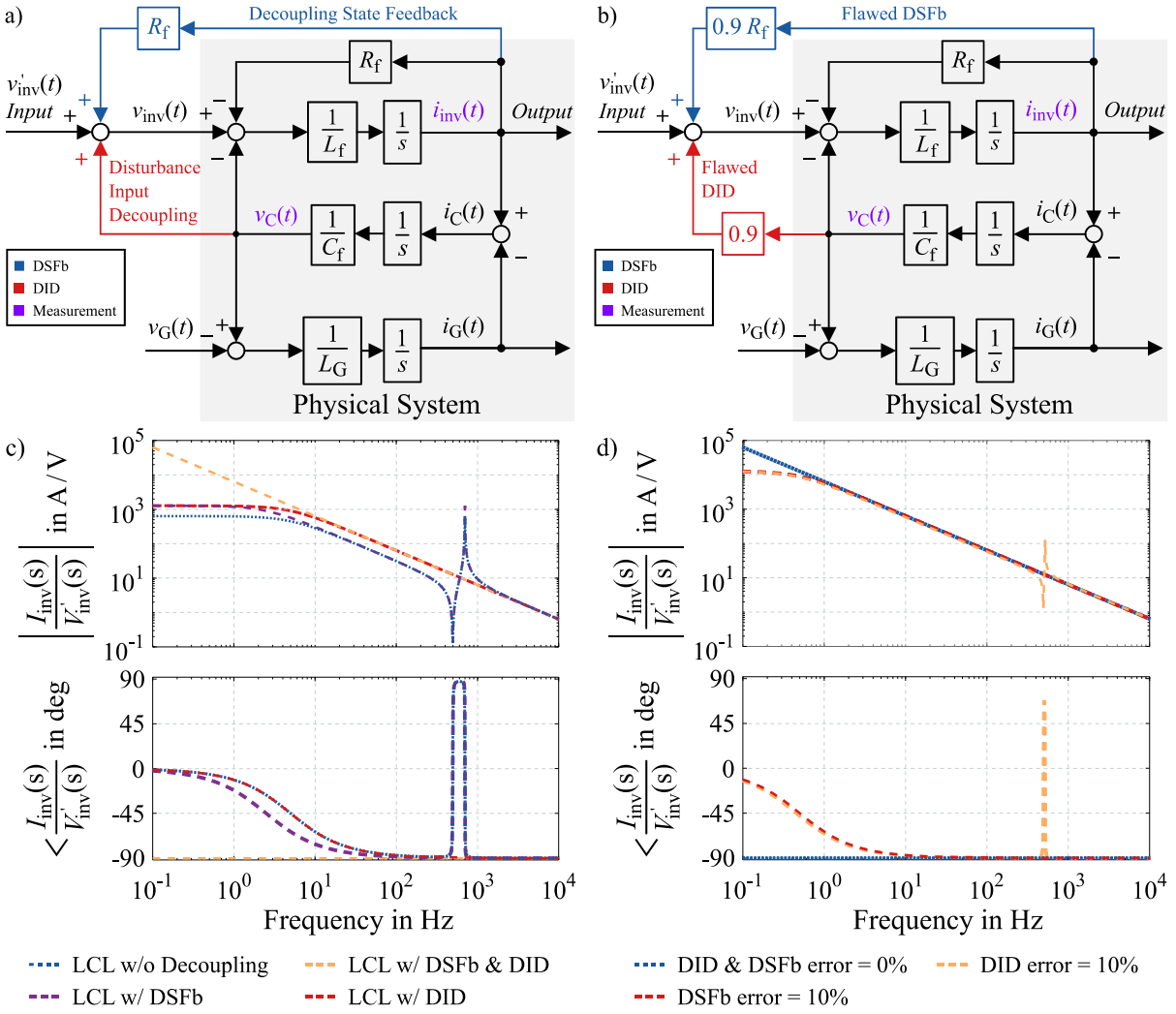

Figure 3.5: Influence and comparison of disturbance input decoupling and decoupling state feedback for the LC-topology. a) state block diagram of the implementation, b) state block diagram of the flawed implementation, c) frequency response estimation for different combinations of the decoupling techniques, d) comparison of the influence of signal errors on the effectiveness of the decoupling techniques.

frequency response function plot of the inverter current with respect to the inverter voltage with different combinations of these decoupling techniques. Figure 3.5.d shows the frequency response function's influence due to flawed signals for the decoupling, as indicated above in the same figure (Figure 3.5.b).

The disturbance input decoupling changes the controlled plant dramatically. In this case, the disturbance input decoupling changes the inverter transfer function from a second-order to a first-order system. Consequently, the frequency response function alters strongly with flawed disturbance input decoupling, shown in Figure 3.5.d − orange. The resonance and antiresonance (singularity with very high impedance) are not fully decoupled anymore.

On the other hand, the decoupling state feedback does not change the order of the system. It merely leaves some of the PT1-behavior of the system instead of a pure integration system.

Some might argue that the system becomes unstable when the decoupling state feedback is bigger than the natural state feedback as it yields positive feedback. This instability would be true without control, but once control is implemented, the positive feedback can still be beneficial and will not cause instability. The remaining state feedback merely shifts the intended eigenvalues by a tiny margin.

The type of information needed for each decoupling technique offers another perspective and further physical insight into the shown issues. A disturbance usually cannot be observed. In the LC-topology, the capacitor voltage can be observed as a state (instead of a disturbance) only with complete state information (see Figure 4.3 – comparison between full-state and reduced-state models), including the grid current (actual disturbance). Thus, observers often can only yield estimated (and therefore flawed) disturbance information.

In many cases, the disturbance might not even be an energy state at all. The consequent volatility and unpredictability of the disturbance combined with its strong influence on the controlled system make disturbance input decoupling a very sensitive technique in comparison.

3.2. Control Design

This subchapter outlines the control design for the LC- and the LCL-topology with active damping approaches, as discussed in chapter 1.

3.2.1. LC-Topology

Since the LC-topology (see Figure 3.1) encompasses the state information of the capacitor voltage, the decoupling of the capacitor voltage is part of the current control in any case. Figure 3.6 illustrates the two discussed options of control techniques for the LC-topology. As described previously, the decoupling of the capacitor voltage breaks the plant – seen from the converter – down to a first-order L-load. Using (2.4), the eigenvalues of the plant are placed at $f_{\mathrm{Res}} / 3$ and $f_{\mathrm{Res}} / 30$ (250 Hz and 25 Hz). As described in subchapter 2.1.4, the current control of grid-side inverters utilizes the dq-reference frame. The consequent decoupling of the cross-coupling between the d- and q-current is integrated into the control, as well (Figure 3.6).

$$\frac{I_{\mathrm{G}}(s)}{V_{\mathrm{C}}(s)} = \frac{\omega_0^2 C \cdot s}{s^2 + \omega_0^2} \tag{3.3}$$

$$\frac{I_{\mathrm{G}}(s)}{I_{\mathrm{C}}(s)} = \frac{\omega_0^2}{s^2 + \omega_0^2} = \frac{I_{\mathrm{G}}(s)}{I_{\mathrm{inv}}(s)} \tag{3.4}$$

Figure 3.8 and (3.6) provide the transfer function with implemented virtual impedance. Figure 3.9 depicts the pole-zero map for the grid impedance and command tracking for the approach with and without a virtual resistor R_{vir}.

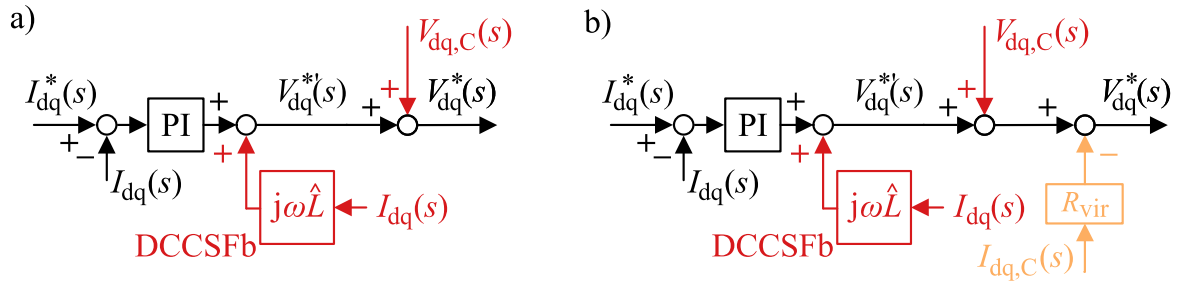

Figure 3.6: Control techniques with active damping for the LC-topology. a) voltage decoupling, b) voltage decoupling and virtual resistor implementation in series with capacitor. A separate dq-representation including the load can be found in Figure 9.3 in the appendix chapter.

$$I_{\mathrm{inv}}(s)\cdot Ls = \left(I_{\mathrm{inv}}^{*}(s) - I_{\mathrm{inv}}(s)\right)\cdot G_{\mathrm{PI}}(s) - I_{\mathrm{inv}}(s)\cdot R_{\mathrm{vir}}\left(1 - \frac{I_{\mathrm{G}}(s)}{I_{\mathrm{inv}}(s)}\right) \tag{3.5}$$

$$\frac{I_{\mathrm{inv}}(s)}{I_{\mathrm{inv}}^{*}(s)} = \frac{K_{\mathrm{p}}\cdot s + K_{\mathrm{i}}}{L_{\mathrm{f}}\cdot s^2 + \left(K_{\mathrm{p}} + R_{\mathrm{vir}} - \frac{R_{\mathrm{vir}}\cdot\omega_0^2}{s^2+\omega_0^2}\right)\cdot s + K_{\mathrm{i}}} \tag{3.6}$$

Figure 3.7 illustrates the overlaid command tracking plot for the inverter current and the overlaid dynamic stiffness plot (impedance seen from the grid) for varying virtual resistors.

Due to the well-decoupled capacitor voltage, command tracking of the inverter current is not an issue. Without any virtual resistance, well-behaved tracking is achieved. On the contrary, Figure 3.7, Figure 3.8, Figure 3.9, and (3.6) – compared to (2.4) – show that increased virtual resistance yields antiresonant behavior above the controller's bandwidth. This antiresonance does not constitute any problems to the system, though. Further, the

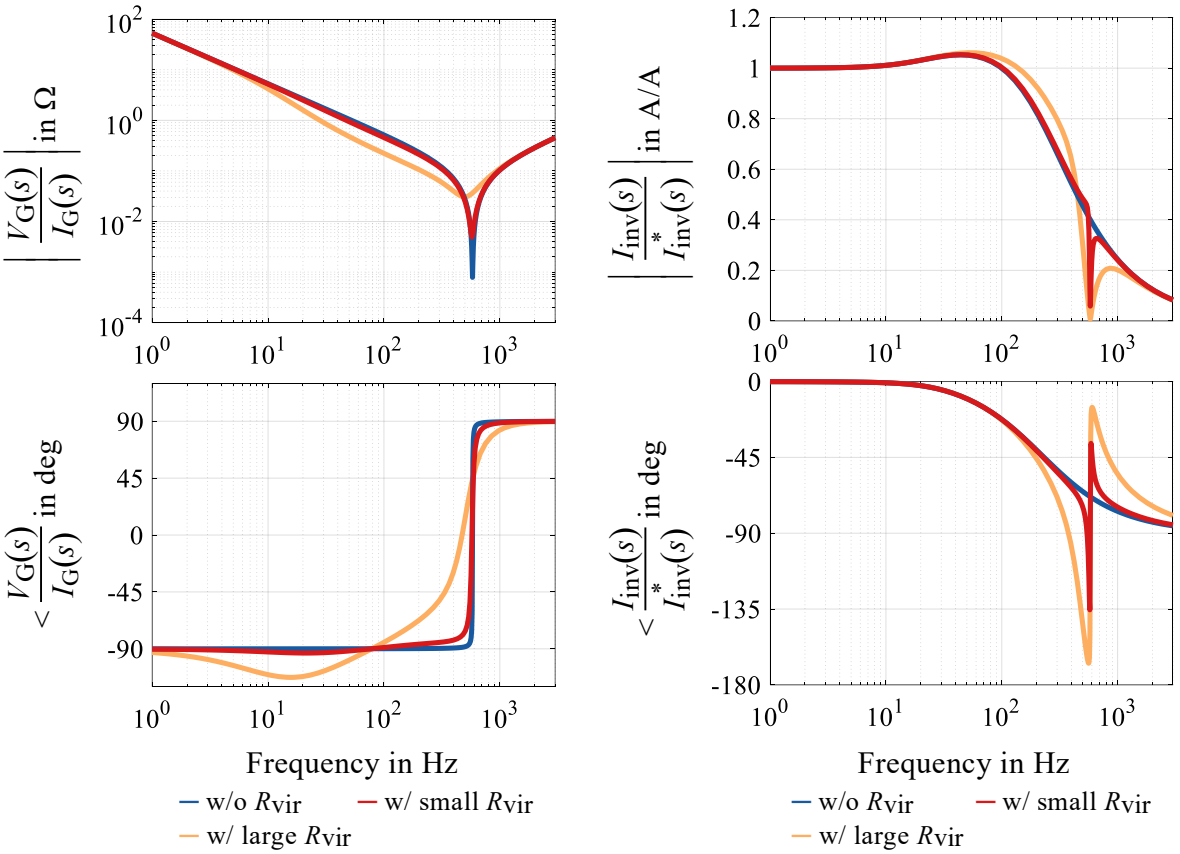

Figure 3.7: Dynamic analysis of the current controller for the LC-topology with varying virtual resistance: *Left*: dynamic stiffness, *Right*: command tracking (note – the system is modelled with losses, thus the phase does not fully drop to –180 deg).

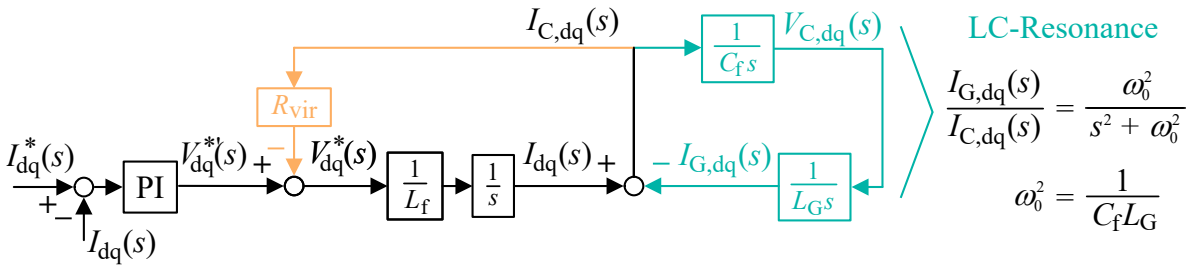

Figure 3.8: Block diagram of the active damping approach via virtual resistance R_{vir} with the assumption of decoupled capacitor voltage and implemented decoupling of the dq-current cross-coupling. The grid-side resonant LC-structure couples back via R_{vir} yielding an antiresonance for the current command tracking at ω_0.

pole-zero map reveals oscillatory poles. These poles are close to the antiresonance and thus do not influence the dynamic performance.

Equation (3.7) illustrates the impedance seen from the grid. This impedance contains the grid impedance and the filter capacitance – an LC-resonance. The dynamic stiffness in Figure 3.7 consequently reflects this LC as harmonic impedance.

$$\frac{V_G(s)}{I_G(s)} = L_G \cdot s + \frac{1}{C_f \cdot s} - \frac{R_{vir}}{L_f C_f \cdot s^2 + C_f(K_p + R_{vir}) \cdot s + C_f K_i} \tag{3.7}$$

The virtual impedance implementation suppresses the resonance effect very effectively (see Figure 3.7 – left in blue). The equation (3.7) shows that the virtual resistance adds a series impedance to the grid-side LC-resonance. The series impedance added by the control via

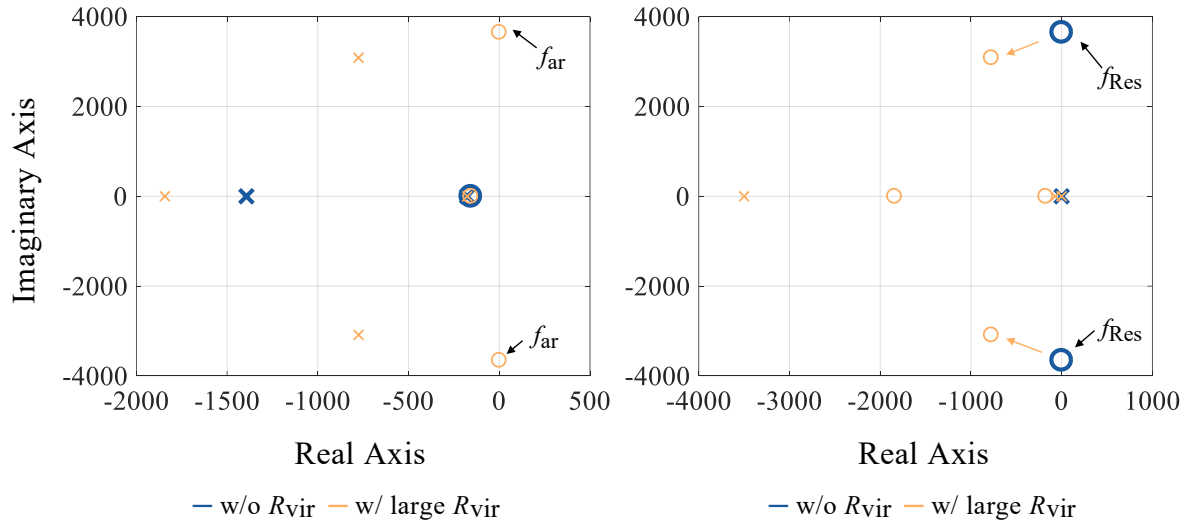

Figure 3.9: Pole-zero map of the current controller for the LC-topology with varying virtual resistance; *Left*: command tracking, *Right*: dynamic stiffness (impedance seen from grid).

the virtual resistance achieves damping at the resonance frequency when the term $L_f C_f \cdot s^2$ dominates in the denominator for this frequency. However, increasing R_{vir} further also increases the term $C_f(K_p + R_{vir}) \cdot s$, which in return can degrade the damping performance.

Figure 3.7 shows that the plant is not passive, roughly between 1 Hz and 100 Hz. The impedance is substantial in that region, which suggests this does not influence other systems. No example was found where this threatens negative cross-coupling effects. However, this phase drop is the trade-off of the active damping approach via virtual resistance based on capacitor current feedback. Filtering out these low-frequency components for the active damping could solve the problem.

The evaluation of this effect should be part of future research.

Observer

The active damping approach using capacitor current feedback – as presented in [6, 8, 10, 11, 13] – needs two different current information, the inverter current for the control and the capacitor current for the active damping. The second current measurement, however, poses a problem in many applications. Thus, an algorithm that avoids this additional measurement is very advantageous. A common approach for obtaining further state information is the implementation of an observer [79–83].

Figure 3.10 depicts a first-order Luenberger-style observer for the capacitor voltage. The observer controller's output estimates the disturbance – the grid current – and consequently can be used to estimate the capacitor current. Figure 3.11 shows the overlaid plot of the dynamic stiffness and command tracking comparing the performance using the observer's capacitor current information to actual measurement implementation with and without parameter estimation error. These plots suggest that the sensor replacement technique via a Luenberger-style observer offers a very robust alternative. Figure 3.11 further shows that

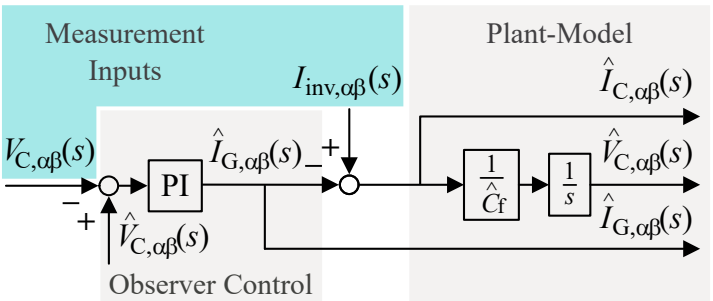

Figure 3.10: Luenberger-style observer of the capacitor voltage model of the LC-filter. The observer estimates the grid-current and the capacitor current.

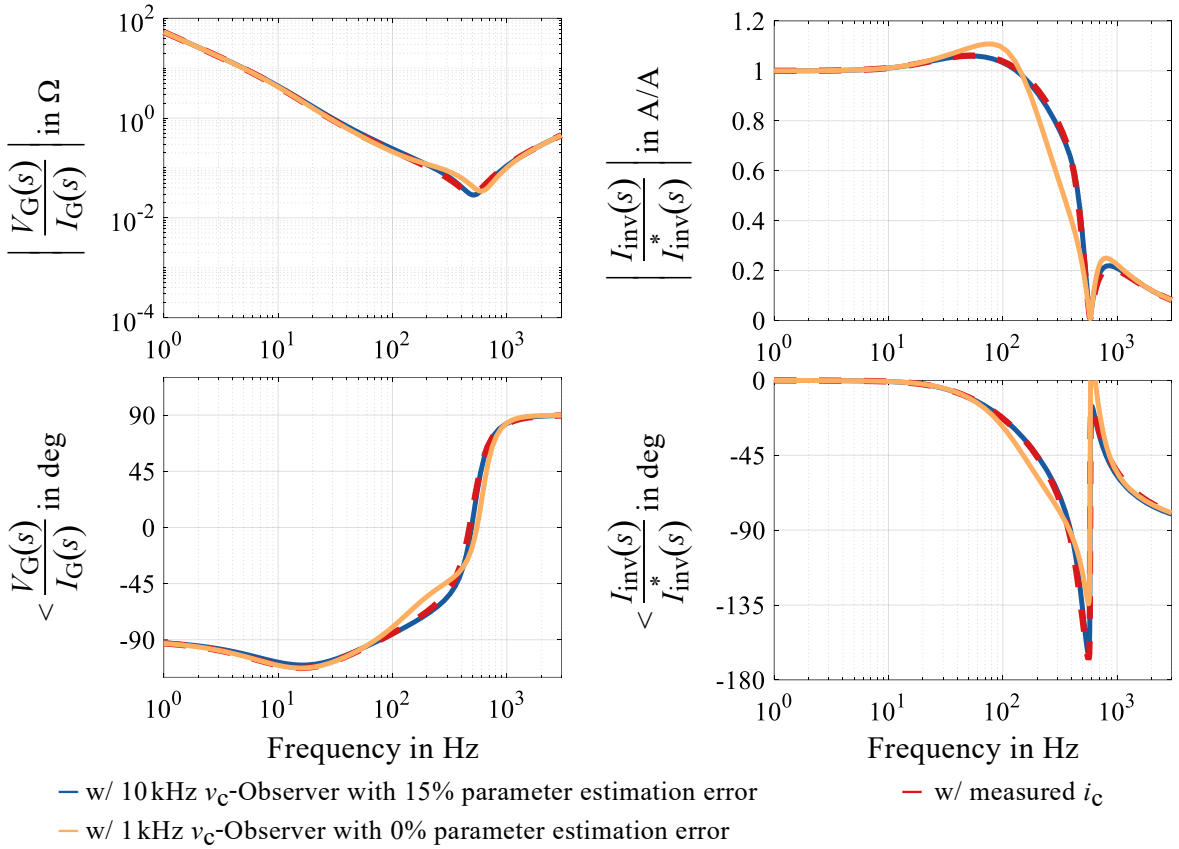

Figure 3.11: Dynamic analysis of the current controller for the LC-topology w/ and w/o v_c-observer for capacitor current estimation with large virtual resistance: *Left*: dynamic stiffness, *Right*: command tracking (note – the system is modelled with losses, thus the phase does not fully drop to –180 deg).

the bandwidth of the observer should be placed well above the resonant frequency, which seems intuitive.

3.2.2. LCL-Topology

The LCL-topology (see Figure 3.2) utilized the inverter current and voltage information after the LCL structure at the PCC. In contrast to the LC-topology, the plant seen from the inverter includes the resonance and antiresonance of the LCL structure, similar to the impedance seen from the grid (see Figure 3.4 − red).

However, until the antiresonance and resonance frequency, the plant can be approximated as a first-order L-filter with the inductance value of $L_{f1} + L_{f2}$ (see Figure 3.3). Consequently, the controller can be tuned again using (2.4) with the combined inductance.

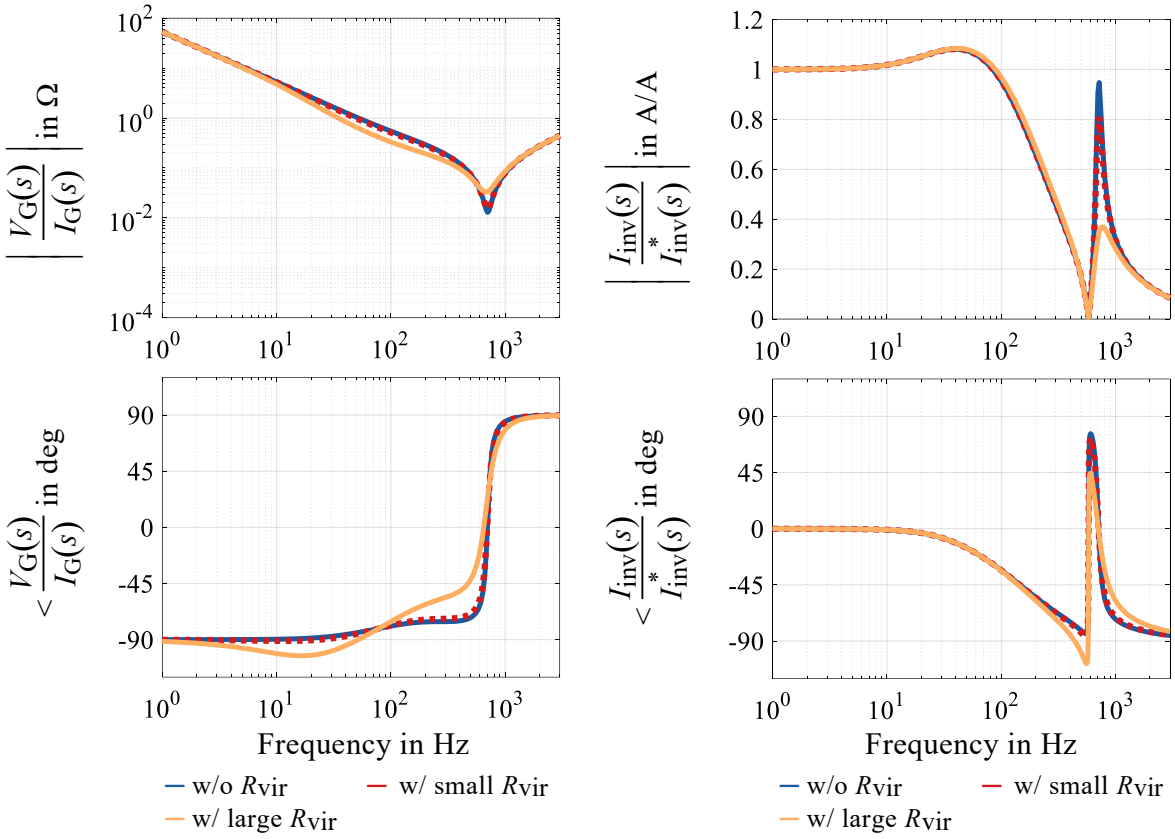

Figure 3.12: Dynamic analysis of the current controller for the LCL-topology with varying virtual resistance: *Left*: dynamic stiffness, *Right*: command tracking (note – the system is modelled with losses).

Using the same control algorithms as shown in Figure 3.6, except for a different L parameter and V_G instead of V_C for the decoupling, frequency response function plots are derived and depicted in Figure 3.12 for varying virtual resistance.

The harmonic impedance seen from the grid (dynamic stiffness) shows very similar attributes comparing the LC- (Figure 3.7) and the LCL-topology (Figure 3.12). In contrast to the LC-topology, the command tracking of the LCL-topology reveals the need for further active damping regarding the resonance. The virtual resistance achieves very efficient damping.

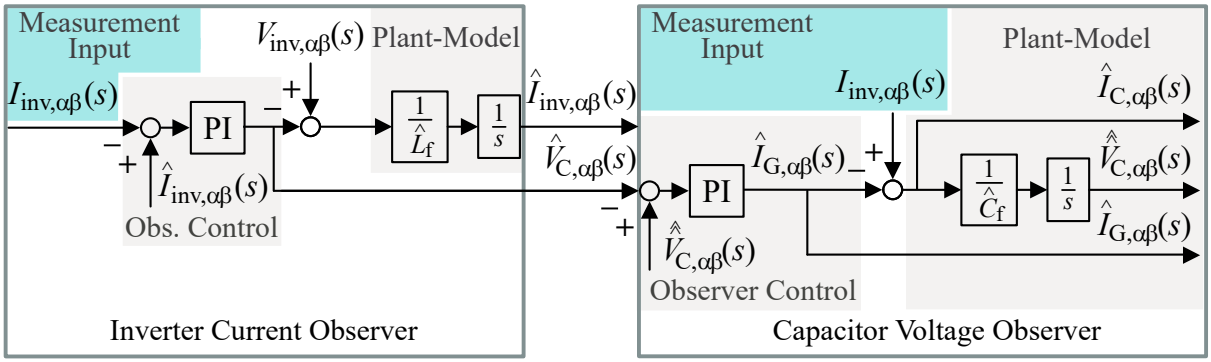

Figure 3.13: Cascaded Luenberger-style observer structure of inverter current and capacitor voltage model of the LC-filter for the LCL-topology. The observers estimate the grid-current, the capacitor voltage, and the capacitor current.

Observer

Similar to the LC-topology, a sensor replacement technique via observer would greatly benefit many applications' active damping schemes. Figure 3.13 shows a cascaded

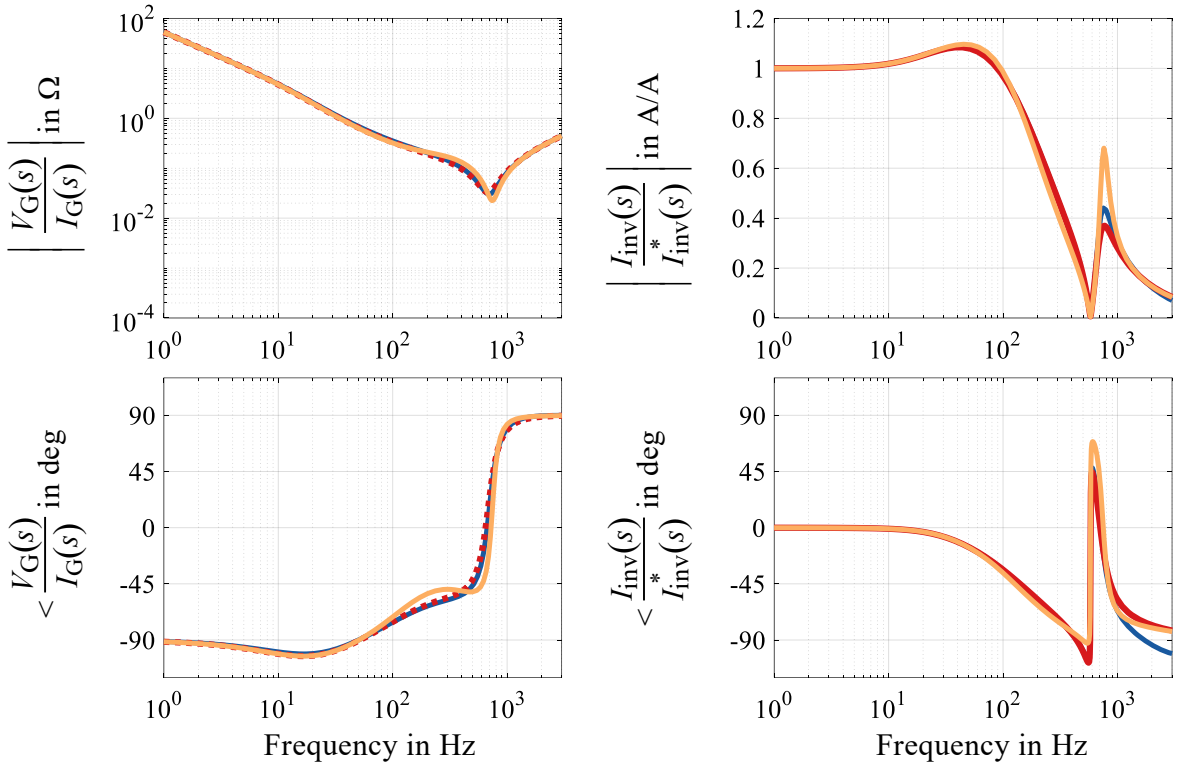

Figure 3.14: Dynamic analysis of the current controller for the LCL-topology w/ and w/o the cascaded Luenenberger-style observer for capacitor current estimation with large virtual resistance: *Left*: dynamic stiffness, *Right*: command tracking (note – the system is modelled with losses).

Luenenberger-style observer structure. This cascade uses the inverter current observer to estimate the capacitor voltage. Similar to the LC-topology, the capacitor voltage observer estimates the capacitor current.

Figure 3.14 depicts the frequency response function plots comparing simulation results to different observer setups. These dynamic plots reveal similar attributes for the LC-topology compared to the LCL-topology. Both topologies benefit greatly from high bandwidth observers but are relatively robust regarding the filter parameters. Further, none of the presented methods need any information regarding the grid impedance.

3.3. Continuous Design Conclusion

The dynamic analysis shows that the LC-topology and the LCL-topology need active damping to achieve a well-behaved harmonic impedance seen from the grid. Using the virtual resistance in series with the capacitor provides proper damping (see the grid scenario in Figure 3.15). However, the virtual resistance drops the phase at lower frequencies resulting in non-passive behavior. Though the author did not find critical examples for this setup, the consequent phase drop must be considered a trade-off. Filtering out the low-frequency components in the active damping could potentially solve this issue. Future work will investigate this effect.

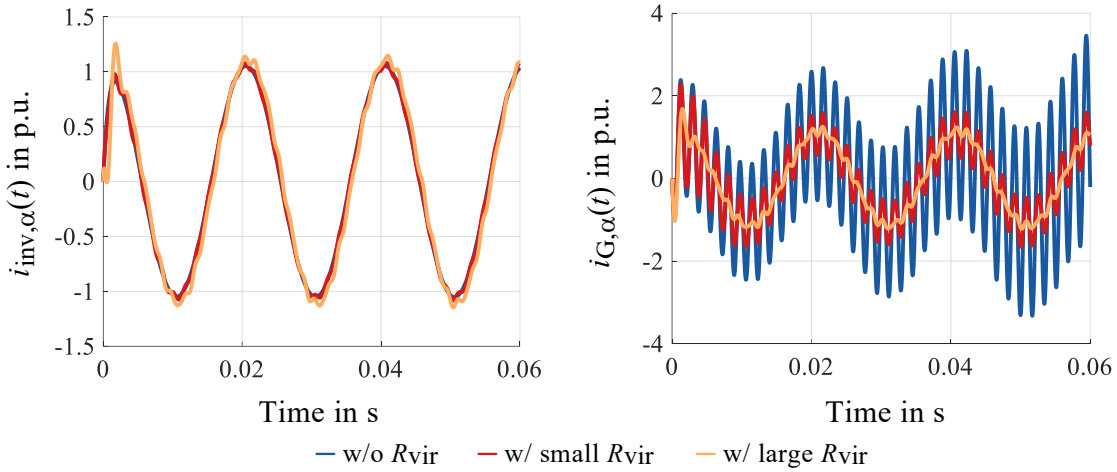

$$v_{\mathrm{G},\alpha}(t) = V_{\mathrm{max,n}}\left[\cos(\omega_{\mathrm{G}} \cdot t) + 0.03 \cdot \cos(\omega_{\mathrm{Res,LCL}} \cdot t) + 0.03 \cdot \cos(\omega_{\mathrm{Res,LC}} \cdot t)\right]$$

Figure 3.15: Time domain plot of α-axis for grid-scenario with 3 % harmonic content at LC and LCL resonant frequency for the current controller of the LC-topology with observer-based virtual resistance. Disturbance was implemented as shown in equation above.

The observer-based sensor replacement techniques (Figure 3.10, Figure 3.13) perform very effectively in the dynamic analysis. The observer is very robust regarding the filter parameters and needs no further information on the grid impedance. However, the performance of the observers deteriorates rapidly at low bandwidth. The bandwidth should exceed the resonance to be effective at the resonant frequency.

Figure 3.15 showcases the efficiency of the described active damping algorithm that uses observer-based state feedback in a time-domain plot for the LC-topology.

A first-order assumption is the basis of the tuning and design for the command tracking of the LCL-topology. In contrast, the LC-topology can be controlled like a first-order due to the capacitor voltage decoupling and thus inherently shows superior command tracking performance. The developed LCL-observer provides capacitor voltage information, as well. However, this information is only estimated and not observed and thus should not be used for disturbance input decoupling. Disturbance input decoupling with estimated information is similar to the use of flawed DID and will yield erratic attributes as illustrated in chapter 3.1.2.

The LC-topology and the LCL-topology utilize the capacitor voltage information within their observer structures to estimate the capacitor current. However, in the case of the LC-topology, this information is directly available through measurement. Consequently, the observer structure of the LC-topology is more robust.

This chapter aimed to evaluate the problems of the continuous domain of the control problem. Though the actual control operates in a discrete environment, the resonant problem itself occurs in continuous time. Thus, the insights from this chapter build a sound basis for the discrete control approach.

The next chapter focuses on discrete-time control design.

4. Discrete Design

This chapter focuses on the implementation of the concepts of chapter 3 in the discrete domain. The publications [23–25], which were published in connection with this work, highlight the issues that are unique to the z-domain. Identifying the correct direct-discrete models is crucial to obtaining effective decoupling and the consequent manipulation of the system's eigenvalues. Both presented control algorithms for the LC- and the LCL-topology base on a first-order L filter assumption after voltage decoupling. Thus, the current control design can be held out as conceptually presented in chapters 2.1.3 and 2.1.4. Equation (2.14) shows the eigenvalue placement, and Figure 2.6 illustrates the control topology.

Within the framework of this work, the University of Rostock published a discrete modeling approach and the consequent current control in [24] for the LC-topology. For simplicity, this concept is called the Rostock approach and will be laid out in the following. Another research group associated with the Aalto-University introduced a different direct discrete modeling approach in [11] in called the Aalto approach from here on (see also [21, 84–95]).

First, this chapter will describe both approaches and compare them. The two models perform very similarly – arguably with slight advantages for the Rostock approach for the LC-topology. The Rostock approach will be used onwards for the control and observer design. All parameters used for the plots and examples are shown in Table A.1 (Appendix).

4.1. Control Problem

This subchapter presents the derivation of the direct discrete model and identifies the problems that are unique to the discrete domain. This chapter models the inverter as a discrete voltage source. With this assumption, the manipulated input can be modeled as a zero-order-hold, as shown in Figure 4.2.a.

Aalto Approach

The Aalto approach [11] presents the derivation of a direct discrete model for the full state-vector $\mathbf{x} = [\boldsymbol{i}_{\mathrm{inv}}, \boldsymbol{v}_{\mathrm{C}}, \boldsymbol{i}_{\mathrm{G}}]^{\mathrm{T}}$ as shown in (4.1) – (4.3) in the dq-frame.

The phrase full state-vector describes in this work the state vector as just shown. It engulfs all states – both grid and filter currents, and the capacitor voltage. Consequently, more parameters (L_G) and state information ($\boldsymbol{i}_\mathrm{G}$) are involved in this state-space description (full LCL-topology):

$$\begin{aligned}\frac{\mathrm{d}\mathbf{x}}{\mathrm{d}t} = \mathbf{A}\,\mathbf{x} + \mathbf{B}_\mathrm{inv}\,\boldsymbol{v}_\mathrm{inv} + \mathbf{B}_\mathrm{g}\,\boldsymbol{v}_\mathrm{G} &= \begin{bmatrix} -\mathrm{j}\omega_\mathrm{g} & -\frac{1}{L_\mathrm{f}} & 0 \\ \frac{1}{C_\mathrm{f}} & -\mathrm{j}\omega_\mathrm{g} & -\frac{1}{C_\mathrm{f}} \\ 0 & \frac{1}{L_\mathrm{G}} & -\mathrm{j}\omega_\mathrm{g} \end{bmatrix}\mathbf{x} + \begin{bmatrix} \frac{1}{L_\mathrm{f}} \\ 0 \\ 0 \end{bmatrix}\boldsymbol{v}_\mathrm{inv} + \begin{bmatrix} 0 \\ 0 \\ -\frac{1}{L_\mathrm{f}} \end{bmatrix}\boldsymbol{v}_\mathrm{G} \\ \boldsymbol{I}_\mathrm{inv} &= \mathbf{C}_\mathrm{c}\,\mathbf{x} = \begin{bmatrix} 1 & 0 & 0 \end{bmatrix}\mathbf{x} \end{aligned} \tag{4.1}$$

$$\begin{aligned}\mathbf{x}[k+1] &= \boldsymbol{\Phi}\,\mathbf{x}[k] + \boldsymbol{\Gamma}_\mathrm{inv}\,\boldsymbol{v}_\mathrm{inv}[k] + \boldsymbol{\Gamma}_\mathrm{g}\,\boldsymbol{v}_\mathrm{G}[k] \\ \boldsymbol{i}_\mathrm{inv}[k] &= \mathbf{C}_\mathrm{c}\,\mathbf{x}[k] \end{aligned} \tag{4.2}$$

$$\begin{aligned}\boldsymbol{\Phi} &= \mathrm{e}^{\mathbf{A}T_\mathrm{s}} \\ \boldsymbol{\Gamma}_\mathrm{inv} &= \left(\int_0^{T_\mathrm{s}} \mathrm{e}^{\mathbf{A}\tau}\,\mathrm{e}^{-\mathrm{j}\omega_\mathrm{g}(T_\mathrm{s}-\tau)}\,\mathrm{d}\tau\right)\mathbf{B}_\mathrm{inv} \\ \boldsymbol{\Gamma}_\mathrm{g} &= \left(\int_0^{T_\mathrm{s}} \mathrm{e}^{\mathbf{A}\tau}\,\mathrm{d}\tau\right)\mathbf{B}_\mathrm{g} \end{aligned} \tag{4.3}$$

The resulting matrices $\boldsymbol{\Phi}$, $\boldsymbol{\Gamma}_\mathrm{inv}$, and $\boldsymbol{\Gamma}_\mathrm{g}$ are shown in (A.1) in the appendix.

The same approach can be used for the available reduced state-vector $\mathbf{x} = [\boldsymbol{i}_\mathrm{inv}, \boldsymbol{v}_\mathrm{c}]^\mathrm{T}$ as shown in (4.4) – (4.7) in the case of the LC-topology. The resulting matrices are shown in (4.7). Such a reduced state model is crucial for the LC-topology due to the lack of information regarding L_G, $\boldsymbol{v}_\mathrm{G}$, and $\boldsymbol{i}_\mathrm{G}$.

$$\begin{aligned}\frac{\mathrm{d}\mathbf{x}}{\mathrm{d}t} = \mathbf{A}\,\mathbf{x} + \mathbf{B}_\mathrm{inv}\,\boldsymbol{v}_\mathrm{inv} + \mathbf{B}_\mathrm{g}\,\boldsymbol{i}_\mathrm{G} &= \begin{bmatrix} -\mathrm{j}\omega_\mathrm{g} & -\frac{1}{L_\mathrm{f}} \\ \frac{1}{C_\mathrm{f}} & -\mathrm{j}\omega_\mathrm{g} \end{bmatrix}\mathbf{x} + \begin{bmatrix} \frac{1}{L_\mathrm{f}} \\ 0 \end{bmatrix}\boldsymbol{v}_\mathrm{inv} + \begin{bmatrix} 0 \\ -\frac{1}{C_\mathrm{f}} \end{bmatrix}\boldsymbol{i}_\mathrm{G} \\ \boldsymbol{i}_\mathrm{inv} &= \mathbf{C}_\mathrm{c}\,\mathbf{x} = \begin{bmatrix} 1 & 0 \end{bmatrix}\mathbf{x} \end{aligned} \tag{4.4}$$

$$\begin{aligned}\mathbf{x}[k+1] &= \boldsymbol{\Phi}\,\mathbf{x}[k] + \boldsymbol{\Gamma}_\mathrm{inv}\,\boldsymbol{v}_\mathrm{inv}[k] + \boldsymbol{\Gamma}_\mathrm{g}\,\boldsymbol{i}_\mathrm{G}[k] \\ \boldsymbol{i}_\mathrm{inv}[k] &= \mathbf{C}_\mathrm{c}\,\mathbf{x}[k] \end{aligned} \tag{4.5}$$

$$\begin{aligned}
\boldsymbol{\Phi} &= \mathrm{e}^{\mathbf{A}T_\mathrm{s}} \\
\boldsymbol{\Gamma}_\mathrm{inv} &= \left(\int_0^{T_\mathrm{s}} \mathrm{e}^{\mathbf{A}\tau}\, \mathrm{e}^{-\mathrm{j}\omega_\mathrm{g}(T_\mathrm{s}-\tau)}\, \mathrm{d}\tau \right) \mathbf{B}_\mathrm{inv} \\
\boldsymbol{\Gamma}_\mathrm{g} &= \left(\int_0^{T_\mathrm{s}} \mathrm{e}^{\mathbf{A}\tau}\, \mathrm{d}\tau \right) \mathbf{B}_\mathrm{g}
\end{aligned} \tag{4.6}$$

$$\begin{aligned}
\boldsymbol{\Phi} &= \mathrm{e}^{-\mathrm{j}\omega_\mathrm{g}T_\mathrm{s}} \begin{bmatrix} \cos\left(\omega_\mathrm{ar}T_\mathrm{s}\right) & -\omega_\mathrm{ar}C_\mathrm{f}\sin\left(\omega_\mathrm{ar}T_\mathrm{s}\right) \\ \omega_\mathrm{ar}L_\mathrm{f}\sin\left(\omega_\mathrm{ar}T_\mathrm{s}\right) & \cos\left(\omega_\mathrm{ar}T_\mathrm{s}\right) \end{bmatrix} \\
\boldsymbol{\Gamma}_\mathrm{inv} &= \mathrm{e}^{-\mathrm{j}\omega_\mathrm{g}T_\mathrm{s}} \begin{bmatrix} \sin\left(\omega_\mathrm{ar}T_\mathrm{s}\right)\omega_\mathrm{ar}C_\mathrm{f} \\ 1-\cos\left(\omega_\mathrm{ar}T_\mathrm{s}\right) \end{bmatrix} \\
\boldsymbol{\Gamma}_\mathrm{g} &= \mathrm{e}^{-\mathrm{j}\omega_\mathrm{g}T_\mathrm{s}} \frac{\omega_\mathrm{ar}^2}{\omega_\mathrm{g}^2-\omega_\mathrm{ar}^2} \begin{bmatrix} \cos\left(\omega_\mathrm{ar}T_\mathrm{s}\right) + \mathrm{j}\sin\left(\omega_\mathrm{ar}T_\mathrm{s}\right)\dfrac{\omega_\mathrm{g}}{\omega_\mathrm{ar}} - \mathrm{e}^{\mathrm{j}\omega_\mathrm{g}T_\mathrm{s}} \\ \omega_\mathrm{ar}L_\mathrm{f}\cdot\sin\left(\omega_\mathrm{ar}T_\mathrm{s}\right) + \mathrm{j}\omega_\mathrm{g}L_\mathrm{f}\left[\mathrm{e}^{\mathrm{j}\omega_\mathrm{g}T_\mathrm{s}} - \cos\left(\omega_\mathrm{ar}T_\mathrm{s}\right)\right] \end{bmatrix}
\end{aligned} \tag{4.7}$$

The Equations (4.8) and (4.9) show the implementation of the Clarke-Transformation in the discrete domain and the consequent relationship between the system matrices in the αβ- and dq-reference frames.

$$\begin{aligned}
\mathrm{e}^{-\mathrm{j}\theta_\mathrm{g}[k+1]} &= \mathrm{e}^{-\mathrm{j}(\theta_\mathrm{g}[k]+\omega_\mathrm{g}[k]T_\mathrm{s})} = \mathrm{e}^{-\mathrm{j}\theta_\mathrm{g}[k]} \cdot \mathrm{e}^{-\mathrm{j}\omega_\mathrm{g}[k]T_\mathrm{s}} \\
\mathbf{x}_{\alpha\beta}[k+1]\cdot\mathrm{e}^{-\mathrm{j}\theta_\mathrm{g}[k+1]} &= \left(\boldsymbol{\Phi}_{\alpha\beta}\mathbf{x}_{\alpha\beta}[k] + \boldsymbol{\Gamma}_{\mathrm{inv}.\alpha\beta}\boldsymbol{v}_{\mathrm{inv}.\alpha\beta}[k] + \boldsymbol{\Gamma}_{\mathrm{g}.\alpha\beta}\boldsymbol{i}_{g.\alpha\beta}[k]\right) \\
&\quad \cdot \mathrm{e}^{-\mathrm{j}\theta_\mathrm{g}[k]} \cdot \mathrm{e}^{-\mathrm{j}\omega_\mathrm{g}[k]T_\mathrm{s}} \\
\mathbf{x}_\mathrm{dq}[k+1] &= \left(\boldsymbol{\Phi}_{\alpha\beta}\mathbf{x}_\mathrm{dq}[k] + \boldsymbol{\Gamma}_{\mathrm{inv}.\alpha\beta}\boldsymbol{v}_{\mathrm{inv}.\mathrm{dq}}[k] + \boldsymbol{\Gamma}_{\mathrm{g}.\alpha\beta}\boldsymbol{i}_{g.\mathrm{dq}}[k]\right)\cdot\mathrm{e}^{-\mathrm{j}\omega_\mathrm{g}[k]T_\mathrm{s}}
\end{aligned} \tag{4.8}$$

$$\begin{aligned}
\boldsymbol{\Phi} &= \boldsymbol{\Phi}_\mathrm{dq} = \boldsymbol{\Phi}_{\alpha\beta}\cdot\mathrm{e}^{-\mathrm{j}\omega_\mathrm{g}[k]T_\mathrm{s}} \\
\boldsymbol{\Gamma}_\mathrm{inv} &= \boldsymbol{\Gamma}_{\mathrm{inv}.\mathrm{dq}} = \boldsymbol{\Gamma}_{\mathrm{inv}.\alpha\beta}\cdot\mathrm{e}^{-\mathrm{j}\omega_\mathrm{g}[k]T_\mathrm{s}} \\
\boldsymbol{\Gamma}_\mathrm{g} &= \boldsymbol{\Gamma}_{\mathrm{g}.\mathrm{dq}} = \boldsymbol{\Gamma}_{\mathrm{g}.\alpha\beta}\cdot\mathrm{e}^{-\mathrm{j}\omega_\mathrm{g}[k]T_\mathrm{s}}
\end{aligned} \tag{4.9}$$

Rostock Approach

The Rostock approach published the proposal of another method to derive reduced state-vector direct discrete models for the capacitor voltage and inverter current for the LC-topology without information of the grid-voltage in the αβ-reference frame in [24]. In this approach, the continuous capacitor-voltage and inverter-current equations are transformed into the Laplace domain – (4.10) and (4.11).

$$I_{\mathrm{inv}}(s) - I_{\mathrm{G}}(s) = V_{\mathrm{C}}(s) \cdot C_{\mathrm{f}} \cdot s - C_{\mathrm{f}} \cdot v_{\mathrm{C}}(t=0) \tag{4.10}$$

$$V_{\mathrm{inv}}(s) - V_{\mathrm{C}}(s) = I_{\mathrm{inv}}(s) \cdot (L_{\mathrm{f}}\, s + R_{\mathrm{f}}) - L_{\mathrm{f}} \cdot i_{\mathrm{inv}}(t=0) \tag{4.11}$$

After substituting the inverter voltage and the grid-current with a latched representation (zero-order hold – (4.12)), (4.10) and (4.11) are cross-solved for the inverter current and capacitor voltage:

$$V_{\mathrm{inv}}(s) = \frac{v_{\mathrm{inv}}(t=0)}{s}, \quad I_{\mathrm{G}}(s) = \frac{i_{\mathrm{G}}(t=0)}{s} \tag{4.12}$$

$$I_{\mathrm{inv}}(s) = A_1(s) \cdot v_{\mathrm{inv}}(t=0) + A_2(s) \cdot v_{\mathrm{C}}(t=0) + A_3(s) \cdot i_{\mathrm{G}}(t=0) + A_4(s) \cdot i_{\mathrm{inv}}(t=0) \tag{4.13}$$

$$V_{\mathrm{C}}(s) = B_1(s) \cdot i_{\mathrm{inv}}(t=0) + B_2(s) \cdot i_{\mathrm{G}}(t=0) + B_3(s) \cdot v_{\mathrm{inv}}(t=0) + B_4(s) \cdot v_{\mathrm{C}}(t=0) \tag{4.14}$$

Transforming (4.13) and (4.14) back into the time domain and sampling at T_{s} yields the difference equations (4.15) and (4.16), where $f[k] \triangleq f(t = kT_{\mathrm{s}})$ and $f[k-1] \triangleq f(t = (k-1)T_{\mathrm{s}})$:

$$i_{\mathrm{inv}}[k] = A_{1\mathrm{t}} \cdot v_{\mathrm{inv}}[k-1] + A_{2\mathrm{t}} \cdot v_{\mathrm{C}}[k-1] + A_{3\mathrm{t}} \cdot i_{\mathrm{G}}[k-1] + A_{4\mathrm{t}} \cdot i_{\mathrm{inv}}[k-1] \tag{4.15}$$

$$v_{\mathrm{C}}[k] = B_{1\mathrm{t}} \cdot i_{\mathrm{inv}}[k-1] + B_{2\mathrm{t}} \cdot i_{\mathrm{G}}[k-1] + B_{3\mathrm{t}} \cdot v_{\mathrm{inv}}[k-1] + B_{4\mathrm{t}} \cdot v_{\mathrm{C}}[k-1] \tag{4.16}$$

Figure 4.1 and Figure 4.2 depict the resulting z-domain models. The equations for the coefficients are given in Table 4.1.

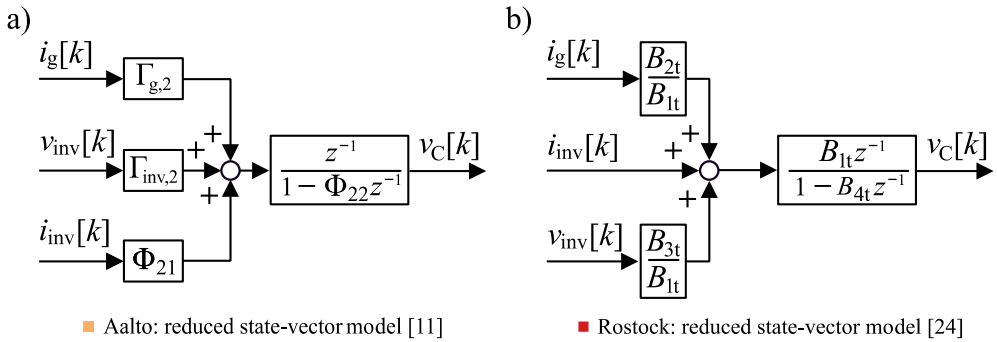

Figure 4.1: Structure of the discussed discrete reduced state-vector models. a) Aalto approach: reduced state-vector model for the capacitor voltage [11], b) Rostock approach: reduced state-vector model for the capacitor voltage via direct discrete modelling [24].

TABLE 4.1
COEFFICIENTS OF DIFFERENCE EQUATIONS [24]

Coefficient	Equation		Coefficient	Equation
H_1	$\sinh\left(\frac{T_s\sqrt{C(CR^2-4L)}}{2LC}\right)\frac{\sqrt{C}\ \mathrm{e}^{-T_s/(2\tau)}}{\sqrt{CR^2-4L}}$		A_{4t}	$H_2 - H_1R$
H_2	$\cosh\left(\frac{T_s\sqrt{C(CR^2-4L)}}{2LC}\right)\mathrm{e}^{-T_s/(2\tau)}$		B_{1t}	$2H_1\frac{L}{C} \overset{R=0}{\Longleftrightarrow} -B_{2t}$
τ	L/R		B_{2t}	$H_1\frac{CR^2-2L}{C} + H_2R - R$
A_{1t}	$2H_1$		B_{3t}	$1 - H_1R - H_2$
A_{2t}	$-2H_1 = -A_{1t}$		B_{4t}	$H_1R + H_2$
A_{3t}	$1 - H_1R - H_2$		A_{2t}/A_{1t}	-1

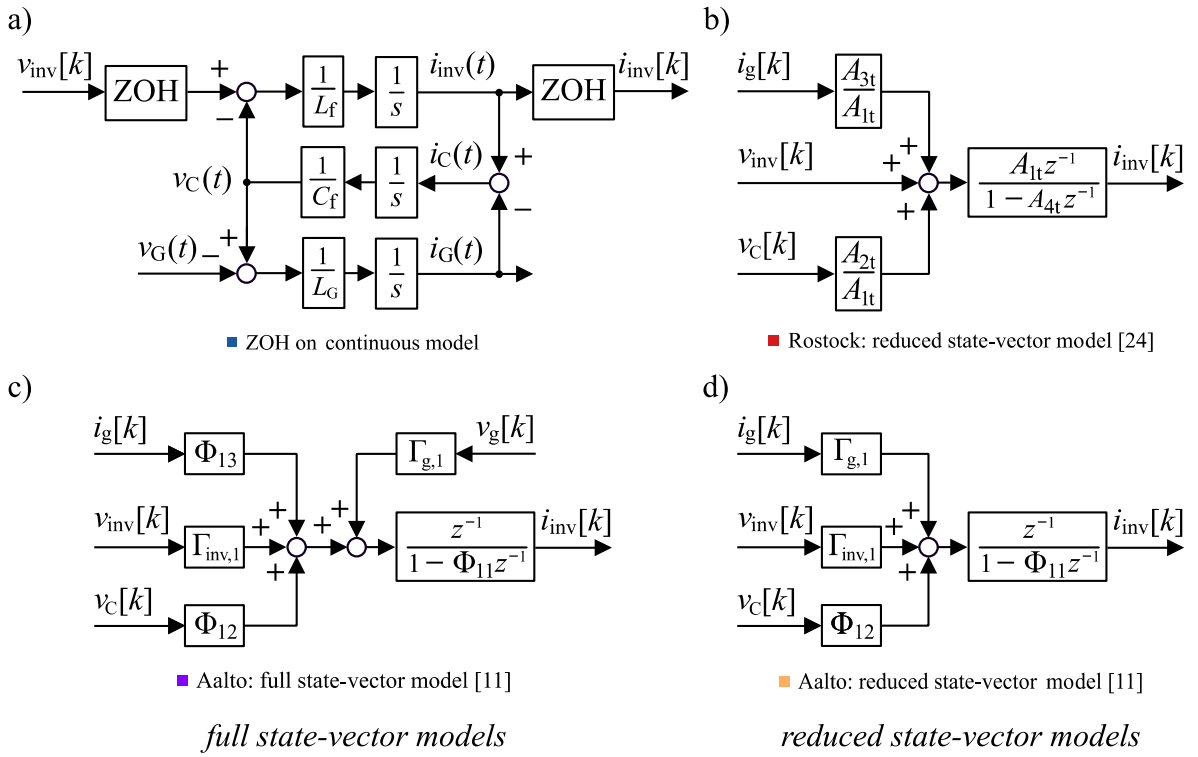

Figure 4.2: Structure of the discussed discrete models. a) zero-order representation of the inverter within the continuous system, b) Rostock: reduced state-vector model for the inverter current via direct discrete modelling [24], c) Aalto: full state-vector model for the inverter current [11], and d) Aalto reduced state-vector model for the inverter current [11].

Figure 4.3 and Figure 4.4 respectively show a time-domain plot and a frequency-domain plot for comparison of the direct discrete z-domain models to the continuous model with a discrete voltage source.

Both the time-domain and frequency-domain plots show that the Aalto discrete full vector-state model presented in [11] overlaps with the zero-order representation of the inverter voltage. Both reduced state-vector models (Aalto [11] and Rostock [24]) overlap with the discrete voltage source model up until the resonance frequency and start to deviate slowly above the resonance frequency. Therefore, this approximation should suffice to control up until the resonance and dampen the resonance itself.

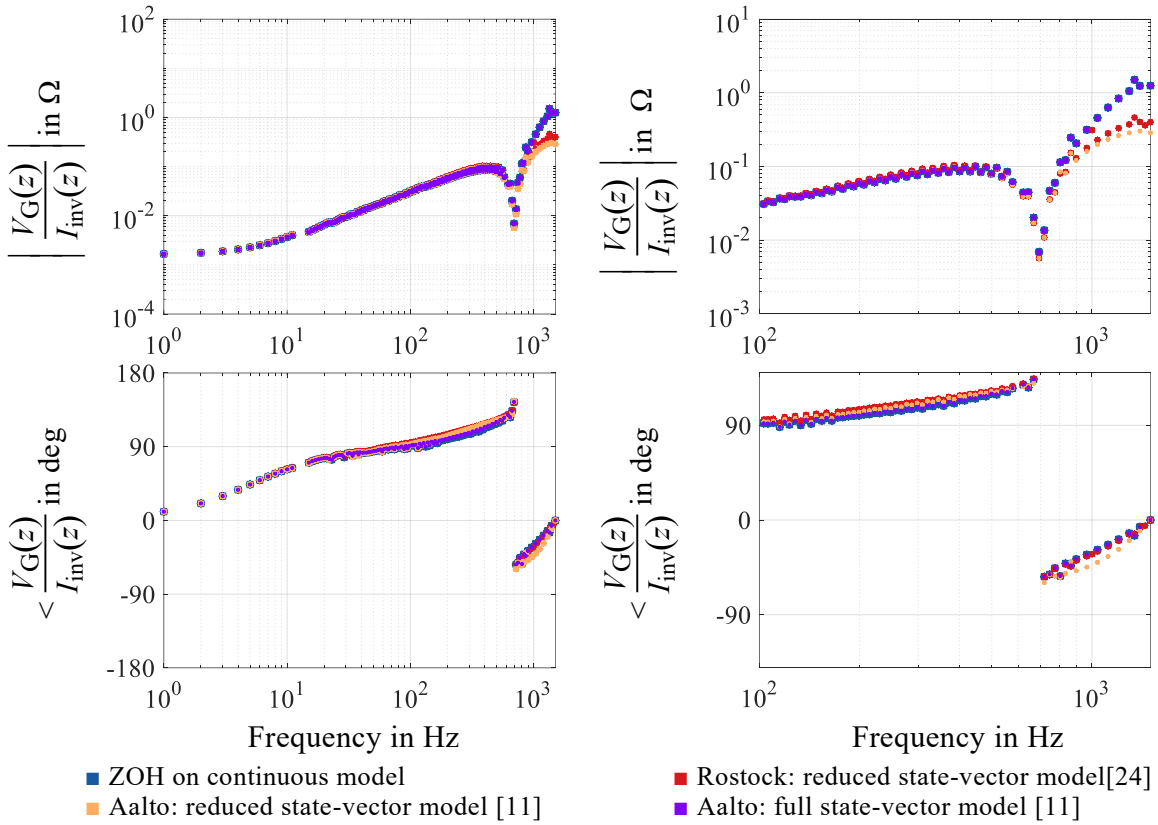

Figure 4.3: Comparison of the discussed discrete models ([11] and [24]) with the reference zero-order representation of the reference inverter with f_s = 3 kHz. Both subfigures illustrate the frequency response function of $V_G(z)/I_{inv}(z)$. The right subfigure illustrates a zoom of the dynamic behavior around the resonant frequency.

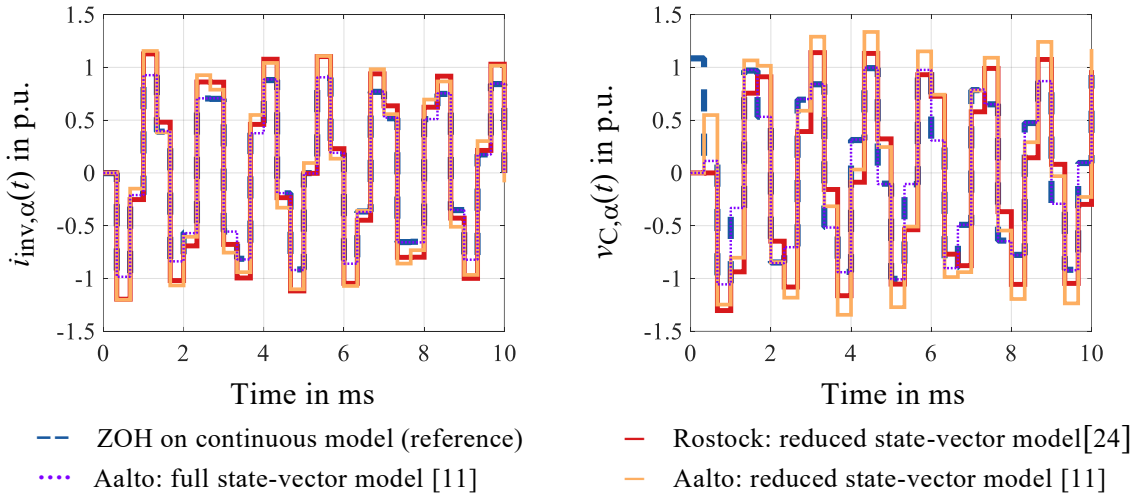

Figure 4.4: Comparison of the discussed discrete models ([11] and [24]) with the zero-order representation of the reference inverter with f_S = 3 kHz, left: inverter current time domain plot; right: capacitor voltage time domain plot. The resonant of the plants at app. 700 Hz is excited by 1 % of the nominal grid voltage. All other voltages are set to zero.

In conclusion, the reduced state-vector models closely describe the discrete-voltage approximation system up until the resonance frequency – with a slight deviation above the resonance. A full state-vector model is not applicable without the information of L_G, $\boldsymbol{v}_G$, and $\boldsymbol{i}_G$. Thus, the shown reduced-state vector models are an excellent basis for the control design for the LC-topology.

Both methods of Aalto and Rostock are similar in the mathematical approach. In the Rostock strategy, the resistance of the L-filter is included, and the grid-current as disturbance is slightly differently implemented (as a latched approximation). In comparison, the reduced state-vector approaches of Rostock and Aalto perform very similarly. The Rostock approach does show slightly closer tracking of the reference model. The full state-vector model of Aalto University is used in the following for analysis of the overall system and to dissect problems with the grid-impedance. However, for the control and observer design, the reduced state-vector models of the University of Rostock are utilized.

The Rostock approach is also applicable for a full-state vector model. In that case, the latch approach would be applied to the inverter and grid voltage instead. Since the Aalto approach shows perfect tracking already, introducing the Rostock full-state model is not necessary for the analysis of this paper.

4.2. Control Design

4.2.1. Open-Loop

Active Damping

Using the full-state model [11], (4.17) is solved for the inverter current and voltage to yield (4.18), showing the open-loop transfer function of the system before any decoupling. The coefficients, including the active damping via R_{vir}, are given in (A.2) in the appendix chapter.

Figure 4.5 and Figure 4.6 show the influence of the virtual resistance implementation on the poles-zero map. The oscillatory poles p_1 and p_2 increase both in frequency and damping with increased active damping. However, after p_1 and p_2 are fully damped, p_1 moves quickly out of the unit circle, resulting in instability of the system. p_3, and the antiresonant zeros z_1 and z_2 remain stationary with respect to the damping coefficient.

$$\begin{bmatrix} \boldsymbol{I}_{\mathrm{inv}}(z) \\ \boldsymbol{V}_{\mathrm{c}}(z) \\ \boldsymbol{I}_{\mathrm{g}}(z) \end{bmatrix} = \begin{bmatrix} \phi_{11} & \phi_{12} & \phi_{13} \\ \phi_{21} & \phi_{22} & \phi_{23} \\ \phi_{31} & \phi_{32} & \phi_{33} \end{bmatrix} \begin{bmatrix} \boldsymbol{I}_{\mathrm{inv}}(z) \\ \boldsymbol{V}_{\mathrm{c}}(z) \\ \boldsymbol{I}_{\mathrm{g}}(z) \end{bmatrix} \cdot z^{-1} + \begin{bmatrix} \gamma_{\mathrm{inv1}} \\ \gamma_{\mathrm{inv2}} \\ \gamma_{\mathrm{inv3}} \end{bmatrix} \boldsymbol{V}_{\mathrm{inv}}(z) \cdot z^{-1} \tag{4.17}$$

$$\frac{\boldsymbol{I}_{\mathrm{inv}}(z)}{\boldsymbol{V}_{\mathrm{inv}}(z)} = \frac{C_1 \cdot z^3 + C_2 \cdot z^2 + C_3 \cdot z + C_4}{z^4 + D_1 \cdot z^3 + D_2 \cdot z^2 + D_3 \cdot z + D_4} \tag{4.18}$$

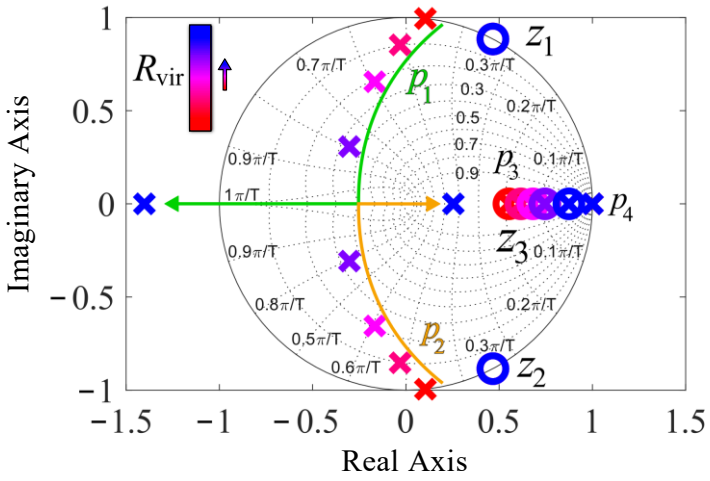

Figure 4.5: Pole-zero map of the discrete full-state vector plant model $I_{\mathrm{inv}}(z)/V_{\mathrm{inv}}(z)$ with f_{s} = 3 kHz, without decoupling and with varying active damping coefficient R_{vir}.

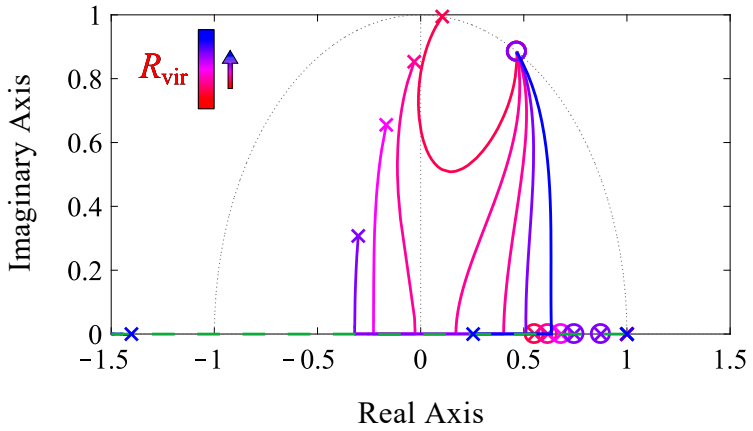

Figure 4.6: Zoomed root-locus of the discrete full-state vector plant model $I_{inv}(z)/V_{inv}(z)$ with f_S = 3 kHz without decoupling and with varying active damping coefficient R_{vir}.

In conclusion, the virtual resistance can strongly dampen the resonance poles, but overdamping can yield instability. In consequence, the damping coefficient has to be chosen adequately. Further, (A.2) shows that the pole starting positions depend on the grid impedance. However, the decoupling of the capacitor voltage minimizes this influence.

Decoupling Techniques

Chapter 3.1 outlines the concept of capacitor voltage decoupling in the continuous domain. Figure 3.7 illustrates that this decoupling transforms the controlled plant to a first-order L-filter system. However, decoupling the capacitor voltage similarly in the discrete domain does not decouple all cross-coupling from the grid-side, as seen in (4.15) and (4.16), and Figure 4.2. The cross-coupling of the grid current into the inverter-current difference-system remains – $I_{inv}(z) \neq f(V_C(z))$, but $I_{inv}(z) = f(I_G(z))$.

Figure 4.7 depicts the open-loop d-axis voltage step-response of the plant with various decoupling implementations. For similar decoupling as the continuous design of chapter 3, a first-order PT1-response for the d-axis current with close to zero reaction in q-axis current has to be achieved for this step test.

The current dq cross-coupling is calculated with the same concept of (4.9) yielding:

$$\mathrm{CCSFb} = \mathrm{j} \cdot \mathrm{Im}\left\{ \mathrm{e}^{-\mathrm{j}\omega_g[k]T_S} \cdot A_{4t}/A_{1t} \right\} = -\mathrm{j} \cdot \sin(\omega_g[k]T_S) \cdot A_{4t}/A_{1t} \tag{4.19}$$

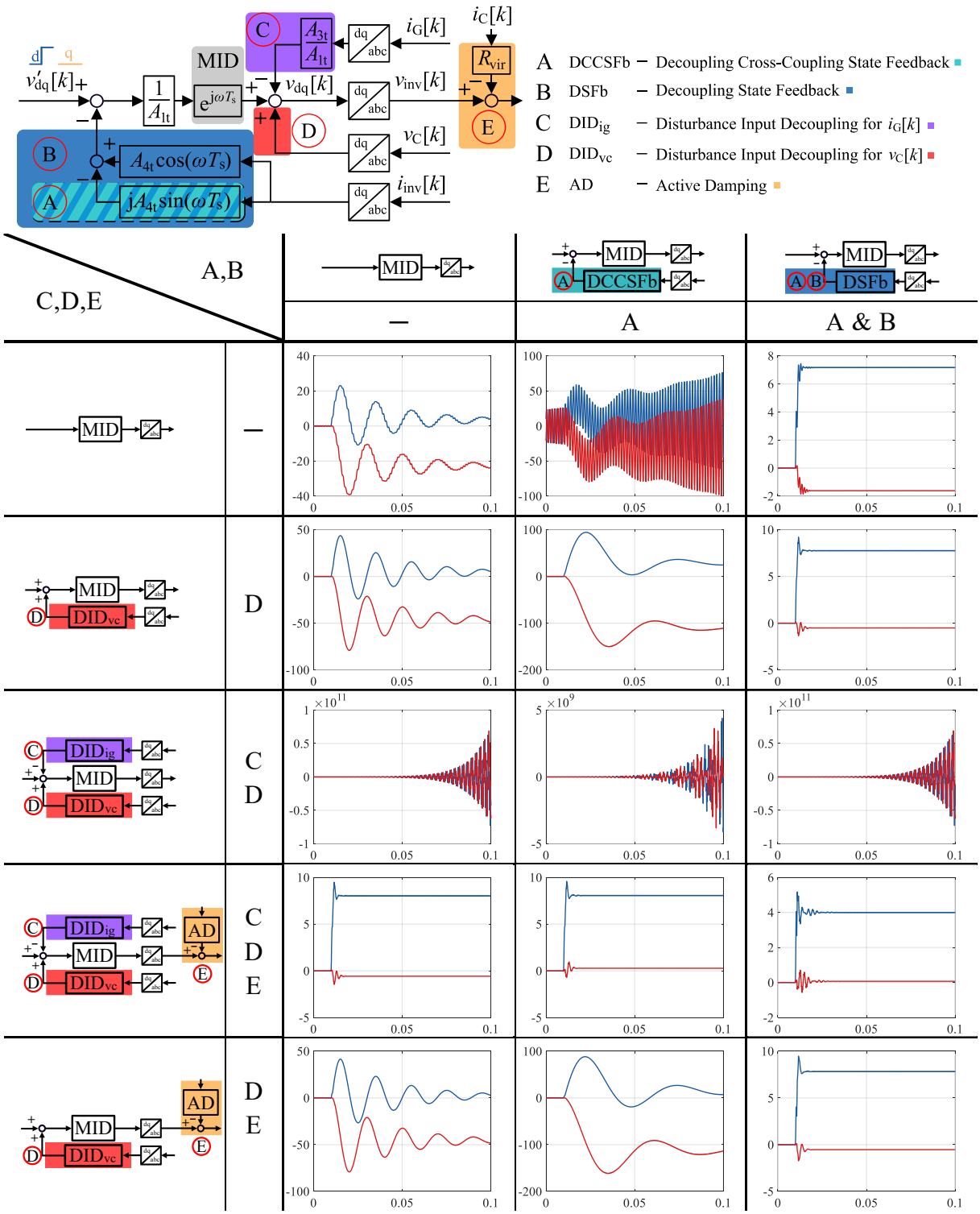

Figure 4.7:Open-loop step response of the LC-filter plant (f_S = 3 kHz) with various decoupling techniques (blue: d-current, red: q-current): A – decoupling cross-coupling state feedback, B – full decoupling state feedback, C – disturbance input decoupling for the grid current, D – disturbance input decoupling for the capacitor voltage, and E – active damping implementation; y-axis is the d-current in blue and q-current in red in kA, x-axis is time in s. Parameters in Table A.1 (Appendix).

The zero q-current reaction during this test demonstrates correct dq decoupling. While in the continuous domain, this zero reaction is achieved by the dq-current decoupling cross-coupling state feedback (continuous: $\mathrm{j}\omega L$, discrete: $-\mathrm{j}\cdot\sin(\omega T_\mathrm{s})\cdot A_{4\mathrm{t}}/A_{1\mathrm{t}}$), the discrete version also decouples a voltage cross-coupling via the manipulated input decoupling ($\mathrm{e}^{\mathrm{j}\omega T_\mathrm{s}}$ derived according to (4.9)). For more detail on the comparison of continuous and discrete decoupling techniques, the interested reader may refer to [23], which was published in connection to this work.

The PT1-reaction during this open-loop d-voltage step test represents the correct grid-decoupling (disturbance input decoupling). As shown in chapter 3 (Figure 3.5), correct disturbance input decoupling reduces the plant to a first-order RL, which in return shows only PT1-alike responses.

Six decoupling combinations of Figure 4.7 yield plant reactions that come close to this goal. The combinations with full decoupling state feedback (A & B) achieves the PT1-behavior even without grid-current information. A similar comparison between different decoupling techniques was published during this work in [23] for the RL-load. With the full state-feedback decoupling, the plant shows deadbeat-alike attributes. For the RL-load – as shown in [23] – the dynamic responses indicate that this approach is very sensitive to delay times. The combination of decoupling cross-coupling state-feedback (A), both types of disturbance input decoupling techniques (C – for $i_\mathrm{g}[k]$ and D – for $v_\mathrm{c}[k]$), and active damping (E) resemble a similar design approach to the continuous design of chapter 3 and shows less q-current reaction compared to the same combination without decoupling cross-coupling state-feedback (see also Figure 4.8).

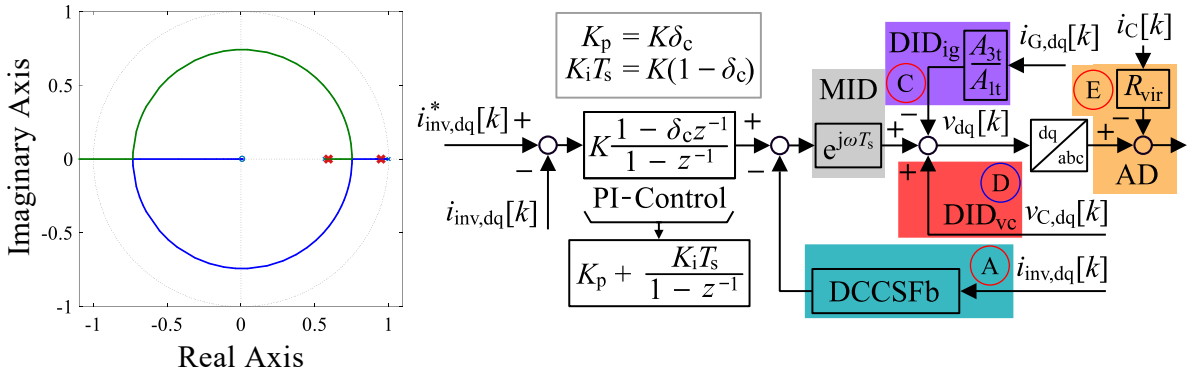

Figure 4.8: Discrete current control design in the dq-reference frame ($f_\mathrm{s} = 3\,\mathrm{kHz}$). *Left*: The open-loop root locus of the controlled plant in blue/green with the final pole locations in red. *Right*: Block diagram of the implemented control strategy with DID (disturbance input decoupling), DCCSFb (decoupling cross-coupling state-feedback: $-\mathrm{j}\cdot\sin(\omega T_\mathrm{s})\cdot A_{4\mathrm{t}}/A_{1\mathrm{t}}$), AD (active damping – R_vir), and MID (manipulated input decoupling: $\mathrm{e}^{\mathrm{j}\omega T_\mathrm{s}}$).

In conclusion, the latter combination (A, C, D, E in Figure 4.7, also Figure 4.8) was chosen as the basis of the control design since similar attributes to the continuous case were achieved. The complete control scheme in separate d- and q-axis is shown again in Figure 5.4. However, the full state-feedback decoupling (A & B in Figure 4.7) seems very promising and should be investigated further apart from this work.

Figure 9.1 and Figure 9.2 in the appendix chapter respectively illustrate the command tracking and dynamic stiffness attributes for the closed-loop control with the various decoupling techniques. Some of the methods do not yield stable operation, and thus, no plot is displayed.

4.2.2. Current Controller

After decoupling the grid voltage and the grid current, the plant model can be approximated to (4.20). Similar to the EV placement of subchapter 2.1.3 and (2.14), (4.21) illustrates the tuning for this plant with a PI controller with a gain of K and a zero placed at δ_c.

$$\frac{I_{inv}(z)}{V_{inv}(z)} = \frac{A_{1t}z^{-1}}{1 - A_{4t} \cdot \cos(\omega T_s)z^{-1}} \tag{4.20}$$

$$\text{EVs:} \quad p_{1/2} = -\frac{A_{1t}K - 1 - A_{4t} \cdot \cos(\omega T_s)}{2} \pm \sqrt{\left(\frac{A_{1t}K - 1 - A_{4t} \cdot \cos(\omega T_s)}{2}\right)^2 - A_{4t} \cdot \cos(\omega T_s) + A_{1t}K\delta_c} \tag{4.21}$$

Figure 4.8 (left) shows the root locus of the given plant for the chosen controller zero δ_c. The gain K subsequently tunes the eigenvalues to the final values as indicated in red. These separated eigenvalues are chosen similar to the continuous design of chapter 3.2 (well separated with the higher eigenvalue representing the bandwidth of the control).

Figure 4.8 (right) presents the full implementation of the active damping, the decoupling techniques, and the current controller. Figure 4.9 shows dynamic stiffness and command tracking plots for different active damping coefficients R_{vir} in the discrete domain. Note, the command tracking can only be obtained within the discrete domain. As the grid voltage and grid current both are continuous signals, dynamic stiffness can be obtained in the continuous domain even for a discrete control system.

Further, the discrete space distorts the angle information as it warps the continuous pole-zero space onto the unit circle. Therefore, continuous frequency response estimation plots are necessary to evaluate passivity. For the sake of design and comparison to the continuous control design, the dynamic stiffness plots of the discrete current control are assessed and depicted in the continuous space in this chapter. In the actual lab setup, these continuous measurements are obtainable but not implemented yet.

Comparing the results of the discrete design (Figure 4.9) with the results of the continuous design (Figure 3.7) shows very similar outcomes. Comparable effective damping is achieved but at the cost of negative real components of the impedance seen from the grid. The non-passive regions do feature a very high impedance value, though. The showcased control algorithm utilizes the grid-current information. The LC-topology assumption does not include the measurement of the grid current, and thus, a discrete representation of the observer shown in chapter 3.2.1 and Figure 3.10 is designed in the following subchapter.

4.2.3. Discrete Luenberger-Style Observer

This chapter presents a discrete representation of the Luenberger-style observer of chapter 3.2.1 and Figure 3.10.

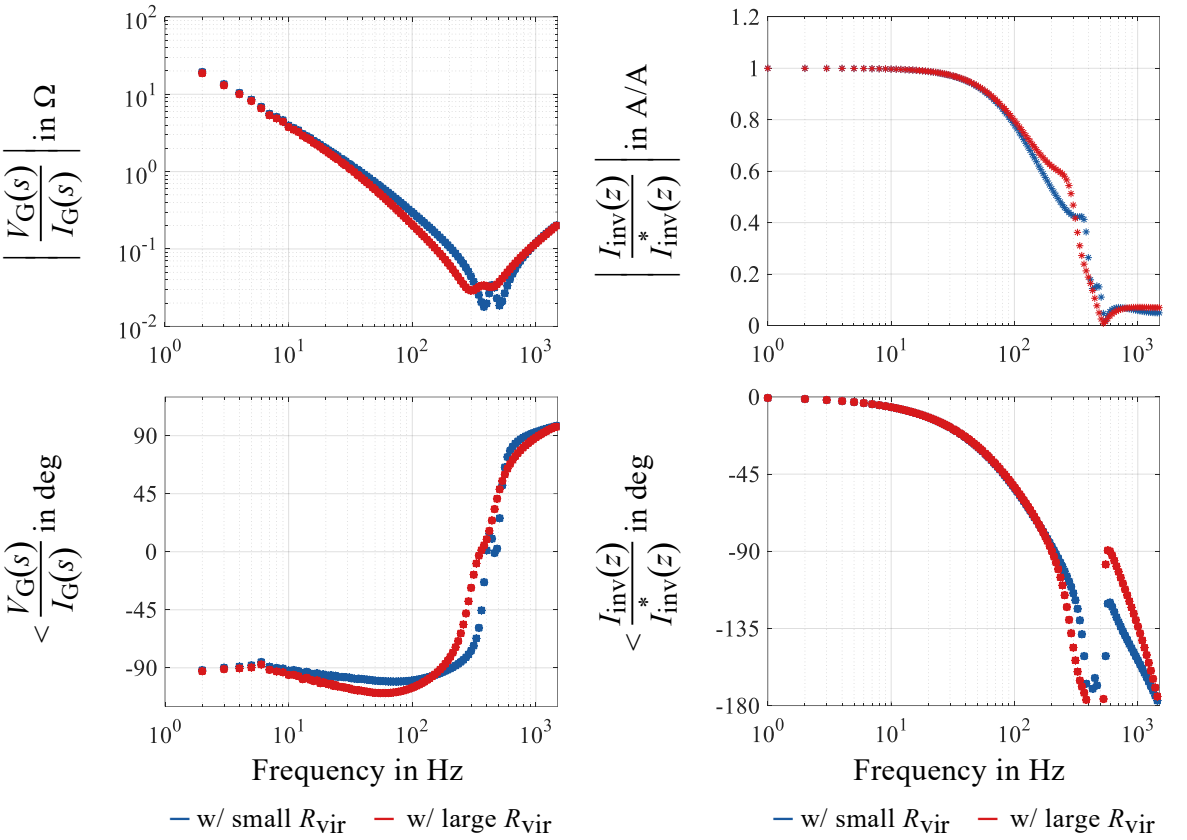

Figure 4.9: Dynamic analysis of the discrete current controller (3 kHz samping) for the LC-toplogy with different virtual resistances for active damping: *Left*: dynamic stiffness, *Right*: command tracking. Small and large virtual resistances describes R_{vir} in the red and purple region of Figure 4.5, respectively.

Figure 4.10 illustrates the basic structure of the discrete Luenberger-style observer within the overall current control scheme. The observer is based on the reduced state-vector model of chapter 4.1 – equation (4.16) − without the grid-current component. Consequently, the observer controller inherently estimates this component. With (4.16), an estimate of the grid current is calculated and used for the decoupling techniques and active damping, as shown in Figure 4.8.

Different parameter estimation errors are introduced into the control design for robustness analysis. The error is implemented for the plant′s resistance, inductance, and capacitance parameters. Further, the error is applied such that the deviance in the time constants is maximized, i.e., when estimated inductances increase with error, capacitance estimates increase as well, and resistance estimation decrease. Consequently, the calculated eigenvalues move strongly with the estimation error. Thus, the control design approach of Figure 4.8 and (4.21) cannot be applied in the same way for various cases yielding similar pole-zero placement. However, using a pole-zero cancellation technique instead, i.e., $\delta_c = A_{4t} \cdot \cos(\omega T_s)$, $K = \left(1 - e^{-j2\pi f_{br} T_s}\right) / A_{1t}$ achieves dynamic plots with better comparability.

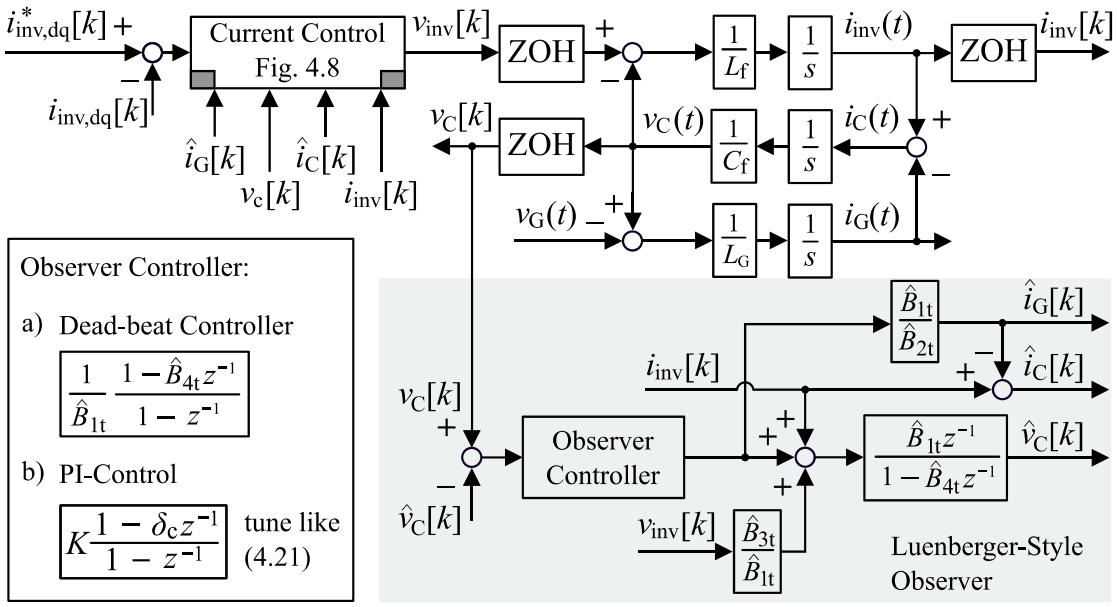

Figure 4.10: Discrete current control using a discrete Luenberger-style observer of the capacitor voltage model of the LC-filter. The observer estimates the grid-current and consequently the capacitor current.

Figure 4.11 presents the frequency response functions of the controlled system with dead-beat observer-based grid-current estimation for different parameter estimation errors. The plots indicate robust dynamic attributes and a well-damped system similar to the continuous results shown in chapter 3.2.1 – Figure 3.11.

Figure 4.12 further shows comparable results for the same dynamic plots in the case of a PI-controller-based observer. However, similar to the continuous case, faster tuning of the observer results in more robust control and a dynamically better behaved system. The disadvantage of faster tuning is the reduced noise filter capabilities of the observer.

4.3. Discrete Design Conclusion

Chapter 3 presented an analysis of the control problem. That chapter further laid out the control scheme's goals, showed the realization in the continuous domain, and therefore

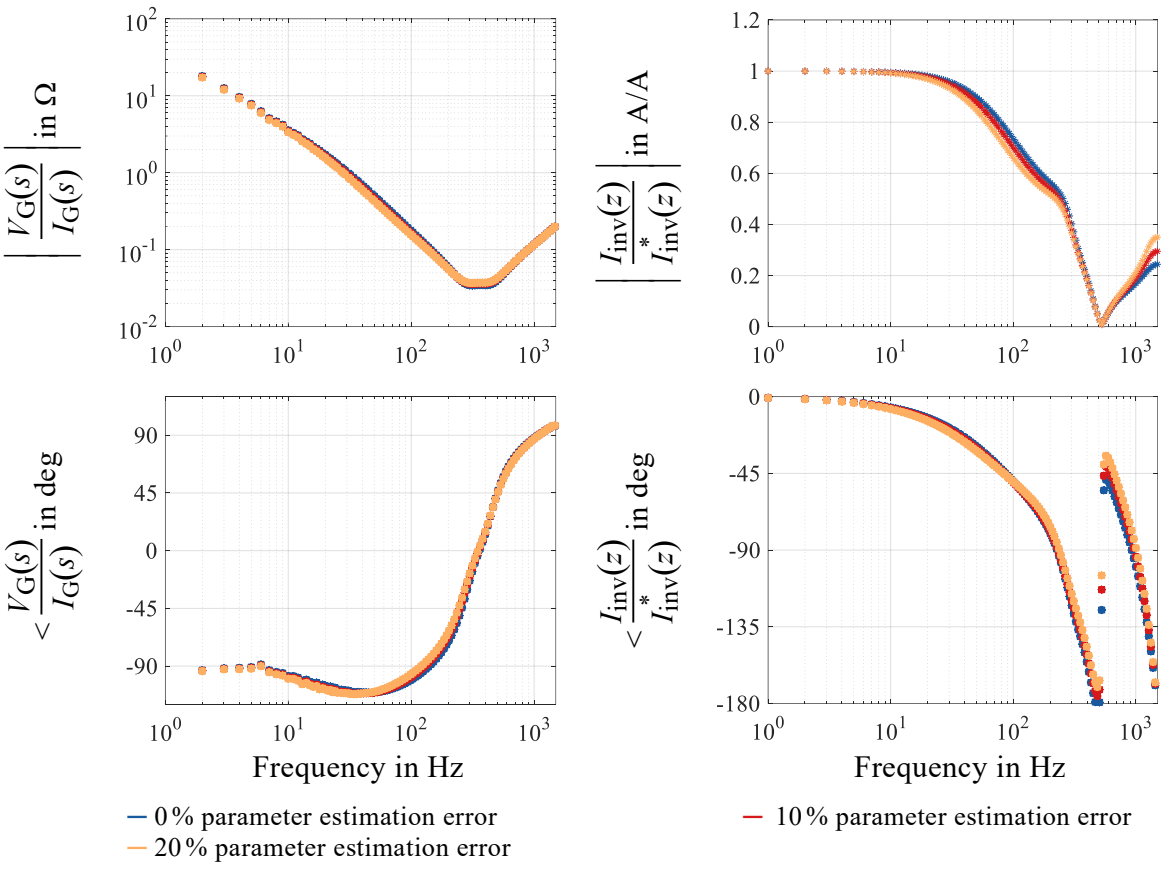

Figure 4.11: Dynamic analysis of the discrete current controller ($f_S = 3\,\text{kHz}$) for the LC-topology with active damping using a dead-beat discrete Luenberger-style observer for grid-current estimation: *Left*: dynamic stiffness, *Right*: command tracking.

serves as a reference for the control design in the discrete environment. In addition, this chapter presented the discrete modeling, the consequent decoupling techniques, the implementation of active damping similar to the continuous method, the current control implementation, and the observer design. Further, dynamic analysis (command tracking and dynamic stiffness/passivity) and robustness analysis are provided for the control system. The control achieves similar dynamic attributes in all these steps compared to the continuous reference. The results present a dynamically well-behaved, well-damped, and robust control technique of LC filters without grid-impedance information.

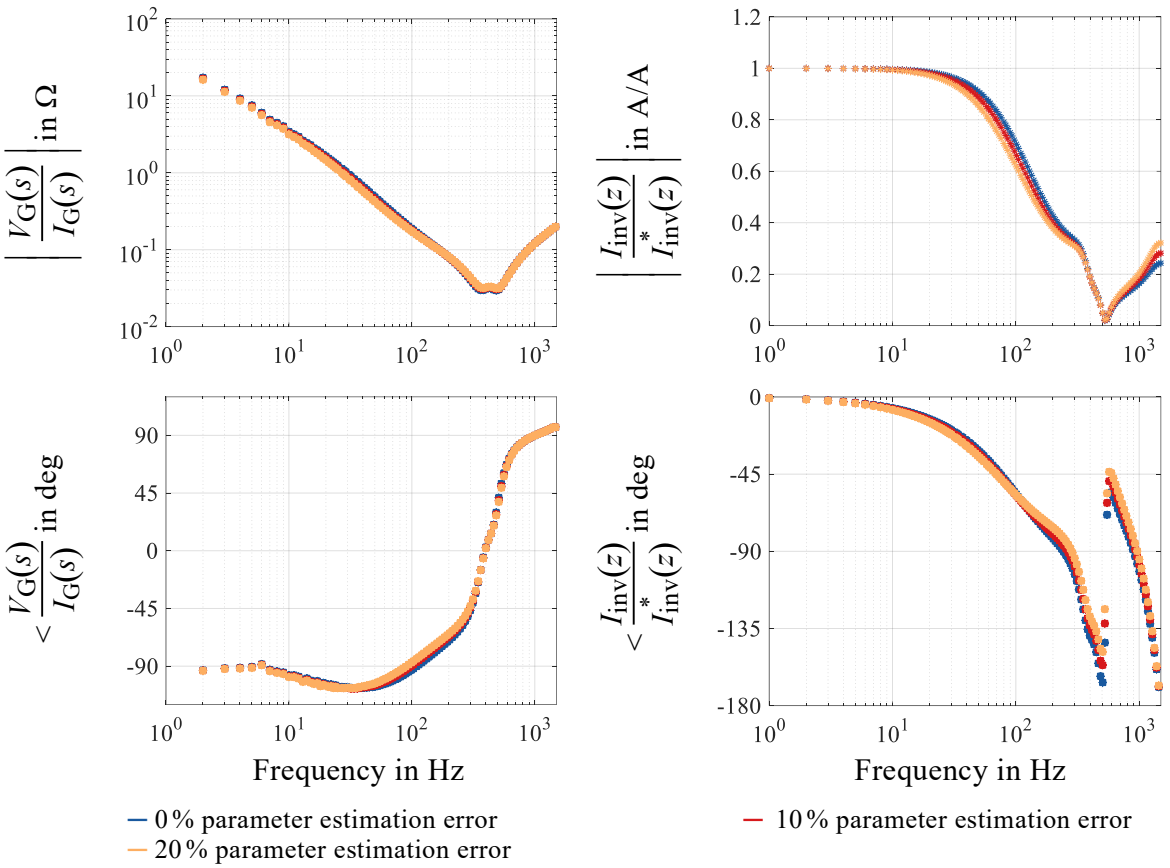

Figure 4.12: Dynamic analysis of the discrete current controller ($f_s = 3$ kHz) for the LC-topology with active damping using a 300 Hz PI-controller-based discrete Luenberger-style observer for grid-current estimation: *Left*: dynamic stiffness, *Right*: command tracking.

The following chapter presents further control issues that stem from the hardware implementation process. The main problems are the computational delay and the PWM-based inverter as voltage source instead of this chapter's perfect discrete voltage source approximation. The delay alone causes an 84° phase of the capacitor current feedback regarding the resonance frequency for the given parameters, which mitigates all active damping.

5. Implementation Space Design

The previous chapters provide physical insights into the control problem, the tools necessary for accurate discrete modeling, and control design for implementation on a microcontroller-based platform. However, the full complexity of the system – including the actual switches, PWM, delay times, the PLL (*Phase-Locked Loop*), sensor noise, filters, saturation effects, etc. – is not yet encompassed in these simulation models. Therefore, the final validation should be held out in actual hardware. However, in simulations, most of these effects can be introduced into the model. Moreover, simulations can separate these issues and analyze the influence one at a time.

This chapter will focus on implementing and analyzing the computational delay and the PWM, which strongly influence the system's dynamics. Simulations can evaluate these two implementation issues separately.

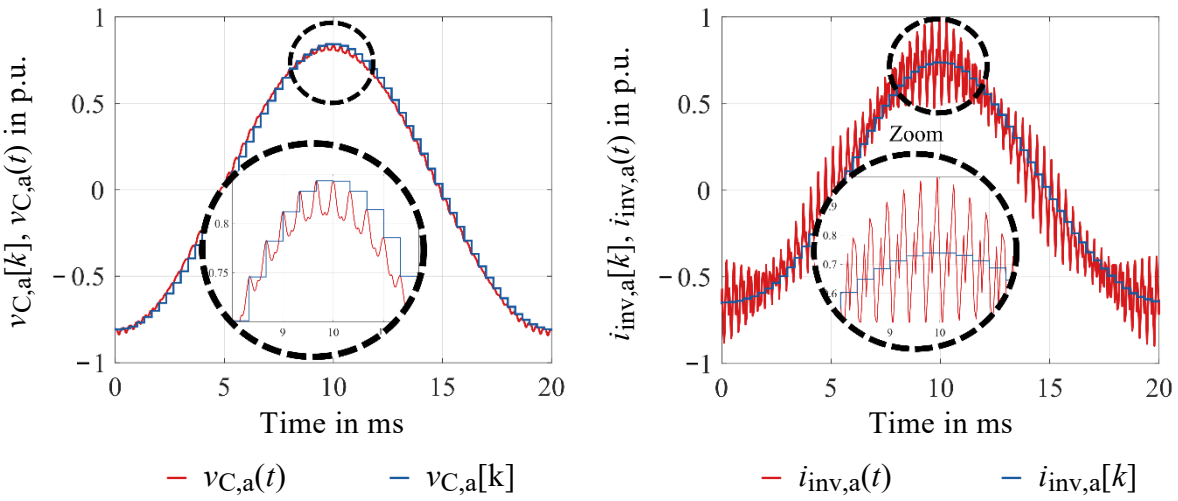

Figure 5.1: Comparison of sampled values with actual continuous raw signal with single-sampling. *Left*: Sampling capacitor voltage at PWM extrema yields errors; *Right*: Sampling inductor current at PWM extrema filters out switching ripple with minimized error.

5.1. Computational Delay

The publications [19, 45] describe that the current at an inductive load driven by a PWM-based inverter should be sampled at the extrema of the PWM. This sampling timing filters out the fundamental switching harmonic during the analog to digital conversion (see Figure 5.1). This ripple is inevitable, and picking it up would cause the controller to react to it, increasing harmonics and distortion.

The update of the voltage could occur in between these sampling instances. Since this delay changes the system's dynamics (see modified z-transform [96]), the delay should be kept constant, though. Further, updating in between the extrema can cause double switching (changes harmonic spectrum/switching frequency). Therefore, the most common approach is updating the reference at the current sampling instances (i.e., at the extrema of the PWM-carrier) but delayed by one sampling period (Figure 5.2).

Since the switches turn on during one flank of the PWM-carrier and switch off during the other, sampling and updating the reference twice per PWM-carrier period is possible

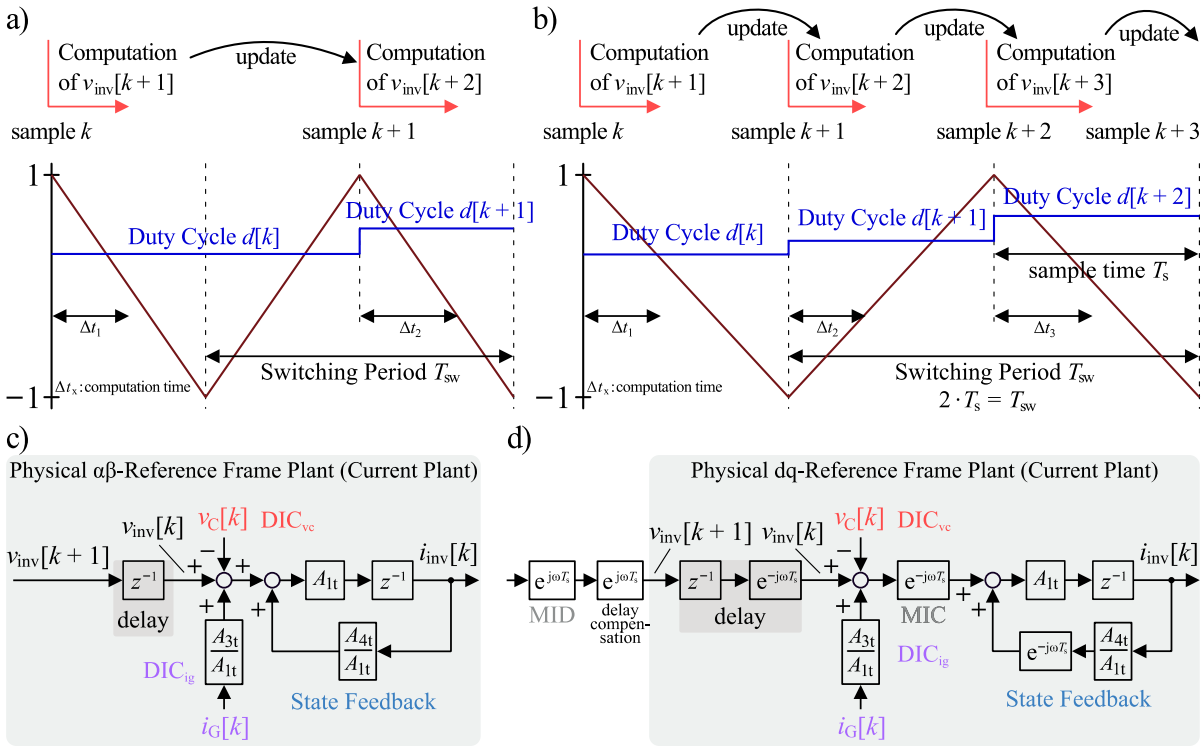

Figure 5.2: Model of the computational delay of the inverter system. a) time diagram of single-sampling, b) time diagram of double-sampling, c) z-domain LC-current model in the αβ-frame with computational delay, d) z-domain LC-current model in the dq-frame with computational delay.

(Figure 5.2.b). This method is also referred to as double-sampling. For both cases – single- and double-sampling – this implementation of updating and sampling results in a unit delay for the manipulated input.

5.1.1. Delay Model

The publications [19, 23–25, 45] state that the unit delay in the αβ-reference frame can be transferred into the dq-frame via: $z^{-1}|^{\alpha\beta} \rightarrow \mathrm{e}^{-\mathrm{j}\omega T_\mathrm{S}} \cdot z^{-1}|^{\mathrm{dq}}$. In consequence, the delay introduces a phase-shift by $\Delta\theta = -\omega T_\mathrm{S}$ in the dq-frame and the delay itself. Since the reference frame frequency ω is considered a constant (dynamically much slower than inverter current), the compensation of this phase shift is very straightforward, as shown in Figure 5.2.d. However, the delay itself denies proper access to the manipulated input and thus compromises the decoupling techniques demonstrated in chapter 4.

5.1.2. Control and Observer

This work published the implementation of discrete Luenberger-style observers for future state information in [23–25]. Similar to the observer of the capacitor-voltage model in chapter 4, Figure 5.3 shows the structure of the inverter-current observer. The capacitor voltage model still estimates the grid-current, which is passed to the inverter-current observer. These two observers provide future state information for the capacitor voltage, the inverter current, and present state information of the grid current and the capacitor current (capacitor current is calculated from inverter and grid current – see Figure 5.4).

As described in chapter 3.1.2, disturbance input decoupling and decoupling state feedback are vastly different regarding the sensitivity of parameters, timing, and, most importantly, signal accuracy. Therefore, the estimated future state information cannot be used for disturbance input decoupling.

The measured capacitor voltage and the first instance of grid-current estimation yield the best results for the disturbance input decoupling techniques. This behavior is to be expected since disturbance input decoupling is very sensitive to sudden changes, and the disturbances themselves are commonly no energy states or simply dynamically much faster than the system states. The decoupling state feedback techniques, on the other side, benefit a lot from future state estimations.

As described previously, the active damping does not achieve proper damping with significant phase errors concerning the resonance. The phase error in deg caused by the delay can be calculated via $360 \cdot f_{\mathrm{Res}} \cdot T_{\mathrm{s}}$. In most cases, this phase error will exceed any tolerance for effective active damping (in this case, 84 °). Therefore, the proposed active damping approach can only yield proper damping with delay compensation. The publication [24], which was derived from this work, shows that additional future state observers can be implemented, as shown in Figure 5.3 (in full detail and execution order in Figure 5.5). These observers are based on the future state information of the previous observer and the future reference voltage, which are all obtainable, as shown in Figure 5.4.

Since the grid current is just an estimated disturbance and not an observed state, the observer's estimate lags depending on the observer's controller bandwidth which was shown and published in connection to this work in [24]. That publication [24] further shows that the dead-beat implementation ensures that the current information lags by one sample step. Therefore, three stages of the cascaded observer structure (for $k + 2$ estimations) must be

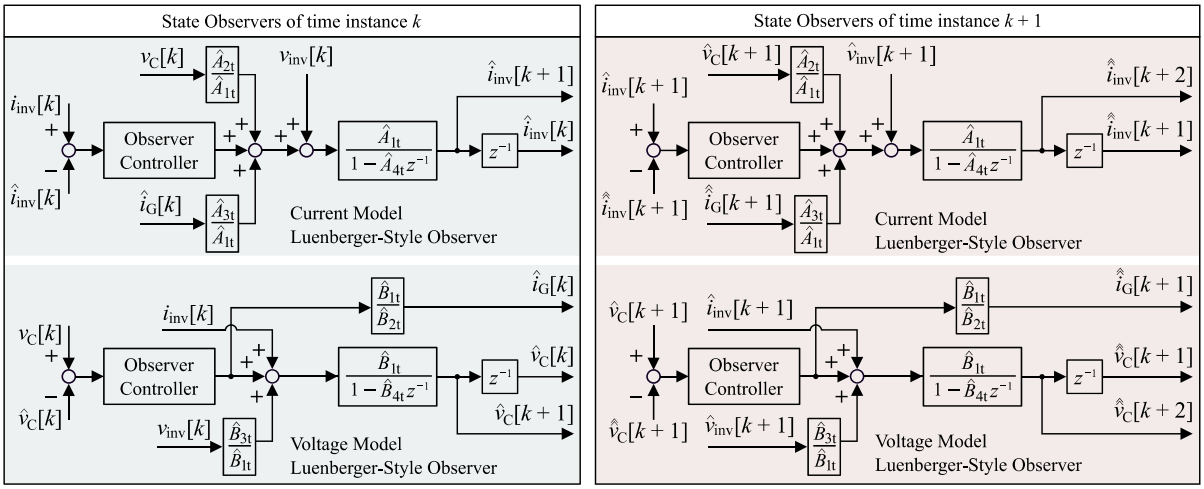

Figure 5.3: Discrete Luenberger-style observer structure for future state estimation using the current and voltage model of the LC-plant. Dynamic analysis (for tuning see Figure 4.10). The cascadedd structure is shown in Figure 5.4 within the overall control structure. Further the detailed cascaded observer structure including the execution order is shown in Figure 5.5.

implemented to establish a proper phase of the estimated grid-current, as shown in Figure 5.4.

The general concept of the observers is based on the fact that the mathematical model can bypass the computational delay. Therefore, the control system and observers have the information on both $v_{\mathrm{inv}}[k+1]$ and $v_{\mathrm{inv}}[k]$ for feed-forward. $v_{\mathrm{inv}}[k]$ is used for the k-sample observer stage with the measurements $i_{\mathrm{inv}}[k]$ and $v_{\mathrm{C}}[k]$. The following sampling stages use

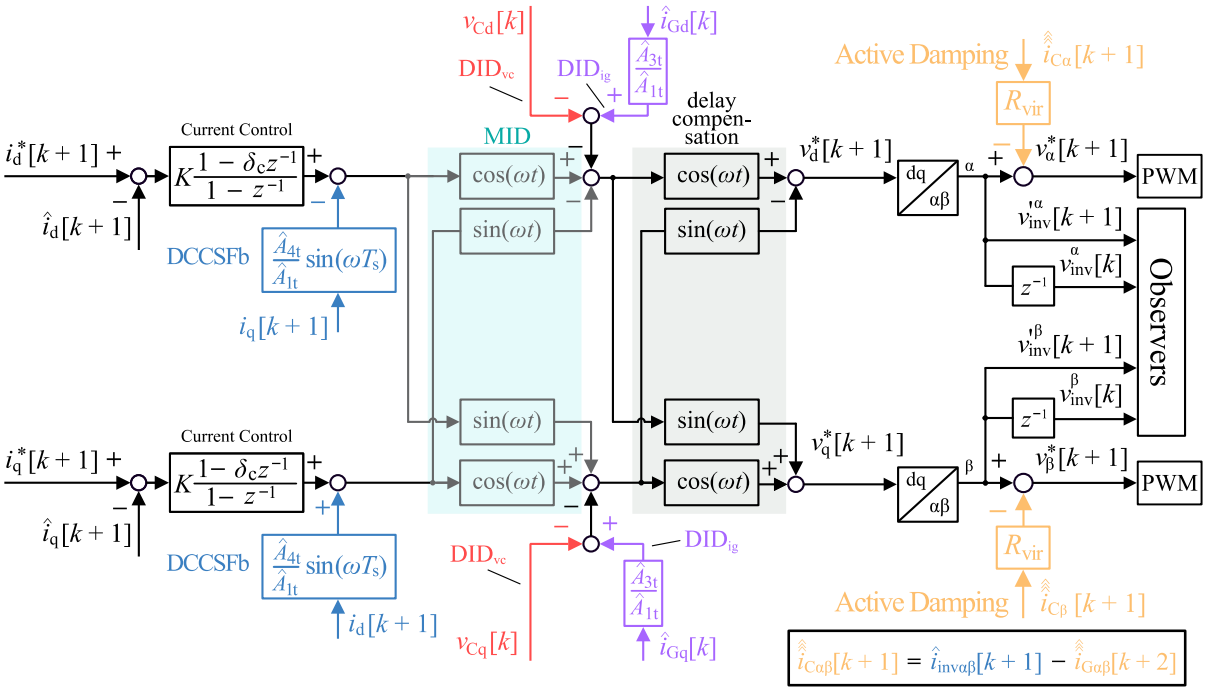

Figure 5.4: Block diagram of the current control structure with delay compensation via a cascaded Luenberger-style observer structure with active damping implementation and decoupling techniques: DCCSFb – Decoupling Cross-Coupling State Feedback, DID – Disturbance Input Decoupling (index: vc – capacitor voltage, ig – grid-current). A shorter version in complex format is displayed in the appendix in Figure 9.5. Further the detailed cascaded observer structure including the execution order is shown in Figure 5.5.

future estimated and observed states from the previous stages (for instance: $[k+1]$-stage uses $\hat{i}_{\mathrm{inv}}[k+1]$ and $\hat{v}_{\mathrm{C}}[k+1]$ from the $[k]$-stage – Figure 5.3 and Figure 5.5). However, the $[k+2]$-stage misses a proper feed-forward – $v_{\mathrm{inv}}[k+2]$. $v_{\mathrm{inv}}[k+2]$ could be approximated by utilizing future state information on a separate future-state controller. However, using a rotated version of $v_{\mathrm{inv}}[k+1]$ as an approximation did yield robust and well-behaved dynamics already ($v_{\mathrm{inv}}[k+2] = v_{\mathrm{inv}}[k+1] \cdot \mathrm{e}^{\mathrm{j}\omega T}$– see Figure 5.3 and Figure 5.5).

To create the final structure, however, the implementation of the active damping has to be included in the feed-forwards. Since the k-sample state is stored from the previous cycle, the active damping portion is already included.

The $[k+1]$-stage and $[k+2]$-stage, on the other hand, need a damping signal at the feed-forward before the $i_{\mathrm{G}}[k+1]$ and $i_{\mathrm{G}}[k+2]$ estimation are derived. Thus, approximations of these damping portions had to be found. Instead, for the $[k+1]$-stage and $[k+2]$-stage, the estimates of $i_{\mathrm{G}}[k]$ and $i_{\mathrm{G}}[k+1]$ are used, respectively.

Figure 5.5 shows the detailed block structure of the cascaded discrete Luenberger-style observer. The red numbers indicate the execution order of the main calculations. Each calculation has to be reliant on signals with lower execution numbers.

Example:

1. Execution block 4 relies on $v_{\mathrm{inv}}[k]$ and $v_{\mathrm{C}}[k]$ with execution order 0, estimated $i_{\mathrm{G}}[k]$, which was derived in execution block 1 and execution block 3. Thus, the estimated $i_{\mathrm{G}}[k]$ has to be multiplied with $A_{3\mathrm{t}}/A_{1\mathrm{t}}$ (estimated) before execution order 4.
2. The calculation for $i_{\mathrm{C}}[k+1]$ needs estimated $i_{\mathrm{inv}}[k+1]$ from execution block 4 and estimated $i_{\mathrm{G}}[k+2]$ from execution block 9 and thus has to be performed any time after 9.

For more detail, a flowchart of the overall current control algorithms with observer implementation is shown in Figure 6.11.

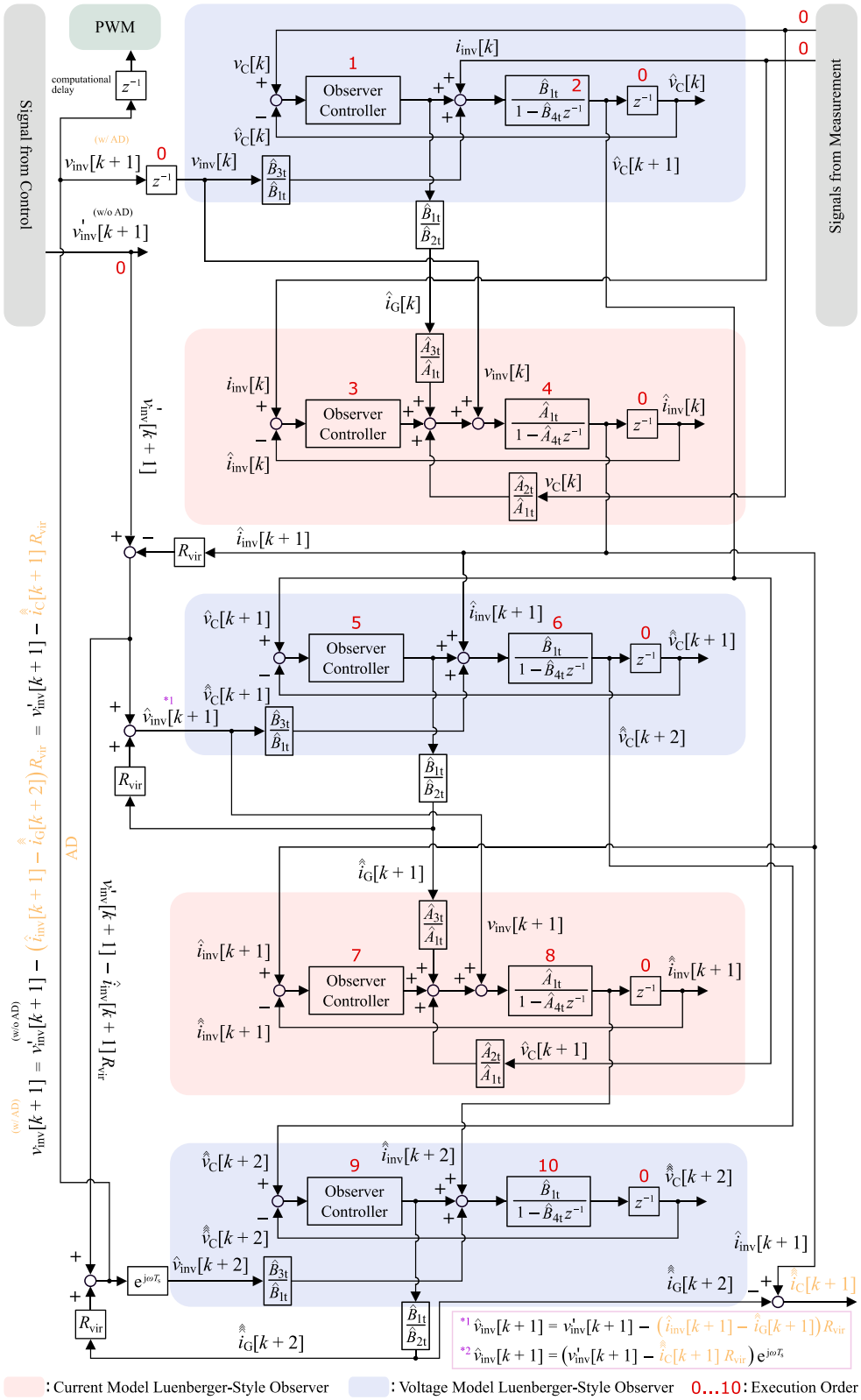

Figure 5.5: Cascaded discrete Luenberger-style observer-structure in full detail with execution order for main csalculations. Execution 0 indicates that this value is present at the start of the calculation sequence.

Figure 5.6 shows the resulting frequency response estimation plots for varying parameter estimation errors up to 30 % with the current control structure of Figure 5.4 using active damping, disturbance input decoupling, decoupling cross-coupling state feedback based on current, and future state information estimated from the proposed cascaded discrete Luenberger-style observer structure.

The proposed delay compensation structure (Figure 5.4) achieves a very robust and well-damped system. However, the results shown in Figure 5.6 are still based on the perfect zero-order-hold discrete voltage assumption. The following subchapter introduces the PWM-based inverter as a voltage source.

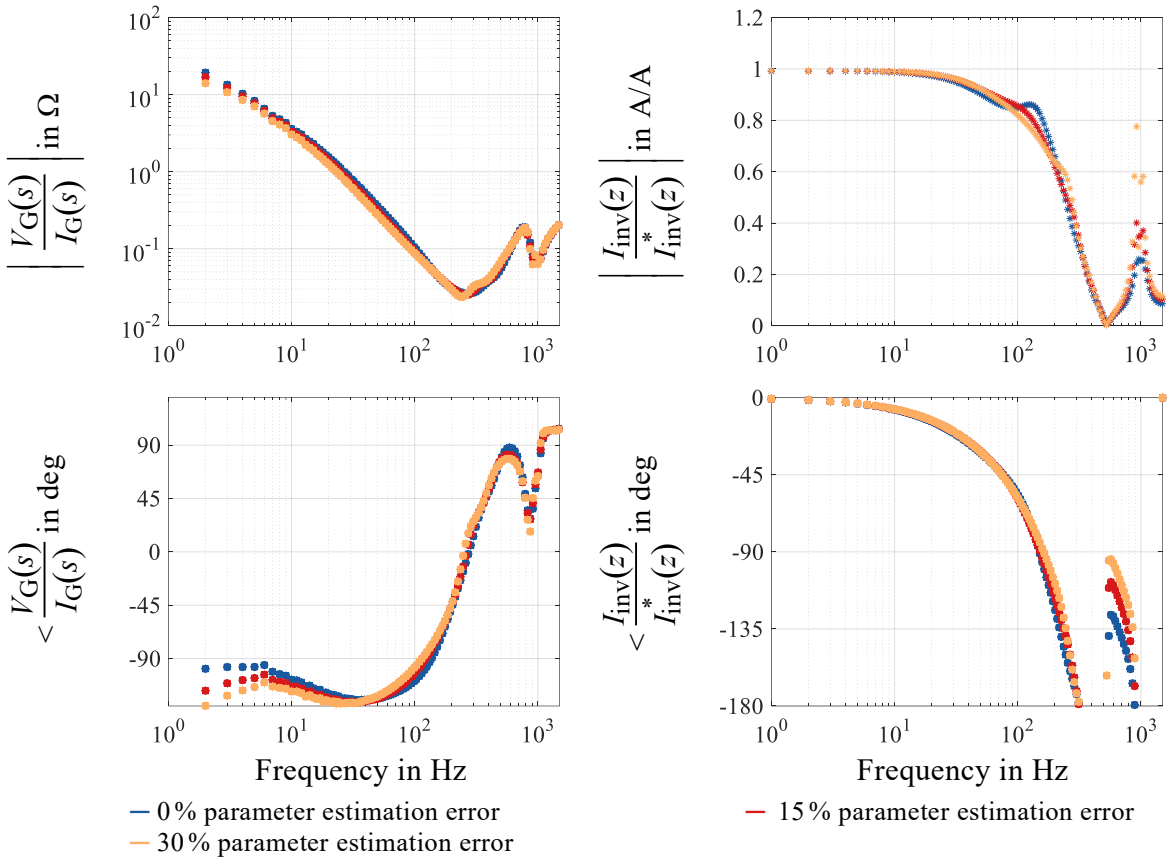

Figure 5.6: Dynamic analysis for different parameter estimation errors of the discrete current controller for the LC-topology (w/ computational delay, 3 kHz sampling) with active damping (R_{vir} = 30 mΩ) using a deadbeat-based cascaded discrete Luenberger-style observer structure (see Figure 5.3 and Figure 5.4) for estimation of present and future state information for the grid-current, inverter current, and capacitor voltage. *Left*: dynamic stiffness, *Right*: command tracking.

5.2. PWM-based Voltage Source

In this subchapter, the PWM-based inverter replaces the zero-order-hold discrete voltage source assumption in the simulation.

5.2.1. Sampling Issues

150 Hz in dq

The publication [46] describes comprehensively the errors caused in current sampling due to the PWM. The PWM is not an ideal discrete voltage source. The PWM matches the intended voltage on average but contains components that deviate from it. Consequently, the sampled current contains response of the ideal voltage and artifacts from the PWM. The paper describes these error components and shows that mainly the fundamental, the -2^{nd}, and the 4^{th} harmonics are affected. This paper further shows that this effect is almost entirely mitigated for double-sampling, as the described components of the -2^{nd} and the 4^{th} harmonics cancel out with that sampling scheme.

The -2^{nd} and 4^{th} harmonics in the dq-reference frame both result in superimposed 150 Hz signals.

Figure 5.7 (left) shows the step response of the proposed control structure with and without the PWM implementation. The 150 Hz component caused by the PWM is very prominent.

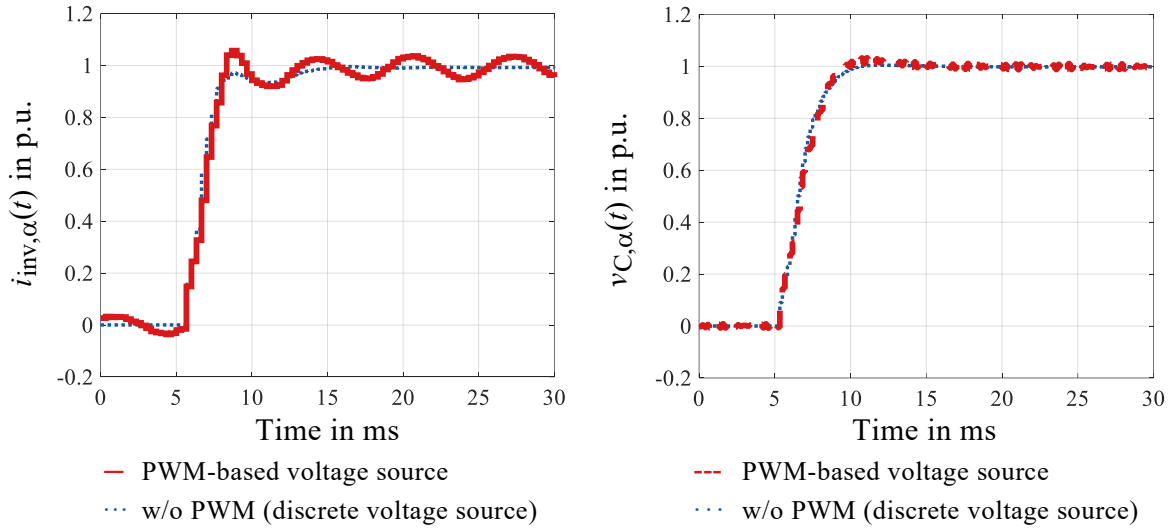

Figure 5.7: Step response comparison of the controlled LC-plant with the proposed current control scheme (Figure 5.4) with PWM-based voltage source representation vs the zero-order-hold discrete voltage source model. *Left*: single-sampling (f_{sw} = 3 kHz, f_s = 3 kHz), *Right*: double-sampling (f_{sw} = 3 kHz, f_s = 6 kHz).

The paper [46] also suggests that double-sampling can mitigate this problem. This suggestion seems very promising as faster sampling in most cases improves control dynamics, and all delays and phase shifts in the signals become smaller. Figure 5.7 (right) illustrates the same comparison in step response with and without PWM in the case of double-sampling ($f_{sw} = 3\,\text{kHz}$, $f_s = 6\,\text{kHz}$). The double-sampling eliminates the 150 Hz distortion almost entirely.

Phase and Magnitude of PWM

The paper [97] describes the discrepancy between the zero-order hold approximation and the PWM. The differences are pronounced in the spectrum (see Figure 5.8). Further, the closer the reference signal approaches the Nyquist frequency $f_s/2$, the stronger the PWM

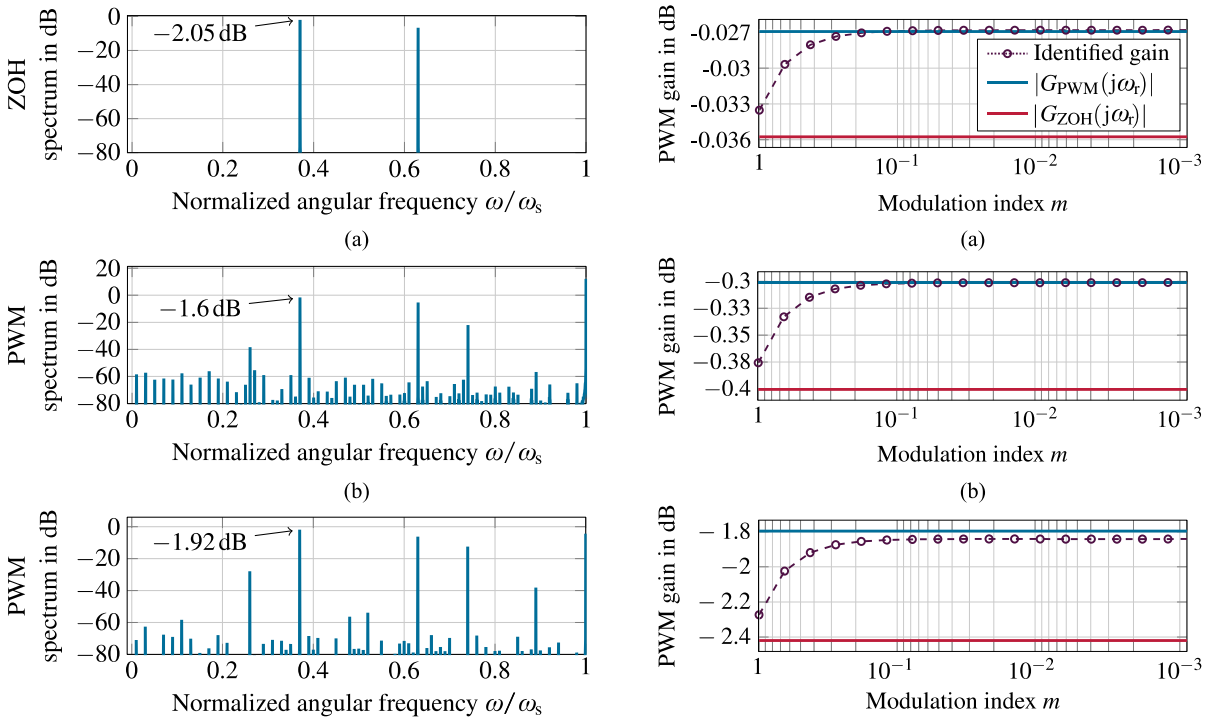

ω_s – sample frequency in rad/s, ω_r – signal frequency in rad/s, ω – frequency (FFT) in rad/s

Figure 5.8: Normalized amplitiude spectrum for a sinusoidal reference input signal with frequency $\omega_r = 0.37\ \omega_s$ for: (a) the ZOH element, (b) PWM with modulation index $m = 0.3$, and (c) PWM with $m = 1$. Image from [32] (p.1518).

Figure 5.9: Plot of modulation gain over modulation for: Dashed violet – the actual identified nonlinear modulator gain, solid blue – the linear magnitude of the proposed PWM model of [32], and solid red – ZOH representation for a sinusoidal reference input with (a) $\omega_r = \omega_s/20$, (b) $\omega_r = \omega_s/6$, and (c) $\omega_r = 0.4\ \omega_s$. Image from [32] (p.1518).

sidebands affect the fundamental. This distortion leads to increased phase and magnitude errors at higher frequencies – compare (a) to (b) to (c) in Figure 5.9 (the error changes from appr. 0.4 % at $\omega_s/20$ to 4 % at $\omega_s/6$ to 22 % at 0.4 ω_s). Furthermore, this discrepancy depends on the modulation index (Figure 5.9 – higher modulation index results in higher modulation error) and the plants' time constants [97].

The publication [97] describes this effect only for first-order systems like an inductive machine or L-filter based converter. Nonetheless, the findings still apply to the LC-filter, but the order of impact remains a subject of further investigation.

The Sampling of Capacitive Signals

As mentioned before (chapter 5.1), sampling at the PWM-extrema works well for inductive signals of voltage source inverters such as the inverter current for L- or LC-filters (see Figure 5.1–right in the Appendix chapter). However, this sampling strategy is very problematic for capacitive signals. Sampling the voltage at the capacitor at the PWM-extrema leads to substantial measurement errors. Figure 5.10 (left) shows that this sampling technique does not sample the average but one of the extrema of the resulting voltage ripple in the case of single-sampling. On the other hand, Figure 5.10 (right) illustrates that double-sampling yields an alternating measurement between the extrema of the voltage ripple. This sampling problem becomes even more severe for voltage measurements at first-order *L*-filters, as the voltage is not an actual energy state in such circumstances.

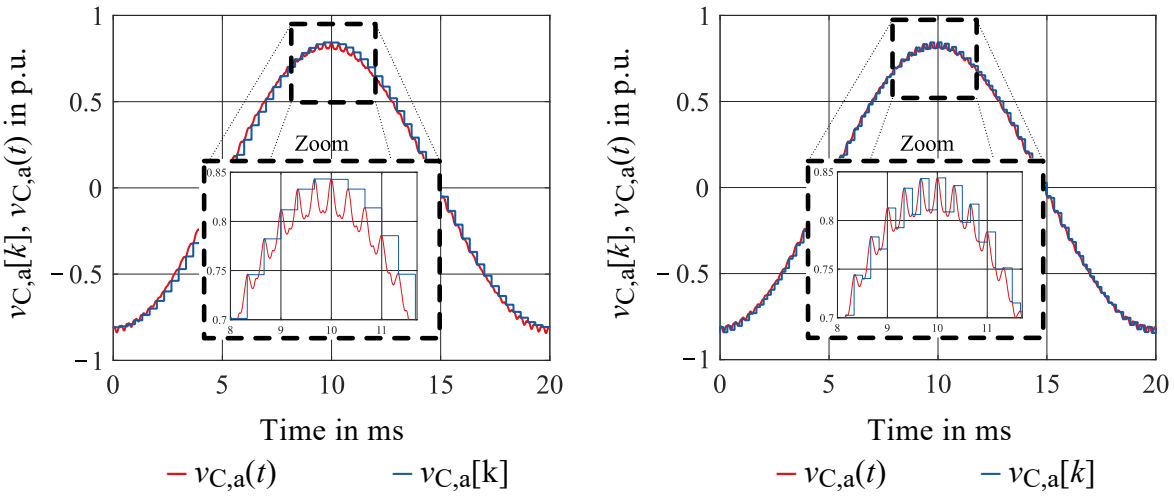

Figure 5.10: Comparison of sampled capacitor voltage (line-neutral) with the actual continuous raw signals with single-sampling on the *left* and double-sampling on the *right*. The sampling takes place at the extrema of the PWM leading to conceptual sampling errors.

This issue can be mitigated by measuring in between the extrema. The downside of that sampling technique is a considerable reduction of available computation time (cut in half) and a slight change in the system′s dynamics. This sampling issue was noted in this work, but no correction was implemented. The consequent oscillations at switching frequency for double-sampling were very apparent on the manipulated inputs and sampled currents. Further, the measurements do not represent the average model behavior and thus can cause estimation inaccuracies of the observers. In simulations, the described improved sampling strategy did solve the related issues. The improved sampling strategy is not part of this work to be consistent between simulations and measurements.

Figure 5.11 and Figure 5.12 show the frequency response function plots for different parameter estimation errors up until 30 % for single-sampling and double-sampling,

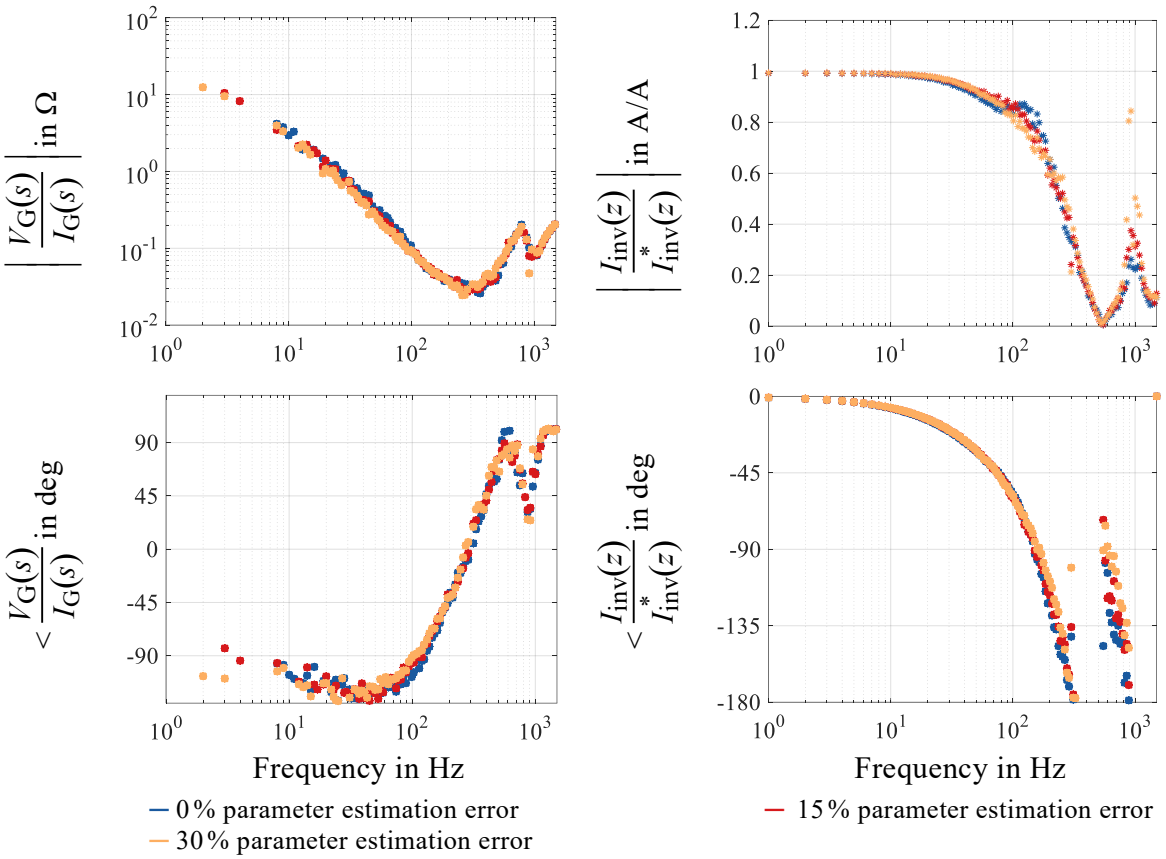

Figure 5.11: Dynamic analysis for different parameter estimation errors of the discrete current controller for the LC-topology (w/ computational delay and 3 kHz PWM and 3 kHz single-sampling implementation) with active damping (R_{vir} = 30 mΩ) using a deadbeat-based cascaded discrete Luenberger-style observer structure (see Figure 5.3 and Figure 5.4) for estimation of present and future state information for the grid-current, inverter current, and capacitor voltage. *Left*: dynamic stiffness (impedance), *Right*: command tracking.

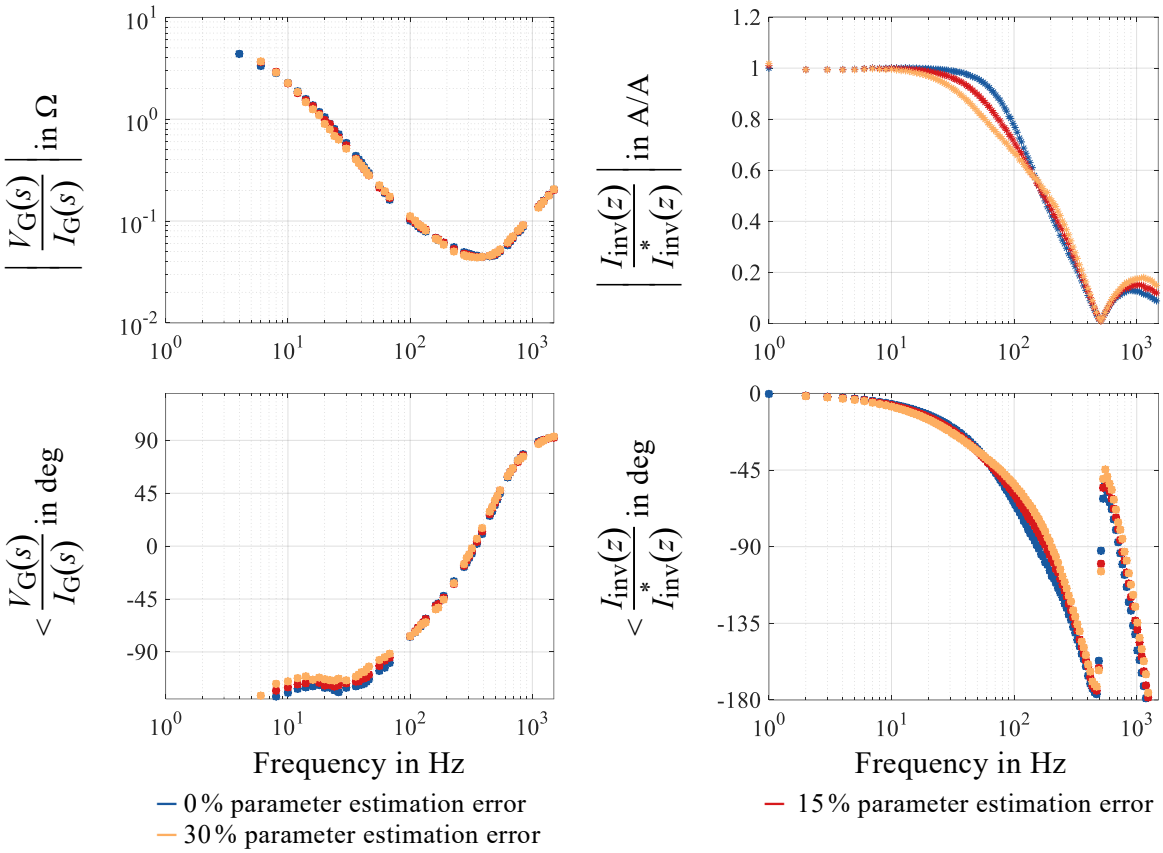

Figure 5.12: Dynamic analysis for different parameter estimation of the discrete current controller for the LC-topology (w/ computational delay and 3 kHz PWM and 6 kHz double-sampling implementation) with active damping (R_{vir} = 30 mΩ) using a deadbeat-based cascaded discrete Luenberger-style observer structure (see Figure 5.3 and Figure 5.4) for estimation of present and future state information for the grid-current, inverter current, and capacitor voltage. *Left*: dynamic stiffness (impedance), *Right*: command tracking.

respectively. The dynamic attributes for both cases of sampling yield very similar results to the previous baselines of the continuous and discrete designs.

The computational delay does lead to a drop in phase and magnitude of the harmonic impedance close to the Nyquist Frequency. This drop, however, is still well-damped in all of the displayed cases of estimation error.

The main advantages of double-sampling are achieved due to the higher sampling frequency. Doubling the switching frequency would yield similar harmonic impedance plots but at the cost of higher switching losses. Further, as shown earlier [46], major harmonic (-2^{nd} and 4^{th}) issues are solved by this sampling technique, as well.

5.3. Implementation Space Conclusion

This chapter focused on implementing and compensating for the computational delay that is inevitable for DSP- and PWM-based inverters.

The compensation is based on a cascaded Luenberger-style observer structure that estimates future states. The future state information is used for decoupling techniques and active damping. However, the disturbance input decoupling uses the current state information from measurements, which is critical, as described in chapters 3.1.2 and 5.1.2.

Further, this chapter showed the influence of the PWM regarding the distortion of the -2^{nd} and 4^{th} harmonic. Double-sampling improves the distortion problem. In general, double-sampling yields a more robust and damped control system.

The final control structure with active damping and delay compensation shows very damped and robust system attributes for single- and double-sampling (see Figure 5.13).

The next chapter describes the experimental setup, which includes the down-scaling of the original plant to a 25 V-based laboratory test bench.

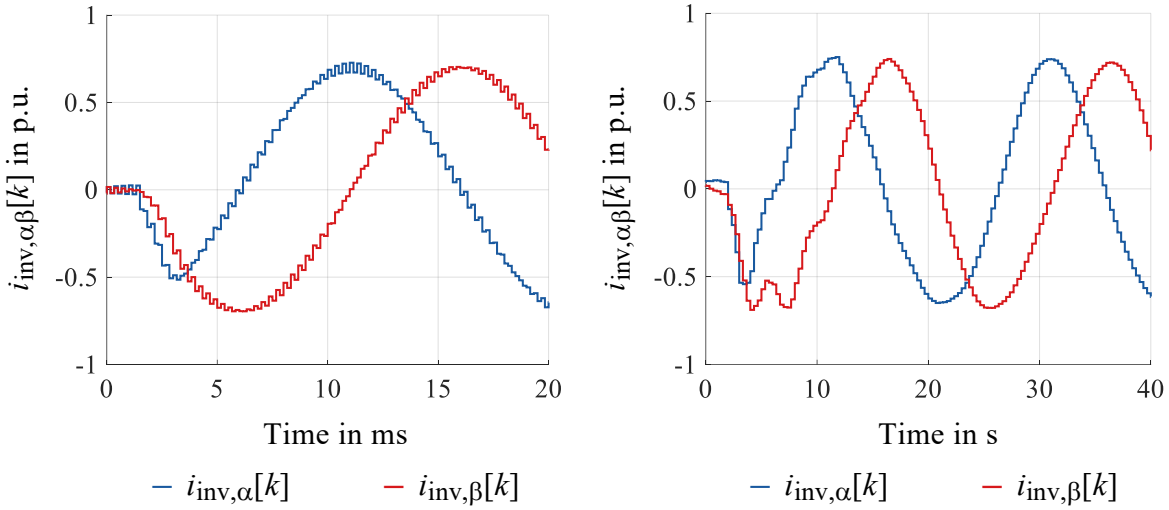

Figure 5.13: Time domain plot of the αβ inverter currents after command step at t = 1 ms with the proposed current control scheme for double-sampling on the *left* and single-sampling on the *right*.

6. Experimental Setup

This chapter outlines the design and approximation methods of the experimental low-voltage test bench. The design process entails the scaling process of the passive components, semiconductors (switching and conduction attributes), and the dead and delay times. Further, this chapter describes the measurement and evaluation methods in detail.

The final design is depicted in Figure 6.1 − Figure 6.3, and Figure 9.7 and Figure 9.8 in the appendix.

6.1. Design

For the laboratory setup at the University of Rostock, the original wind turbine converter parameters had to be scaled down in power to fit the laboratory grid. Most electrical components are not scale-invariant regarding physical size and power dimensions. The design step has to quantify consequent discrepancies, and in many cases, a viable alternative has to be found.

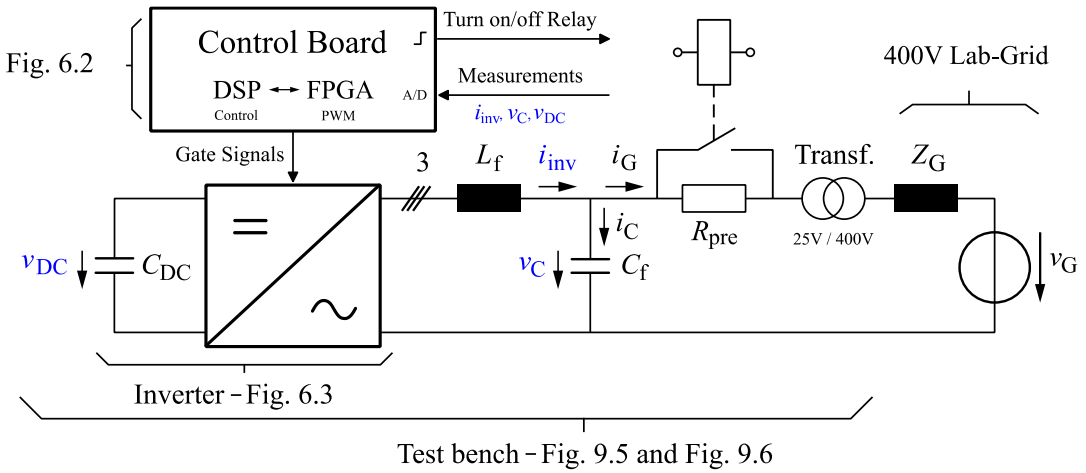

Figure 6.1: Diagram of the laboratory scaled 25 V low-power test bench. The control board is based on a DSP/FPGA combination controlling the gate signals of the inverter and setting up the startup via relays.

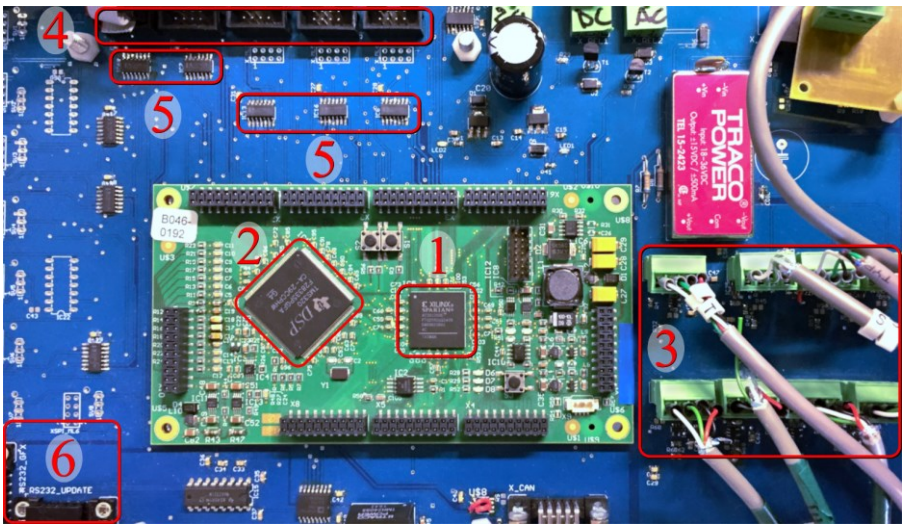

1 – FPGA Xilinx Spartan

2 – DSP TMS320

3 – Sensor inputs (OP-amps)

4 – PWM-output signals

5 – Line driver

6 – RS232: programming & reading

Figure 6.2: Photographs of the control board of the 25 V test bench – DSP/FPGA combination and peripherals.

The predominant semiconductor at the 690 V (1.1 kV DC-link) level of wind turbine converters is the IGBT. However, the IGBT is a bipolar device. It is not suitable for the 25 V level of the test bench due to a poor relationship between conduction and switching loss attributes for these power levels.

A proper replacement at this voltage level is the MOSFET. However, since MOSFETs are unipolar, these devices are very different regarding conduction and switching characteristics than the IGBT. Therefore, adaptations have to be employed to find an appropriate representation of the IGBT. Similar issues are present for the passive components. The

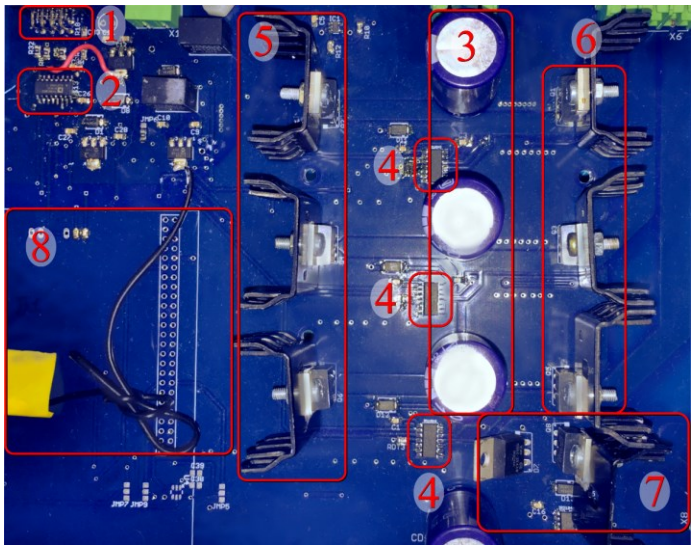

1 – PWM-input signals (from FPGA)

2 – Isolation chips

3 – DC-link

4 – Half-bridge drivers

5 – Low-side phase switches

6 – High-side phase switches

7 – Chopper

8 – Placeholder for alternative microcontroller

Figure 6.3: Photographs of the inverter board of the 25V laboratory test bench – phase switches, drivers, and peripherals.

methods for scaling and adaptations are shown in the following for the different components.

6.1.1. Voltage, Current, and Power-Scaling

This subchapter displays the derivation of the scaling factors for voltage n_u and current n_i and the consequent change in design parameters. In the following, the indexes m and n indicate the test bench parameters and the nominal values of the given setup, respectively (without index m implies the original full-scale power plant).

$$n_i = \frac{I_n}{I_{n\text{-}m}}, \quad n_u = \frac{V_n}{V_{n\text{-}m}} \tag{6.1}$$

This work defines five scaling criteria for the test bench in comparison to the original model:

1. Equal relative (short-circuit) inductive voltage drop u_k: $u_k = u_{k\text{-}m}$
2. Equal relative (no-load) capacitive current i_0: $i_0 = i_{0\text{-}m}$
3. Equal ratio of stored energy and power: $\frac{E_C}{E_{C\text{-}m}} = \frac{P}{P_m}$
4. Equal time constants
5. Equal resonant frequency

Criteria 1 and 2 lead to (6.2) and (6.3), which illustrate the proper scaling of the test bench parameters. Finally, (6.4) – (6.6) show that (6.2) and (6.3) also meet the criteria 3 to 5, respectively.

$$u_k = \frac{\omega L I_n}{V_n} \qquad u_{k\text{-}m} = \frac{\omega L_m I_{n\text{-}m}}{V_{n\text{-}m}}$$

$$u_k = u_{k\text{-}m} = \frac{\omega L I_n}{V_n} = \frac{\omega L_m I_{n\text{-}m}}{U_{n\text{-}m}}$$

$$\boxed{L = L_m \frac{n_u}{n_i} \quad R = R_m \frac{n_u}{n_i}} \tag{6.2}$$

$$i_0 = \frac{\omega C V_n}{I_n} \text{ and } i_{0\text{-}m} = \frac{\omega C_m V_{n\text{-}m}}{I_{n\text{-}m}}$$

$$i_0 = i_{0\text{-}m} = \frac{\omega C V_n}{I_n} = \frac{\omega C_m V_{n\text{-}m}}{I_{n\text{-}m}}$$

$$\boxed{C = C_m \frac{n_i}{n_u}} \tag{6.3}$$

$$\frac{E_\mathrm{C}}{E_\mathrm{C\text{-}m}} = \frac{\frac{1}{2}C_\mathrm{m}{V_\mathrm{n\text{-}m}}^2}{\frac{1}{2}C{V_\mathrm{n}}^2} = \frac{V_\mathrm{n\text{-}m}I_\mathrm{n\text{-}m}}{V_\mathrm{n}I_\mathrm{n}} = \frac{P}{P_\mathrm{m}}$$

$$\frac{n_\mathrm{u}}{n_\mathrm{i}}\left(\frac{1}{n_\mathrm{u}}\right)^2 = \frac{1}{n_\mathrm{i}}\frac{1}{n_\mathrm{u}} \quad \checkmark \tag{6.4}$$

$$\tau_\mathrm{LC\text{-}m} = \sqrt{L_\mathrm{m}C_\mathrm{m}} = \sqrt{L\frac{n_\mathrm{i}}{n_\mathrm{u}}C\frac{n_\mathrm{u}}{n_\mathrm{i}}} = \sqrt{LC} = \tau_\mathrm{LC} \quad \checkmark$$

$$\tau_\mathrm{RL\text{-}m} = \frac{L_\mathrm{m}}{R_\mathrm{m}} = \frac{L}{R}\frac{n_\mathrm{i}}{n_\mathrm{u}}\frac{n_\mathrm{u}}{n_\mathrm{i}} = \frac{L}{R} = \tau_\mathrm{RL} \quad \checkmark \tag{6.5}$$

$$f_\mathrm{R\text{-}LCL\text{-}m} = \frac{1}{2\pi}\sqrt{\frac{L_\mathrm{1m}+L_\mathrm{2m}}{L_\mathrm{1m}L_\mathrm{2m}C_\mathrm{m}}} = \frac{1}{2\pi}\sqrt{\frac{\frac{n_\mathrm{i}}{n_\mathrm{u}}(L_1+L_2)}{\left(\frac{n_\mathrm{i}}{n_\mathrm{u}}\right)^2\cdot\frac{n_\mathrm{u}}{n_\mathrm{i}}L_\mathrm{1m}L_\mathrm{2m}C_\mathrm{m}}}$$

$$= \frac{1}{2\pi}\sqrt{\frac{L_1+L_2}{L_1L_2\,C}} = f_\mathrm{R\text{-}LCL} \quad \checkmark \tag{6.6}$$

6.1.2. Semiconductor Scaling

Conduction Behavior

As described previously, the MOSFET is the preferred semiconductor for the 25 V test bench for this work. The unipolar MOSFET features conduction losses similar to a resistor R_DS. In contrast, the bipolar IGBT shows conduction losses that depend on the load current, as shown in Figure 6.4.

The on-state resistance is part of the design attributes of the MOSFET and is consequently chosen to represent the IGBT at a meaningful operating point. In this work, the R_DS of the MOSFET was selected to match the relative voltage drop V_CE at the nominal current (RMS-value) and nominal operating temperature, as shown in (6.7) and Figure 6.4.

$$V_\mathrm{CE}(I=I_\mathrm{N}) = V_\mathrm{DS\text{-}m}(I=I_\mathrm{N\text{-}m})\cdot n_\mathrm{u}$$

$$R_\mathrm{DS} = \frac{V_\mathrm{DS\text{-}m}(I=I_\mathrm{N\text{-}m})}{I_\mathrm{N\text{-}m}} \tag{6.7}$$

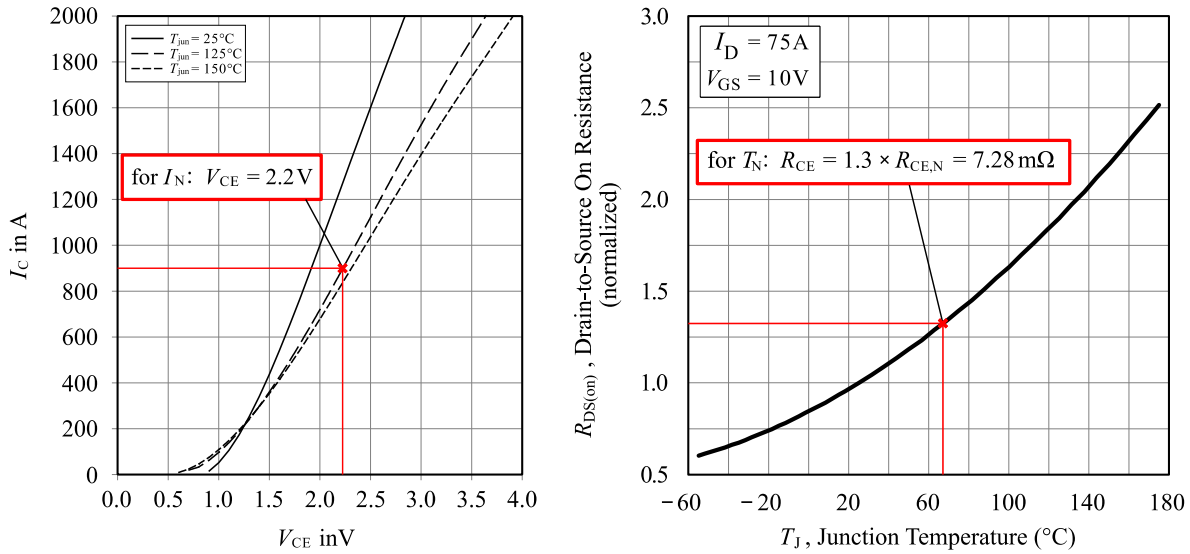

Figure 6.4: Datasheet characteristics of the original IGBT and the model MOSFET. *Left*: Forward-Voltage drop of the IGBT FF1000R17IE4P, *Right*: on-state resistance of the MOSFET IRFS4310PbF.

The temperature of the MOSFET highly depends on the operating point and the cooling system. The operating point can vary dramatically in the wind turbine example. The nominal case is chosen for the design in this project. It should be noted that the reverse conducting bipolar body-diode of the MOSFET has much higher on-state losses (appr. ten times) than the unipolar MOSFET. This body-diode, however, only conducts during the approximately $1 - 3\,\mu s$ dead time of the half-bridge switching. This discrepancy leads to a conduction loss error of roughly 9 % (10 times as much loss during ~ 1% of the time). This effect could be mitigated by lowering the dead time.

However, the dead time also results in a voltage-time area error during switching events depending on the current direction (i.e., once per switching period). For example, a $3\,\mu s$ dead time leads to an average voltage error of 11 V in the original setup and 0.4 V on the test bench. Normalized with the grid voltage (phase-phase RMS), this represents a 1.6 % error. The error at each sampling instance, on the other hand, depends on the reference voltage, and the percentage error can go up to infinite at 0 V reference.

Therefore, comparing the two effects of conduction loss error of the body diode and the voltage-time area error is not straightforward. This work, however, assumes the latter is more severe. The main argument for this statement is that a small error in losses for the switches will be negligible compared to the other loss errors caused by the cables,

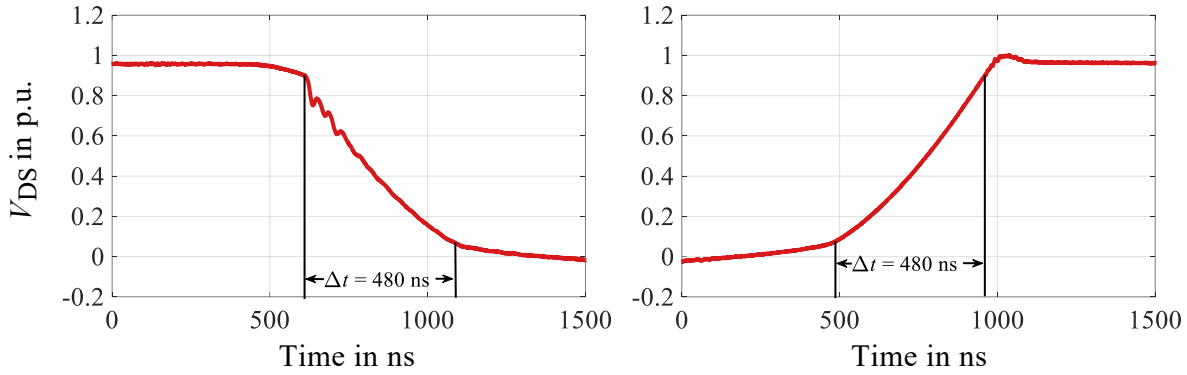

Figure 6.5: Measurements of the voltage flanks of the Drain-Source voltage V_{DS} of the MOSFET IRFS4310PbF with $R_{G,on} = 300\,\Omega$ and $R_{G,off} = 110\,\Omega$. *Left*: turn on appr. 480 ns, *Right*: turn off approx. 480 ns.

transformers, inductors, and all the remaining passive components of a low-voltage system. The manipulated input's 0.4 V average voltage error might impact the control, though. Thus, the same dead time of the original setup was used for the low-voltage test bench.

The temperature estimate used in Figure 6.4 for calculating the on-state resistance can fluctuate in a wide range. Nonetheless, the chosen semiconductor is a good approximation of the nominal operating point of the original converter.

Switching Behavior

In this work, the main criteria for switching behavior representation are the voltage rise and fall time at the MOSFETs (Figure 6.5), and the effective dead time of the half-bridge switching to prevent shoot-throughs (Figure 6.6).

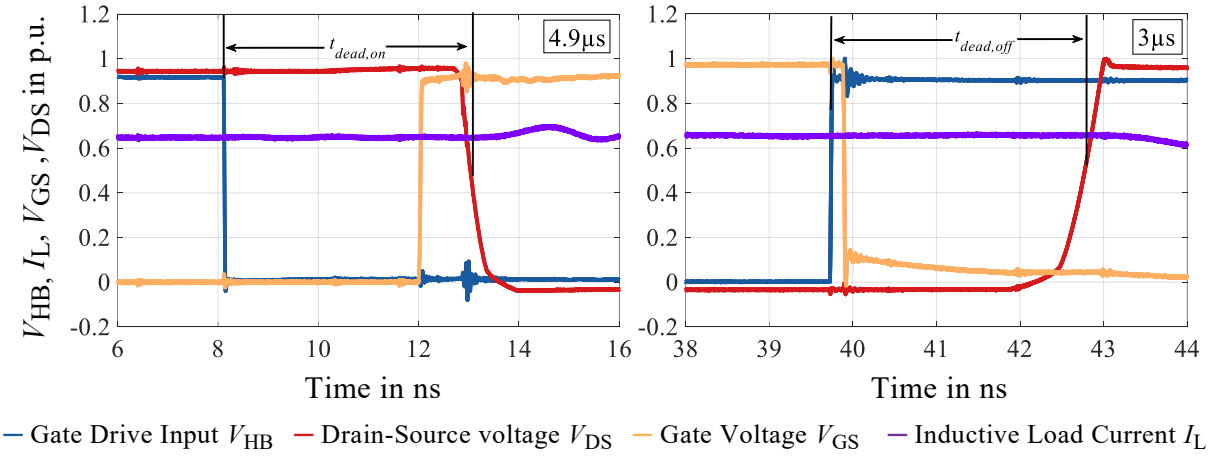

Figure 6.6: Measurements of the switching dead time of the bottom MOSFET IRFS4310PbF and gate driver IR21094SPbF with $R_{DT} = 150\,\text{k}\Omega$. *Left*: turn on, *Right*: turn off, $\Delta t \approx 2\,\mu\text{s}$.

To achieve similar rise times as the original setup during the turn on and turn off, the gate resistances $R_{G,on}$ and $R_{G,off}$ had to be chosen accordingly. This adjustment was held out via measurement and iteration. Figure 6.5 shows the final results using $R_{G,on} = 300\,\Omega$ and $R_{G,off} = 110\,\Omega$ achieving voltage flanks in the 500 ns range, similar to the original IGBT setup.

The gate driver IR21094SPbF is used in this project. The dead time can be varied via an external resistor. Via measurements and iteration, this resistor was set to $150\,k\Omega$ resulting in roughly 2 µs dead time (see Figure 6.6).

6.1.3. Inductive Component Scaling

Subchapter 6.1.1 lays out the intended scaling of the parameters regarding resistance, inductance, and capacitance for all the components. However, the available components cannot always match these desired values. This subchapter describes the challenges of reaching the correct low-voltage scaled model for inductive components.

The publication [98] describes the scaling laws of inductive components (6.8) – (6.10) in a broad sense, where u is the geometric scaling factor (length · u, width · u, height · u), S is the apparent power, m is the mass of the component, and P_{loss} denotes the power loss. The described derivations generally show that inductive components scale well into higher power applications. With higher power, the relative mass in kg / kVA and the relative losses in kW / kVA go down.

Inversely, the relative mass and losses go up when scaling into lower power. (6.8) – (6.10), however, are only accurate if B and J are kept constant (B – magnetic flux density magnitude, J – current density magnitude), which would be the case for most industrial applications as B and J are usually designed close to the maximum of the involved components to achieve high monetary efficiency.

$$S = S_m \cdot u^4 \tag{6.8}$$

$$m = m_m \cdot u^3 \tag{6.9}$$

$$P_{loss} = P_{loss,m} \cdot u^3 \tag{6.10}$$

To find a proper-scaled inductor, the resistance and inductivity values of the equivalent circuit should approximately obey the scaling formulae (6.2). The copper and iron losses dominate the resistive behavior that has to be represented.

Copper losses describe the conduction losses within the windings of the inductor. The conduction losses can be further separated into the pure resistive conduction losses ($P_r = I^2 R_{DC}$ – same as skin effect at $f = 0$), and the skin- ($P_s = F_R(f) \cdot I^2 \cdot R_{DC}$) and proximity effect ($P_p = G_R(f) \cdot H^2 \cdot R_{DC}$) [99]. However, for low-frequency applications, the pure resistive conduction losses without frequency dependency are a good representation.

On the other hand, iron losses represent the losses within the core of the inductor. The iron losses can be further separated into hysteresis and eddy current losses ($P_{ed} \propto f^2 \cdot |B|^2$). For powdered core material, the hysteresis losses dominate the iron losses [99]. This assumption is also valid for laminated material for low-frequency applications [99].

The dissertation [99] shows that the hysteresis losses are well represented with the empirical Steinmetz Equation (6.11), where the parameters K, α, β are material parameters, and V_{Fe} is the volume of the core.

$$P_{loss} = V_{Fe} \cdot K \cdot f^{\alpha} \cdot |B|^{\beta} \tag{6.11}$$

It should be noted that this work tries to simplify the loss effects to a first-order approximation. The main task of this chapter is to evaluate the feasibility of proper representation of scaled models and to identify critical limits. Other effects, such as the relaxation effect, are not considered. For a deeper analysis of inductive components and the loss effects, the interested reader should refer to [99].

Equivalent Circuit

A good representation of the iron losses and copper losses as respective resistances has to be found to evaluate the influence and the validity of the scaled representation of the

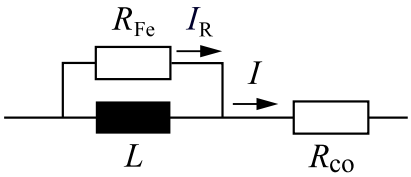

R_{Fe} – iron losses repr. resistance
R_{co} – copper losses repr. resistance
I – current through inductor
I_R – iron loss current

$$P_{Fe} = I_R^2 \cdot R_{Fe} \tag{6.12}$$

$$I_R = I \sqrt{\frac{(\omega L)^2}{(\omega L)^2 + R_{Fe}^2}} \tag{6.13}$$

$$P_{Fe} = I^2 \frac{R_{Fe}(\omega L)^2}{(\omega L)^2 + R_{Fe}^2} \tag{6.14}$$

$$\text{for } f \ll f_n \text{ i.e. } (\omega L)^2 \ll R_{Fe}: \quad P_{Fe} \propto f^2 \;\&\; P_{Fe} \propto I^2 \propto B^2$$

Figure 6.7: First-order equivalent circuit for an inductor including iron and copper losses. The equations are valid for magnitude or RMS values.

inductor. The publication [98] utilizes the typical expression of the iron losses as parallel resistance and the copper losses as series resistance to the inductor (see Figure 6.7).

A parallel R_{Fe} representation for the iron losses − (6.14) − does not match the Steinmetz Equation for every material. However, for $\alpha \approx 2$ and $\beta \approx 2$, the equivalent circuit can be a proper representation within a specific frequency range. For good representation, the losses have to be a function of f^2 and $|B|^2$. The following is valid within the saturation limits of the magnetic material: $B \propto I$ ($B = I \cdot L / A$). Therefore, Figure 6.8 and (6.14) show that the frequency and magnetic flux criteria are met until the natural frequency of the parallel RL model ($\omega_n = R / L$).

Scaling

Figure 6.9 shows a schematic of a toroidal inductor with the physical parameters used in this section. Further, Figure 6.9 illustrates the utilized scaling factors (λ_ρ – conductivity ratio, n_i – current scaling, n_u – voltage scaling, δ_{Fe} – core radius scaling, δ_w – conductor radius scaling, δ_N – number of windings scaling, δ_B – magnetic flux density scaling, δ_x – iron loss scaling to power scaling ratio, δ_{lFe} – core length scaling).

The following section illustrates the scaling in power and the geometry options of a toroidal inductor. Toroidal inductors are not the predominant inductor architecture for high power applications. Further, the analysis is based on simplifications such as $\alpha = 2$ and $\beta = 2$, and assumptions of similar inductor architecture with the same packing density of the windings

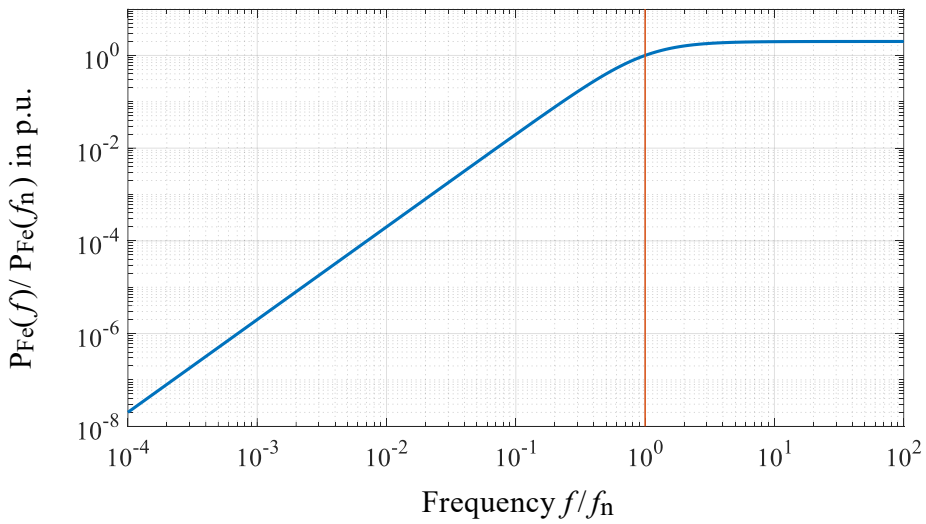

Figure 6.8: Iron losses $P_{Fe}(f)$ over frequency for a parallel resistance representation (see Figure 6.7). Losses are normalized to the losses at the natural frequency f_n. The frequency is normalized to f_n. The losses feature a gradient of 2 decades per decade in the double logarithmic plot, i.e., a quadratic relationship until f_n.

(thus $l_w \propto 2\pi \cdot r_{Fe} \cdot N$, resulting in $l_w/l_{w.m} = \delta_{Fe}\delta_N$). However, this example still serves as a demonstrator for the scaling of inductive components and highlights critical limits. The following shows additional assumptions and the consequent scaling formulae for this example.

The initial premise in this illustration procedure defines the scaling of the copper losses to be equal to the scaling of the apparent power:

$$\frac{P_{co}}{P_{co.m}} = \frac{I^2}{I_m^2}\frac{R_{co}}{R_{co.m}} = \frac{n_i^2}{\delta_\rho}\frac{l_w}{l_{w.m}}\frac{A_{w.m}}{A_w} = \frac{n_i^2}{\delta_\rho}\frac{\delta_{Fe}\delta_N}{\delta_w^2} = \frac{S}{S_m} = n_i \cdot n_u. \tag{6.15}$$

Induction Scaling:

$$\frac{V}{V_m} = \delta_N \frac{\Phi}{\Phi_m} = n_u \tag{6.16}$$

Magnetic flux density scaling:

$$\frac{B}{B_m} = \delta_B = \frac{\Phi}{\Phi_m}\frac{A_{Fe.m}}{A_{Fe}} = \frac{n_u}{\delta_N \delta_{Fe}^2} \tag{6.17}$$

Combining the copper loss scaling assumption (6.15) with the simple induction scaling (6.16), and the magnetic flux density scaling (6.17) yields:

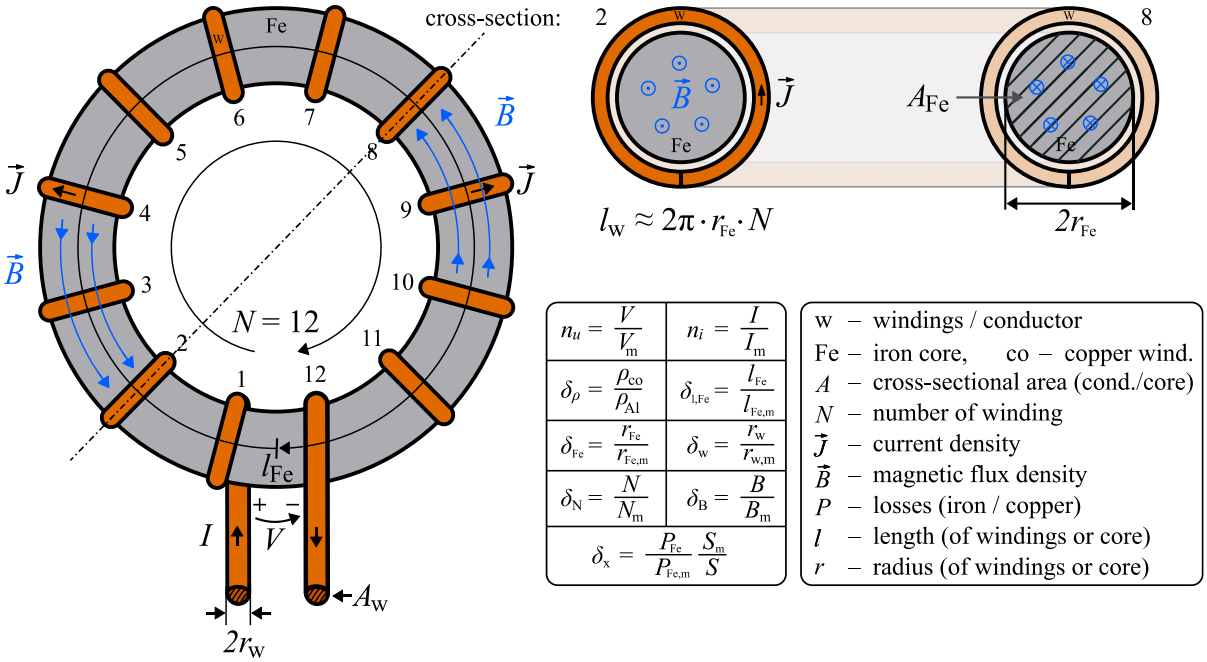

Figure 6.9: Longitudinal section and cross-section of a toroidal inductor. This figure defines the parameters used in section 6.1.3.

$$\boxed{n_\mathrm{i} = \delta_\mathrm{Fe}\delta_\mathrm{w}^2\delta_\rho\delta_\mathrm{B}} \tag{6.18}$$

Assuming the same frequencies (switching and fundamental), similar architecture, and the option of different magnetic flux density, the iron loss scaling can be derived as follows:

$$\frac{P_\mathrm{Fe}}{P_\mathrm{Fe.m}} = \frac{V_\mathrm{Fe}}{V_\mathrm{Fe.m}}\frac{B^2}{B_\mathrm{m}^2} = \frac{V_\mathrm{Fe}}{V_\mathrm{Fe.m}}\delta_\mathrm{B}^2 = \frac{l_\mathrm{Fe}}{l_\mathrm{Fe.m}}\frac{A_\mathrm{Fe}}{A_\mathrm{Fe.m}}\,\delta_\mathrm{B}^2 = \delta_\mathrm{Fe}^2\delta_\mathrm{N}\delta_\mathrm{w} \overset{(6.17)}{=} \delta_\mathrm{B}\delta_\mathrm{w}n_\mathrm{u} \tag{6.19}$$

Further, this example leaves different iron loss scaling options to apparent power scaling (δ_x). This discrepancy was necessary to find proper solutions, as shown in the calculation examples in the appendix subchapter 9.5.

Iron Losses Condition:

$$\frac{P_\mathrm{Fe}}{P_\mathrm{Fe.m}} = \frac{S}{S_\mathrm{m}}\,\delta_\mathrm{x} = \delta_\mathrm{B}\delta_\mathrm{w}n_\mathrm{u} = \delta_\mathrm{x}\cdot n_\mathrm{i}\cdot n_\mathrm{u} \tag{6.20}$$

$$\boxed{n_\mathrm{i} = \delta_\mathrm{w}\delta_\mathrm{B}/\delta_\mathrm{x}} \tag{6.21}$$

Combining the copper loss scaling premises of (6.18) with the iron loss scaling assertion of (6.21) yields (6.22).

$$\boxed{\delta_\mathrm{w}\delta_\mathrm{Fe}\delta_\rho = \delta_\mathrm{x}^{-1}} \tag{6.22}$$

Scaling Calculation Example

With (6.15) − (6.22), possible inductor scaling from a 5 MW wind turbine to a 25 V test bench can be tested. A straightforward solution with perfect iron and copper scaling can be found in (6.15) − (6.22) using the same inductor and by keeping $n_\mathrm{u} = n_\mathrm{i}$.

Using the same inductor of a 5 MW plant for a 25 V test bench is out of the scope of the intended project. Another solution with adequate scaling had to be found. A search algorithm was implemented to see different results for various boundary conditions regarding the physical volume and electrical parameters. The search algorithm aimed to minimize the core volume V_Fe and the iron losses (δ_x) within the defined restrictions. The boundary conditions and results for three examples are shown in the appendix subchapter 9.5. For the given test bench criteria of $n_\mathrm{i} = 450$ and $n_\mathrm{u} = 27$, an optimal solution with a core volume lowered by a factor of 84 but with increased iron losses by a factor of 34 ($\delta_\mathrm{x} = 3\,\%$) was found.

These numbers illustrate the difficulty in scaling for inductive components. The low-voltage test bench components become very resistive in comparison — the scaled example-inductor yields similar or even bigger iron losses than copper losses. In high voltage applications,

the iron losses of inductive components are commonly about an order of magnitude lower than the copper losses.

Figure 6.10 illustrates the influence of higher relative iron losses for the equivalent circuit of Figure 6.7. This figure shows a much stronger damping of the LC resonance in case of iron losses in the same order of magnitude as the copper losses.

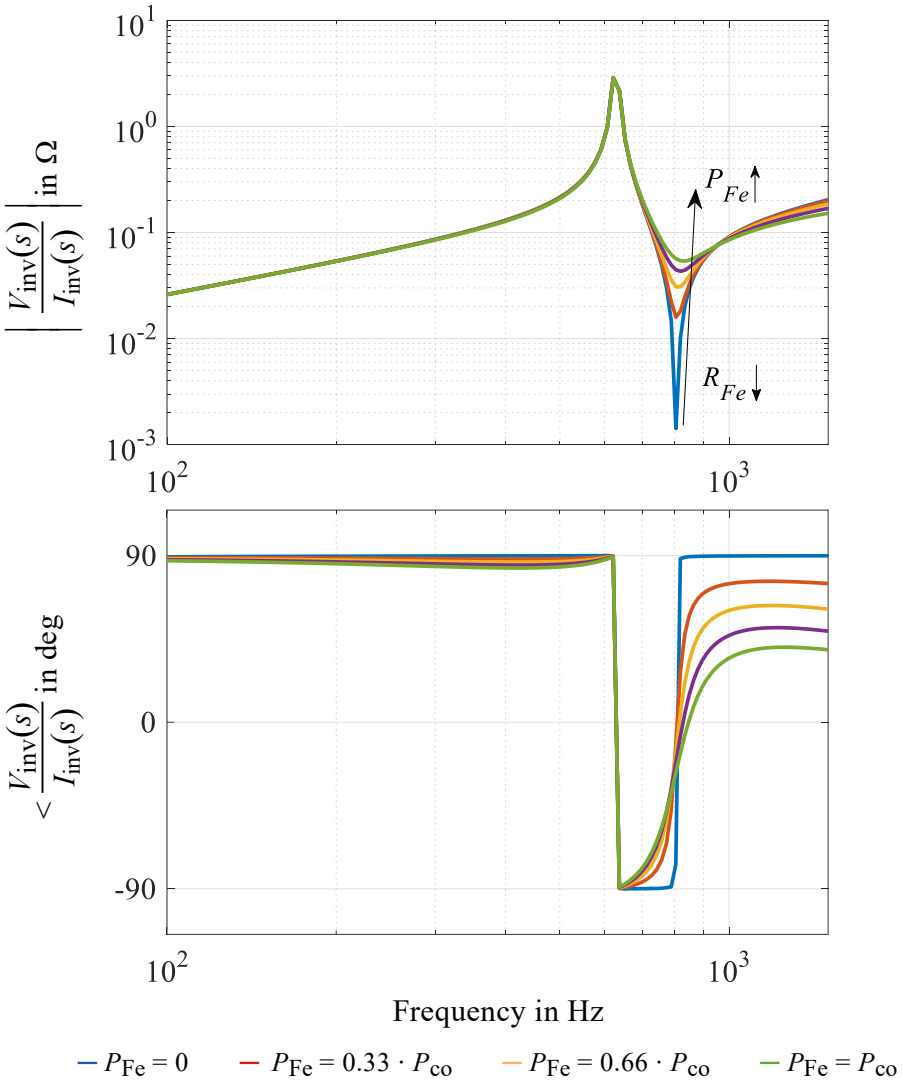

Figure 6.10: Impedance characteristics of the LC-Filter of the parallel equivalent circuit (see Figure 6.7) for various iron losses (0 % − 100 % of the copper losses). The damping is significantly stronger for higher iron losses at the resonance since iron losses increase with frequency ($P_{\mathrm{Fe}} \propto f^2$).

A solution for future investigations for such test benches could be the implementation of air coils. These will have additional problems regarding stray fields and will increase in size significantly but feature zero iron losses.

The calculation example assumed the same core material for the high-voltage and low-voltage setups with the Steinmetz parameters $\alpha = 2$ and $\beta = 2$. This assumption was necessary for the equivalent circuit to match the iron loss effect. In reality, modern core material features much lower Steinmetz parameters (iron powder cores with $\alpha = 1.15$, ferrite cores with $\alpha = 1.24$, and nanocrystalline cores with $\alpha = 1.69$ – see Table A.2 in the appendix [100], [101]), especially for low-voltage core setups. Thus, the calculations and Figure 6.7 firmly over exaggerate the increased damping effect in the low-voltage configuration. However, the illustrated problem is still valid and should be taken into account.

Overall, the test bench was carefully designed to feature very low resistive components. Thus, the system′s resonance problem is still severe. Subchapter 6.3 illustrates these oscillation issues. Consequently, the experimental setup still holds validity for verifying the simulation results. The discussed issues remain an issue of low-voltage setups and will be part of future research.

6.2. Control Implementation

The control algorithm is implemented on the DSP Texas Instruments TMS320 and the FPGA Xilinx Spartan (XC3S1200E) (controller board – see Figure 6.2). The DSP code is written directly in the software environment C via the Code Composer Studio by Texas Instruments. The FPGA is coded in HDL using the software environment Xilinx ISE.

The FPGA handles the sampling of the measurement signals. Further, the FPGA receives the reference voltages from the DSP and carries out the PWM. Finally, the FPGA sends the half-bridge signals through isolation chips toward the gate drivers of the inverter (inverter board – see Figure 6.3).

The DSP obtains the measurement signals from the FPGA and executes the entire control structure, including the observers. Additionally, the DSP manages the over-voltage and over-current protection and the start-up (pre-charge of DC-Link and filter, PLL-convergence, etc.) and turn-off procedures.

Control Flowchart – Control Interrupt

Figure 6.11 illustrates the flowchart of the control algorithm on the DSP. At the start of each interrupt, the measured values and the reference voltages are updated on the FPGA-DSP bus. Since the PLL is used to estimate the future angle (see Figure 6.13), the PLL does not execute at the beginning of the code. Instead, the new PLL runs when values of the future

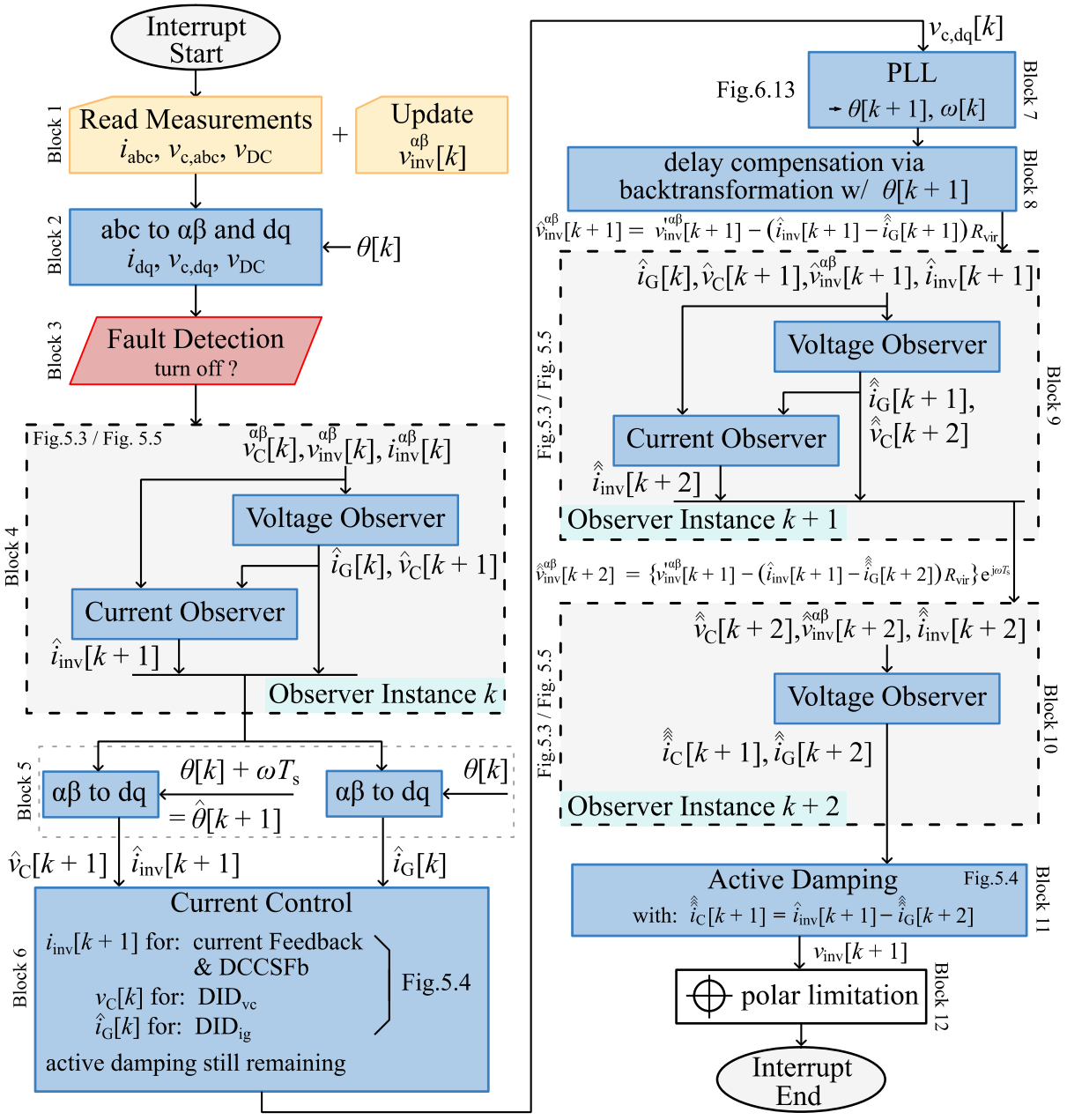

Figure 6.11: Flowchart of the DSP control interrupt. The observer and control structures are shown in more detail in Figure 5.3 and Figure 5.4. Polar limitation is held out twice – also for observers, but for clarity shown only once in this figure.

time instance $k + 1$ are needed for the delay compensation via the back-transformation with the future angle (Block 8). The order of execution of the different observer instances is vital to avoid algebraic loops. Since $\hat{\hat{i}}_G[k+1]$and $\hat{\hat{i}}_G[k+2]$ are needed for future time instances of v_{inv}, estimates have to be used, as shown in Figure 5.4.

Control Flowchart – Start-Up

Figure 6.12 shows the flowchart of the start-up procedure. The test bench uses a DC-source connected to the DC-link at this stage. Thus, a pre-charge resistor is implemented.

After fully charging the DC-link, a contactor bypasses this pre-charge resistor. Similar, the filter capacitors will be pre-charged and bypassed after 4 s, as shown in Figure 6.1. Bypassing this pre-charge resistor excites the resonance. Thus, the resistance value should

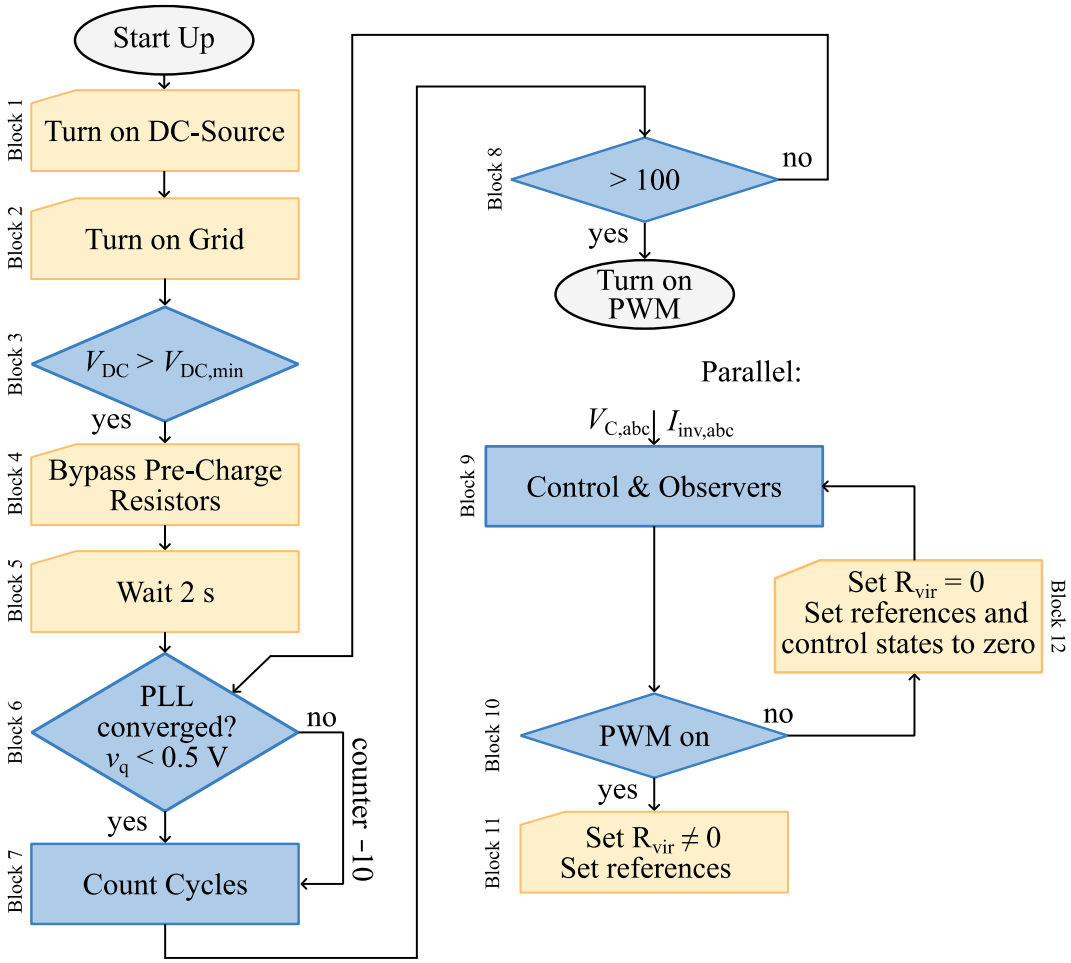

Figure 6.12: Flow-chart of the start-up procedure of the LCL test bench. The test bench utilizes pre-charge resistors for the charging of the DC-Link and the grid filter capacitors. During the start-up, the observers are running with $v_{inv} = v_C$ and $R_{vir} = 0$.

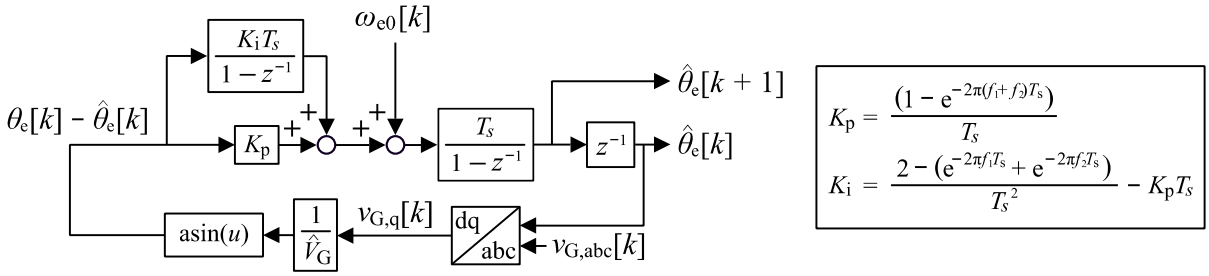

Figure 6.13: State block diagram of the discrete PLL implemented on the test bench. The PLL uses asin(u) and $\hat{V}_G^{-1}$ to decouple the nonlinearities of the Park-Transformation.

not exceed certain limits. The value of this pre-charge resistor has been evaluated via simulation, as shown in the appendix subchapter 9.4.

After the pre-charging, the system will wait for the PLL and the observers to converge before activating the PWM. During this wait time, the inverter is not active, and thus no damping via any control means occurs. Therefore, the active damping coefficient R_{vir} is set to zero within the observers during this period.

6.3. Measurement Results

This subchapter presents the command tracking plots from the test bench. Figure 2.9 illustrates the access to a virtual disturbance to extract dynamic stiffness plots from a first-order RL-load. However, this technique does not apply to the second-order LC filter problem. A disturbance source must be installed to evaluate the simulation results regarding the impedance seen from the grid. Future projects plan to introduce multiple inverters into the test bench. These inverters should operate simultaneously to evaluate the parallel operation. Further, additional inverters can be used as a disturbance source to extract dynamic stiffness plots. However, the test bench currently provides only command tracking frequency response estimation plots.

The grid impedance of the laboratory setup is unknown. Thus, the simulation plots are not exact replicas, but the experiments of this subchapter yield similar attributes and trends. Future work includes both simulation and experimental work to estimate the full-state model of the system more accurately to reproduce the experimental results more closely.

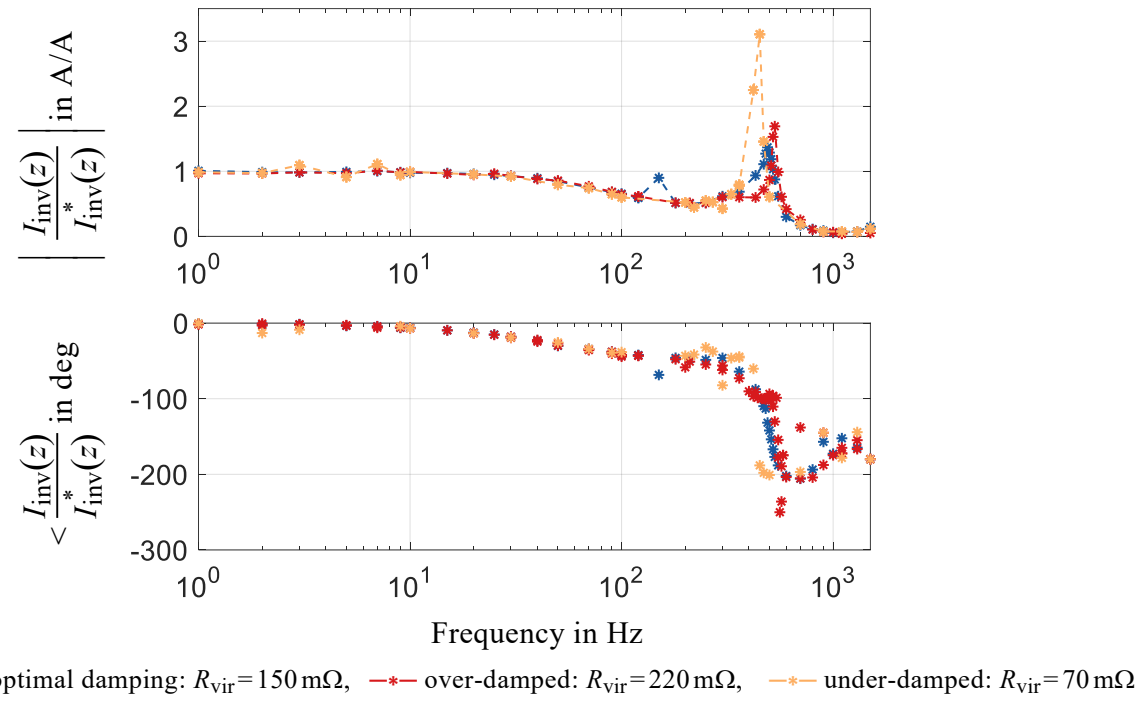

Figure 6.14: *Measurement*: Command tracking FRF for different active damping coefficients of the discrete current controller for the LC-topology on the test bench setup (w/ computational delay, 3 kHz *singe-sampling*) using a deadbeat-based cascaded discrete Luenberger-style observer structure (see Figure 5.3 and Figure 5.4) for estimation of present and future state-information for the grid-current, inverter-current, and capacitor-voltage.

The test setup utilizes both single- (3 kHz) and double-sampling (6 kHz). With single-sampling, the control was too oscillatory without active damping to find any working operating point. This instability was already present in the simulations, as described in subchapter 4.2.2.

Single-Sampling

Figure 6.14 shows the command tracking plot for different damping coefficients for single-sampling (3 kHz switching and 3 kHz sampling). Figure 6.15 (left) shows the peak of the resonant of the command tracking behavior and the respective frequency for different R_{vir}. This resonant behavior can be damped via active damping.

Figure 4.5 and Figure 4.6 of subchapter 4.2.1 illustrated this behavior with pole-zero plots. With increasing damping factor, the resonant frequency increases slightly, as well.

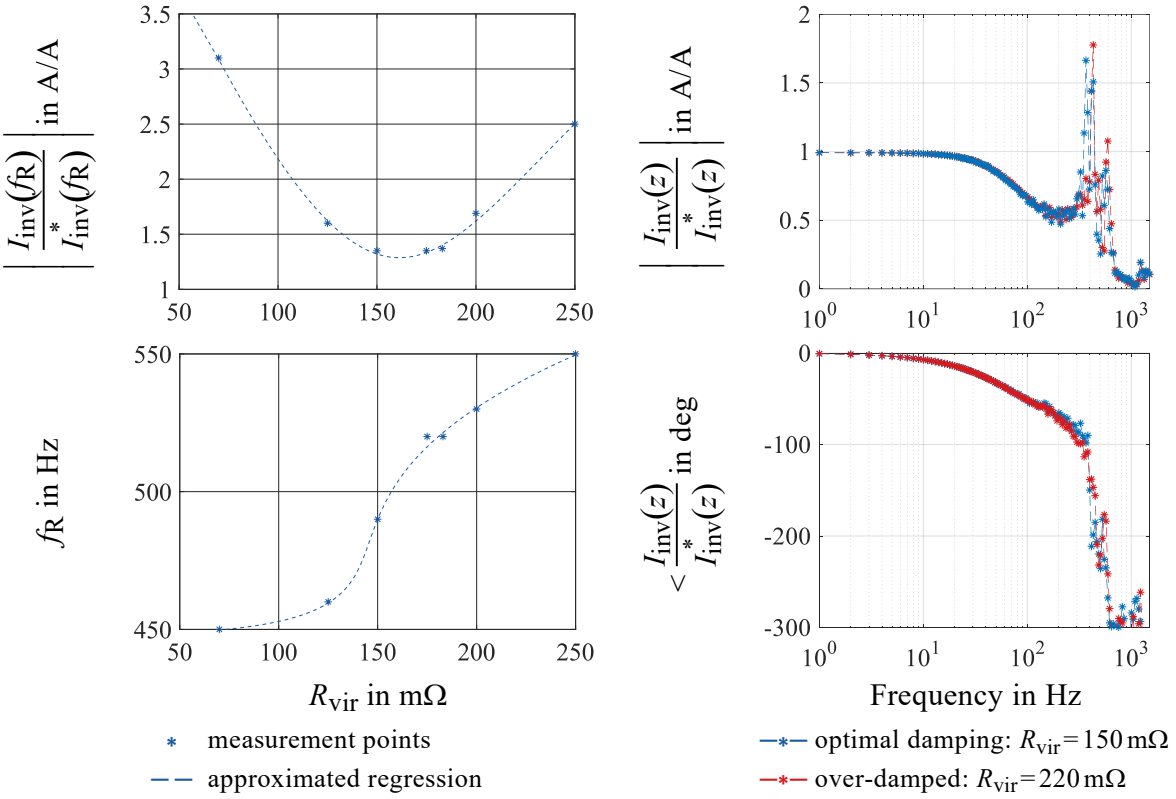

Figure 6.15: For 3 kHz *single-sampling*: *Left*: Measurement: *Left-Top*: Oscillatory peak in the command tracking FRF over the damping coefficient R_{vir}, *Left-Bottom*: Frequency of the oscillatory peak in the command tracking FRF over the damping coefficient — *Right*: Simulation: Command tracking FRF with reduced grid-impedance by one order of magnitude – similar behavior to measurements achieved – see Figure 6.14.

Figure 4.5 further shows that over-damping will also yield instability. This over-damping issue was also present during the experiment and can be seen in Figure 6.14.

A lower damping coefficient was optimal in the test bench compared to the simulation results. Further, the resonant behavior was not present in the simulation. Closer inspections suggested that the potentially most significant difference between simulation and the hardware example was the grid impedance.

The lab's grid connection is an order of magnitude stronger than the original wind turbine application. This strong grid example seems unrealistic for the given application. However, the effect should be investigated further. Figure 6.15 (right) shows similar attributes in simulations with much smaller grid impedances. As described in subchapter 4.2.1, the location of the EVs depends on the grid impedance. These grid impedances can change over time, but most applications should not drastically change in order of magnitude.

Figure 6.16 (left) shows the eigenvalue movement for the variation in grid impedances. Further, Figure 6.16 (right) shows that lower damping coefficients yield stronger relative eigenvalue movement for a low grid impedance. In this case, over-damping and instability happen much sooner than in the weaker grid example.

To summarize, the order of magnitude of the grid impedance also dictates the order of magnitude for effective damping coefficients. Therefore, in the case of grid-impedances

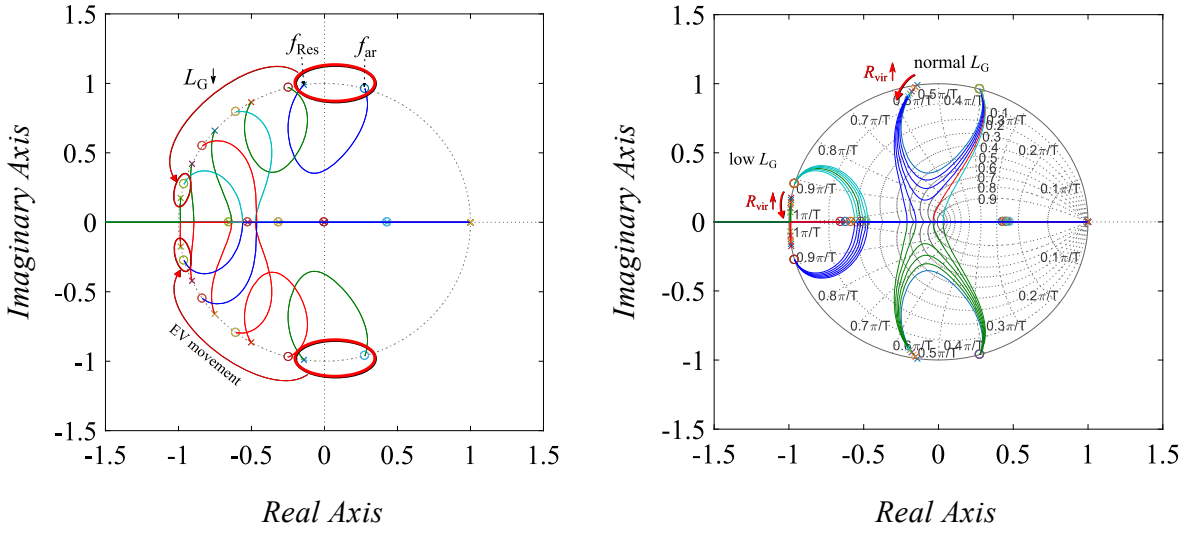

Figure 6.16: *Left*: eigenvalue movement of the LC-plant for decreasing grid impedance (L_G); *Right*: eigenvalue movement for increasing R_{vir} for two cases of grid impedances (low and normal) – the plots are for 3 kHz *single-sampling*.

varying in large regions, adaptive tuning of the damping coefficients could guarantee stability and well-behaved dynamic attributes for the proposed control scheme.

Double-Sampling

Figure 6.17 shows the command tracking plot of the test bench for double-sampling (6 kHz) with and without active damping. Similar to the simulation results in Figure 3.7 of subchapter 3.2, well-behaved command tracking attributes can be observed without damping.

Figure 3.7 reveals that command tracking attributes are not affected negatively without active damping in the case of fast sampling (continuous as an extreme example). However, resonant properties still occur regarding the impedance seen from the grid (see Figure 3.7). Thus, active damping is implemented, and the tracking dynamics remain well behaved. Figure 6.17 shows the same behavior for command tracking on the test bench.

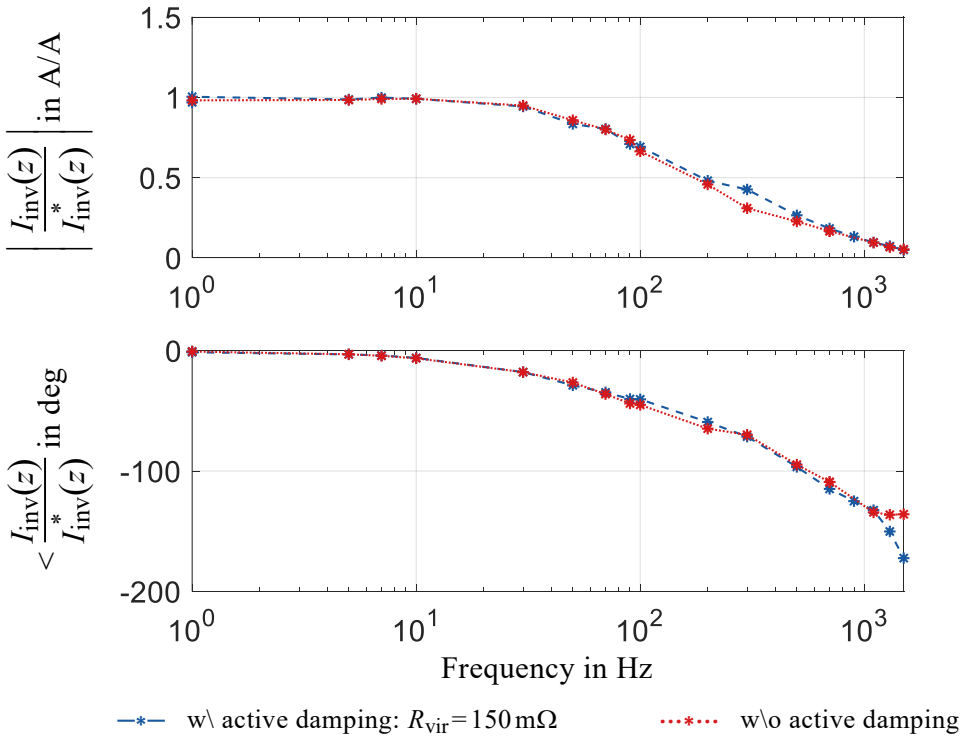

Figure 6.17: Measurements: Command tracking FRF with and without active damping of the discrete current controller for the LC-topology on the test bench setup with double-sampling (w/ computational delay, 6 kHz *double-sampling*) using a deadbeat-based discrete Luenberger-style observer structure for estimation of the future state information of the inverter current.

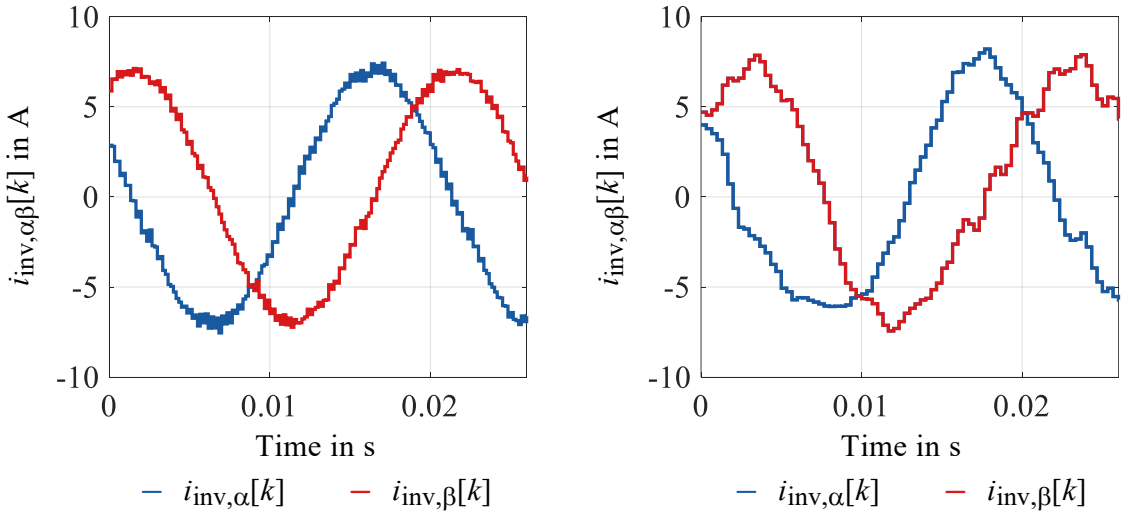

Figure 6.18: Measurements: Time domain plot of the αβ inverter currents with the proposed current control scheme for 6 kHz *double-sampling* on the *left* and for 3 kHz *single-sampling* on the *right*.

Figure 6.18 shows the time domain plot of the α/β-currents comparing double- and single-sampling. The visible harmonics in the single-sampling case are mainly the -2^{nd} and 4^{th} harmonics caused by the PWM. As described in subchapter 5.2.1, these harmonics get mitigated in case of double sampling.

6.4. Interpretation and Limits of the Measurements

The measurements of subchapter 6.3 exhibit the effectiveness of the proposed control scheme. However, the FRFs of the test bench do not perfectly match the simulation results. Multiple effects will be discussed in this subchapter:

- Sampling
- Grid-impedance / resonance
- Loss-effects

Sampling

Subchapter 5.2.1 describes sampling issues for the voltage measurement. The current waveform dictates the standard sampling timing on inductive loads. Consequently, the sampling occurs during the extrema of the PWM carrier signal. This yields magnitude and angle errors for the voltage measurement, depending on the grid impedance. These angle and magnitude errors also yield discrepancies between the sampled currents and voltages. Consequently, the observers become slightly inaccurate, as well.

This issue could be tackled by an improved sampling scheme (sampling between extrema), which would decrease the available computation time. Another solution is faster sampling, reducing the available computation time and increasing the switching frequency (if double-sampling is insufficient).

Grid Impedance / Resonance

While the control algorithm itself does not need grid-impedance information, the order of magnitude of the grid-impedance still affects the eigenvalues, the resonant point, and, consequently, the same design choices. Subchapter 6.3 describes the influence of the grid-impedance on the eigenvalue movement and the consequent effect of the virtual impedance. For a highly varying grid-impedance, the control design and its parameters must be dynamic regarding these changes. This approach seems inevitable if increasing the sampling frequency is not an option.

Increasing the sampling frequency decreases phase and delay issues and improves the observers' performance and the current control scheme. Chapter 5 and subchapter 6.3 illustrate these advantages with the double-sampling technique.

The proposed algorithm cannot be applied to every possible type of grid impedance. The resulting resonance must stay well below the sampling frequency. Otherwise, the voltage drop of the virtual impedance cannot be modulated by the PWM. Further, small resonant eigenvalues will yield a slower possible current control (has to be below resonant frequency) and cause issues as described in subchapter 6.3 (inconvenient eigenvalue locations – see Figure 6.16).

Future work should include proper grid-impedance estimation. While too weak grids cannot be compensated for, too strong grids can be adjusted by implementing more impedance behind the filter.

Loss-Effects

Subchapter 6.1 illustrates the issues of the scaling invariant components for a low-voltage test bench. The iron loss influence and damping attributes, for instance, are difficult to describe. The parallel R_{Fe} model (subchapter 6.1.3) is inaccurate to describe this phenomenon, let alone can be adequately scaled into available low-voltage components. However, this first-order approach serves as a simplified model to give physical insights into the scaling issue. However, the presented obstacles are exaggerated due to the simplified model. Theoretically, a design that results in similar damping attributes for a

specific frequency can be achieved but will fail to represent the original setup over a wide range of frequencies.

Summary

The validity of the damping results of low-voltage test benches is limited regarding passive damping attributes. However, this work carefully designed the passive components of the test bench to yield low resistivity. Thus, the results still show strong resonant behavior. The test bench can evaluate the effectiveness of the active damping from a command tracking perspective but lacks an external disturbance source to assess the simulation results regarding dynamic stiffness (impedance seen from the grid). Further work should investigate the grid impedance and adjust for too strong grids by implementing additional impedance.

Most of the described limits can be solved via faster sampling. The results of the given applications suggest that the double-sampling technique suffices to achieve an excellent outcome.

7. Conclusion

This work demonstrates the systematic LC current control design approach starting from the continuous LC-resonant phenomenon and a consequent continuous design idea to an algorithm implemented on a discrete DSP/FPGA-based system. Furthermore, the design choices are closely linked to the impedance seen from the grid (dynamic stiffness), as this metric provides the most significant insight as to whether actual damping is provided to the overall system.

The simulation and experimental results illustrate that the proposed active damping scheme provides vital and dynamically well-behaved damping attributes. However, each step in complexity, from the continuous domain approach to the discrete domain approach to the implementation space, introduces various identified and solved issues in the respective chapters.

Chapter 4 demonstrates a cohesive discrete modeling approach. This chapter introduces a new modeling approach for a reduced state-vector model due to the position of the sensors for the LC-topology (measurement of inverter current and capacitor voltage; control of inverter current).

Further, issues of the implementation space, such as the computational delay, are introduced. This work proposes a discrete Luenberger-style observer structure to estimate the capacitor current. Further, chapter 5 presents a cascaded observer structure to estimate future states for delay compensation.

Finally, the work describes the design of a low-voltage laboratory setup. The scaling of the original components is expressed vigorously. Chapter 6 shows how to scale the passive components and the proper representation of the IGBT with adjusted MOSFETs. The gate signals of the MOSFETs had to be modified to show similar voltage flanks and dead times. The experimental results are the basis of evaluation for the design and simulation of the previous chapters.

The simulation and experimental results display very effective damping of the LC resonance without information on the grid-impedance. However, the algorithm's limits, including the influence of the grid-impedance, are lined out in subchapter 6.4.

Borwin 1 Showcase

To get an idea of whether this method would have prevented the Borwin 1 accident, some assumptions must first be made. The first assumption is that the damage was caused by overheating damping resistors of the LC-filter of the wind turbines. Secondly, the design comparison assumes the same LC-filter parameters as presented in this thesis. Further, the dimensioning of the damping resistor presumes an optimal damping coefficient of $\xi = 1/\sqrt{2}$ as shown in [78, 102]. Equation (7.1) illustrates the transfer function of the LCL [78]. Consequently, (7.2) shows the dimensioning for the damping resistor R_d for a given damping coefficient ξ. For the parameters of Table A.1, this results in a damping resistor of 78 mΩ.

$$\frac{I(s)}{V(s)} = \frac{1}{Ls} \frac{\left(s^2 + \frac{R_\mathrm{d}}{L_\mathrm{G}} s + \frac{1}{C \cdot L_\mathrm{G}}\right)}{s^2 + \frac{(L + L_\mathrm{G}) \cdot R_\mathrm{d}}{L \cdot L_\mathrm{G}} s + \omega_\mathrm{Res}^2} = \frac{1}{Ls} \frac{\left(s^2 + \frac{R_\mathrm{d}}{L_\mathrm{G}} s + \frac{1}{C \cdot L_\mathrm{G}}\right)}{s^2 + 2\omega_\mathrm{Res}\xi \cdot s + \omega_\mathrm{Res}^2} \tag{7.1}$$

$$R_\mathrm{d} = \frac{2\xi}{C \cdot \omega_\mathrm{Res}} = \frac{\sqrt{2}}{C \cdot \omega_\mathrm{Res}} = 78\,\mathrm{m\Omega}. \tag{7.2}$$

A disturbance from the grid yields the strongest current reaction through the damping resistor at the LC-resonance ω_r seen from the grid. The effective impedance at that frequency is the damping resistor R_d. The nominal current through the damping resistor i_rn can be approximated via the nominal grid voltage v_n (in root mean square):

$$i_\mathrm{rn} = \frac{v_\mathrm{n}}{C \cdot 2\pi \cdot 50} = 0.77 \cdot v_\mathrm{n}. \tag{7.3}$$

The approximated nominal power in each resistor p_rn that has to be dissipated and cooled accordingly is:

$$p_\mathrm{rn} = {i_\mathrm{rn}}^2 \cdot R_\mathrm{d} = 0.6 \cdot R_\mathrm{d} \cdot {v_\mathrm{n}}^2 = 7.4\,\mathrm{kW} \tag{7.4}$$

The additional losses from a disturbance voltage v_d at the LC-resonance seen from the grid can be calculated as follows:

$$p_\mathrm{res} = \frac{{v_\mathrm{d}}^2}{Z_\mathrm{d}(\omega = \omega_\mathrm{r})} = \frac{{v_\mathrm{d}}^2}{R_\mathrm{d}} = 12.9 \cdot {v_\mathrm{d}}^2. \tag{7.5}$$

Assuming the resistor and its cooling can withstand total losses of $n_\mathrm{tot} \cdot p_\mathrm{rn}$, the disturbance voltage v_d has to obey the following to avoid destruction:

$$v_d < \frac{\sqrt{2 \cdot (1 - n_{tot})}}{C^2 \cdot 2\pi \cdot 50 \cdot \omega_{Res}} v_n = 0.77 \cdot R_d \cdot \sqrt{1 - n_{tot}} \cdot v_n = 0.06 \cdot \sqrt{1 - n_{tot}} \cdot v_n \quad (7.6)$$

If the resistor and its cooling were designed to withstand up to 130 % of the nominal power p_{rn} (9.6 kW), the disturbance voltage could not exceed 3.3 % of the nominal grid voltage. The current through the damping resistor would be 168 A at the breaking point.

Figure 5.11 shows the effective impedance seen from the grid over a wide frequency range. At the resonance point, the impedance is somewhere between 70 mΩ and 80 mΩ which is very close to the optimal passive damping resistor R_d. However, the resonant frequency seen from the grid depends on the grid impedance and thus could be lower. At lower frequencies, the harmonic impedance (Figure 5.11) drops down to 25 mΩ. Therefore, the active damping case could result in a similar current reaction at higher frequencies of approximately 170 A or up until 530 A at lower frequencies. Nevertheless, the resonant current is not dissipated in a damping resistor. It thus will not lead to overheating or any other failure mechanism unless other passive components cannot withstand the additional current.

Future Work

Future work should focus on implementing a disturbance source to evaluate dynamic stiffness plots for the experimental setup. This setup can be another similar inverter but with a much higher sampling and switching frequency to allow quasi-continuous FRFs, which is crucial for the correct phase interpretation for passivity analysis. Further, this setup or the disturbance source must be bidirectional in power flow for such measurements. Thus, the arrangements should be designed as a back-to-back configuration.

Additional investigations regarding the grid-impedance of the laboratory setup would help match the application's original grid strength. In the case of a strong laboratory grid, the grid impedance has to be increased via additional impedances.

8. References

[1] T. Thomas, *Troubleshooting continues.* [Online]. Available: https://www.offshorewindindustry.com/news/troubleshooting-continues (accessed: 12.May.2020).

[2] Welt.de, *Rätselhafter Defekt legt größten Windpark lahm.* [Online]. Available: https://www.welt.de/wirtschaft/article131879638/Raetselhafter-Defekt-legt-groessten-Windpark-lahm.html (accessed: 12.May.2020).

[3] C. Buchhagen, C. Rauscher, A. Menze, and J. Jung, "BorWin1 - First Experiences with harmonic interactions in converter dominated grids," in *International ETG Congress 2015; Die Energiewende - Blueprints for the new energy age*, 2015, pp. 1–7.

[4] Cuili Chen, Zhiqiang Wang, Yulong Zhang, Guofeng Li, and Yan Wu, "A novel passive damping LCL-filter for active power filter," in *2014 IEEE Conference and Expo Transportation Electrification Asia-Pacific (ITEC Asia-Pacific)*, 2014, pp. 1–5.

[5] M. Swamy, "A novel active damping scheme for use with regenerative converters," in *2017 IEEE Energy Conversion Congress and Exposition (ECCE)*, 2017, pp. 5073–5079.

[6] B. Abdeldjabar, Xu Dianguo, X. Wang, and F. Blaabjerg, "Robust active damping control of LCL filtered grid connected converter based active disturbance rejection control," in *2016 IEEE 8th International Power Electronics and Motion Control Conference (IPEMC-ECCE Asia)*, 2016, pp. 2661–2666.

[7] J. Dannehl, C. Wessels, and F. W. Fuchs, "Limitations of Voltage-Oriented PI Current Control of Grid-Connected PWM Rectifiers With LCL Filters," *IEEE Transactions on Industrial Electronics*, vol. 56, no. 2, pp. 380–388, 2009, doi: 10.1109/TIE.2008.2008774.

[8] H. Ge, Y. Zhen, Y. Wang, and D. Wang, "Research on LCL filter active damping strategy in active power filter system," in *2017 9th International Conference on Modelling, Identification and Control (ICMIC)*, 2017, pp. 476–481.

[9] H. Yuan and X. Jiang, "A simple active damping method for Active Power Filters," in *2016 IEEE Applied Power Electronics Conference and Exposition (APEC)*, 2016, pp. 907–912.

[10] Hu Wei, Zhou Hui, Sun Jian-jun, Jiang Yi-ming, and Zha Xiao-ming, "Resonance analysis and suppression of system with multiple grid-connected inverters," in *2015 IEEE 2nd International Future Energy Electronics Conference (IFEEC)*, 2015, pp. 1–6.

[11] J. Kukkola, M. Hinkkanen, and K. Zenger, "Observer-Based State-Space Current Controller for a Grid Converter Equipped With an LCL Filter: Analytical Method for Direct Discrete-Time Design," *IEEE Transactions on Industry Applications*, vol. 51, no. 5, pp. 4079–4090, 2015, doi: 10.1109/TIA.2015.2437839.

[12] M. Büyük, A. Tan, M. İnci, and M. Tümay, "A notch filter based active damping of llcl filter in shunt active power filter," in *2017 International Symposium on Power Electronics (Ee)*, 2017, pp. 1–6.

[13] M. Büyük, M. İnci, A. Tan, and M. Tümay, "Capacitor current feedback active damping for Shunt Active Power Filter with output LLCL filter," in *2017 10th International Conference on Electrical and Electronics Engineering (ELECO)*, 2017, pp. 376–379.

[14] S. Zhen-Ao, Y. Zi-Long, W. Yi-Bo, and X. Hong-Hua, "Analysis of harmonic resonances among parallel grid-connected inverters," in *2014 International Conference on Power System Technology*, 2014, pp. 3071–3077.

[15] Surasak Nuilers and B. Neammanee, "Control performance of active damp LCL filter of three phase PWM boost rectifier," in *ECTI-CON2010: The 2010 ECTI International Confernce on Electrical Engineering/Electronics, Computer, Telecommunications and Information Technology*, 2010, pp. 259–263.

[16] W. Zhao and G. Chen, "Comparison of active and passive damping methods for application in high power active power filter with LCL-filter," in *2009 International Conference on Sustainable Power Generation and Supply*, 2009, pp. 1–6.

[17] Y. Shi and J. Su, "An active damping method based on PR control for LCL-filter-based grid-connected inverters," in *2014 17th International Conference on Electrical Machines and Systems (ICEMS)*, 2014, pp. 944–948.

[18] L. Zhou *et al.,* "Inverter-Current-Feedback Resonance-Suppression Method for LCL-Type DG System to Reduce Resonance-Frequency Offset and Grid-Inductance Effect," *IEEE Transactions on Industrial Electronics*, vol. 65, no. 9, pp. 7036–7048, 2018, doi: 10.1109/TIE.2018.2795556.

[19] H. Kim, M. W. Degner, J. M. Guerrero, F. Briz, and R. D. Lorenz, "Discrete-Time Current Regulator Design for AC Machine Drives," *IEEE Transactions on Industry Applications*, vol. 46, no. 4, pp. 1425–1435, 2010, doi: 10.1109/TIA.2010.2049628.

[20] L. Harnefors, X. Wang, A. G. Yepes, and F. Blaabjerg, "Passivity-Based Stability Assessment of Grid-Connected VSCs—An Overview," *IEEE Journal of Emerging and Selected Topics in Power Electronics*, vol. 4, no. 1, pp. 116–125, 2016, doi: 10.1109/JESTPE.2015.2490549.

[21] T. Geyer, *Model predictive control of high power converters and industrial drives*. Chichester West Sussex UK: John Wiley & Sons Inc, 2016.

[22] M. Schütt and H. Eckel, "Design and analysis of complex vector current regulators for modular multilevel converters," in *2017 19th European Conference on Power Electronics and Applications (EPE'17 ECCE Europe)*, 2017, pp. 1–10.

[23] M. Schütt and H. Eckel, "Design and Analysis of Discrete Current Regulators for VSIs," in *2018 20th European Conference on Power Electronics and Applications (EPE'18 ECCE Europe)*, 2018, pp. 1–10.

[24] M. Schütt and H. Eckel, "Discrete Active Damping Control Design for LCL-Resonances Using Observers," in *2019 21st European Conference on Power Electronics and Applications (EPE '19 ECCE Europe)*, 2019, pp. 1–10.

[25] G. K. Sah, M. Schütt, and H. -G. Eckel, "Comparison of Decoupling Techniques via Discrete Luenberger Style Observer for Voltage Oriented Control," in *2020 22nd European Conference on Power Electronics and Applications (EPE'20 ECCE Europe)*, 2020, pp. 1–10.

[26] F. Briz, M. W. Degner, and R. D. Lorenz, "Analysis and design of current regulators using complex vectors," *IEEE Transactions on Industry Applications*, vol. 36, no. 3, pp. 817–825, 2000, doi: 10.1109/28.845057.

[27] M. Büyük, M. İnci, A. Tan, and M. Tümay, "Capacitor current feedback active damping for Shunt Active Power Filter with output LLCL filter," in *2017 10th International Conference on Electrical and Electronics Engineering (ELECO)*, 2017, pp. 376–379.

[28] I. Lar, M. M. Radulescu, E. Ritchie, and A. A. Pop, "Current control methods for grid-side three-phase PWM voltage-source inverter in distributed generation systems," in *2012 13th International Conference on Optimization of Electrical and Electronic Equipment (OPTIM)*, 2012, pp. 859–867.

[29] K. Y. Ahmed, N. Z. Yahaya, V. S. Asirvadam, K. Ramani, and O. Ibrahim, "Comparison of fuzzy logic control and PI control for a three-level rectifier based on voltage oriented control," in *2016 IEEE International Conference on Power and Energy (PECon)*, 2016, pp. 127–132.

[30] A. Kihel, F. Krim, and A. Laib, "MPPT voltage oriented loop based on integral sliding mode control applied to the boost converter," in *2017 6th International Conference on Systems and Control (ICSC)*, 2017, pp. 205–209.

[31] H. Qi, Y. Wu, and Y. Bi, "The main parameters design based on three-phase voltage source PWM rectifier of voltage oriented control," in *2014 International Conference on Information Science, Electronics and Electrical Engineering*, 2014, pp. 10–13.

[32] H.-C. Moon, J.-S. Lee, J.-H. Lee, and K.-B. Lee, "MPC-SVM method with subdivision strategy for current ripples reduction and neutral-point voltage balance in three-level inverter," in *2017 IEEE Energy Conversion Congress and Exposition (ECCE)*, 2017, pp. 191–196.

[33] R. G. Omar, "FCS-MPC strategy for a five-phase voltage source inverter using maximum load current constraint," in *2018 1st International Scientific Conference of Engineering Sciences - 3rd Scientific Conference of Engineering Science (ISCES)*, 2018, pp. 98–103.

[34] L. Xia, Z. Chen, Q. Yang, L. Xu, S. Bao, and B. Wu, "Research on Grid-side Control for a Medium Voltage Direct-Connected Cascaded Inverter Based on Model Predictive Control Under Weak Grid Conditions," in *2021 IEEE 16th Conference on Industrial Electronics and Applications (ICIEA)*, 2021, pp. 627–632.

[35] X. Wang, Y. Zhang, H. Yang, B. Zhang, J. Rodriguez, and C. Garcia, "A Model-Free Predictive Current Control of Induction Motor Based on Current Difference," in *2020 IEEE 9th International Power Electronics and Motion Control Conference (IPEMC2020-ECCE Asia)*, 2020, pp. 1038–1042.

[36] T.-T. Nguyen, H.-J. Yoo, and H.-M. Kim, "Model Predictive Control of Inverters in Microgrid with Constant Switching Frequency for Circulating Current Suppression," in *TENCON 2018 - 2018 IEEE Region 10 Conference*, 2018, pp. 1566–1571.

[37] F. Hans and W. Schumacher, "Modeling and small-signal stability analysis of decentralized energy sources implementing Q(U) reactive power control," in *2017 11th IEEE International Conference on Compatibility, Power Electronics and Power Engineering (CPE-POWERENG)*, 2017, pp. 588–593.

[38] M. Calabria and W. Schumacher, "Stability optimization for distributed generation of load-following energy," in *2014 IEEE International Energy Conference (ENERGYCON)*, 2014, pp. 1034–1041.

[39] V. Hovelaque, C. Commault, and J. M. Dion, "Poles and zeros of linear structured systems," in *1997 European Control Conference (ECC)*, 1997, pp. 3234–3239.

[40] Y. Liu and P. H. Bauer, "On pole-zero patterns of non-negative impulse response discrete-time systems with complex poles and zeros," in *2009 17th Mediterranean Conference on Control and Automation*, 2009, pp. 1102–1107.

[41] F. Briz, P. García, M. W. Degner, D. Díaz-Reigosa, and J. M. Guerrero, "Dynamic Behavior of Current Controllers for Selective Harmonic Compensation in Three-Phase Active Power Filters," *IEEE Transactions on Industry Applications*, vol. 49, no. 3, pp. 1411–1420, 2013, doi: 10.1109/TIA.2013.2253537.

[42] R. D. Lorenz, T. A. Lipo, and D. W. Novotny, "Motion control with induction motors," *Proceedings of the IEEE*, vol. 82, no. 8, pp. 1215–1240, 1994, doi: 10.1109/5.301685.

[43] M. J. Ryan, W. E. Brumsickle, and R. D. Lorenz, "Control topology options for single-phase UPS inverters," *IEEE Transactions on Industry Applications*, vol. 33, no. 2, pp. 493–501, 1997, doi: 10.1109/28.568015.

[44] D. Serfontein, J. Rens, and G. Botha, "Harmonic impedance assessment using prevailing phasors," in *2018 18th International Conference on Harmonics and Quality of Power (ICHQP)*, 2018, pp. 1–5.

[45] C. H. van der Broeck, R. W. D. Doncker, S. A. Richter, and J. v. Bloh, "Discrete time modeling, implementation and design of current controllers," in *2014 IEEE Energy Conversion Congress and Exposition (ECCE)*, 2014, pp. 540–547.

[46] C. M. Wolf, M. W. Degner, and F. Briz, "Analysis of current sampling errors in PWM, VSI drives," in *2013 IEEE Energy Conversion Congress and Exposition*, 2013, pp. 1770–1777.

[47] M. Konghirun and L. Xu, "A dq-axis current control technique for fast transient response in vector controlled drive of permanent magnet synchronous motor," in *The 4th International Power Electronics and Motion Control Conference, 2004. IPEMC 2004*, 2004, 1316-1320 Vol.3.

[48] B. Li, S. Huang, X. Chen, and Y. Xiang, "A simplified DQ-frame current controller for single-phase grid-connected inverters with LCL filters," in *2017 20th International Conference on Electrical Machines and Systems (ICEMS)*, 2017, pp. 1–5.

[49] K. Li, X. Liu, J. Sun, and C. Zhang, "Robust current control of PMSM based on PCH and disturbance observer," in *Proceedings of the 33rd Chinese Control Conference*, 2014, pp. 7938–7942.

[50] L. Zhong, M. F. Rahman, W. Y. Hu, and K. W. Lim, "Analysis of direct torque control in permanent magnet synchronous motor drives," *IEEE Transactions on Power Electronics*, vol. 12, no. 3, pp. 528–536, 1997, doi: 10.1109/63.575680.

[51] K. Wang, R. D. Lorenz, and N. Aamir Baloch, "Torque and Speed Response Differences Between Deadbeat-Direct Torque and Flux Control and Indirect Field Oriented Control for Induction Machine Drives," in *2018 IEEE Energy Conversion Congress and Exposition (ECCE)*, 2018, pp. 5428–5435.

[52] Y. Huang and Q. Wang, "Disturbance Rejection of Central Pattern Generator Based Torque-Stiffness-Controlled Dynamic Walking," *Neurocomput*, vol. 170, C, pp. 141–151, 2015, doi: 10.1016/j.neucom.2015.04.096.

[53] W.-S. Yao, I. Hu, G. Kao, M. Shih, and K. Chen, "Dynamic stiffness analysis of repetitive control and applied to Advanced Metrology Analyzer," in *2016 17th International Conference on Electronic Packaging Technology (ICEPT)*, 2016, pp. 1206–1211.

[54] A.D. Shaw, S.A. Neild, and D.J. Wagg, “Dynamic analysis of high static low dynamic stiffness vibration isolation mounts,” *Journal of Sound and Vibration*, vol. 332, no. 6, pp. 1437–1455, 2013, doi: 10.1016/j.jsv.2012.10.036.

[55] Z. Niu, J. Su, Y. Zhang, and H. Lin, “Dynamic Stiffness Characteristics Analysis of Bogie Suspension for Rail Vehicle Based on Big Data-Driven Bench Test,” *IEEE Access*, vol. 6, pp. 79222–79234, 2018, doi: 10.1109/ACCESS.2018.2884957.

[56] Zhu Sihong, Wang Jiasheng, and Zhang Ying, “Research on theoretical calculation model for dynamic stiffness of air spring with auxiliary chamber,” in *2008 IEEE Vehicle Power and Propulsion Conference*, 2008, pp. 1–6.

[57] S. Kim, H. Jeong, and J. S. Lee, “Dynamic Stiffness Improvement of a Grid-tied Voltage Source Inverter,” in *2019 10th International Conference on Power Electronics and ECCE Asia (ICPE 2019 - ECCE Asia)*, 2019, pp. 1389–1394.

[58] M. Weck and K. Teipel, *Handbook of Machine Tools*: Wiley, 1984.

[59] S. A. Tobias, *Machine Tool Vibrations*. New York: Wiley, 1965.

[60] F. Koenigsberger and J. Tlusty, *Machine tool structures*: Pergamon Press, 1970.

[61] Q. Fei, L. Jian-Wen, L. Yong-Gang, S. Wei, and L. Zhong-Liang, “Research on the responsibility partition of harmonic pollution and harmonic impedance based on the total least-squares regression method,” in *2014 International Conference on Power System Technology*, Chengdu, Oct. 2014 - Oct. 2014, pp. 2122–2127.

[62] Jie Bao, Peter L. Lee, *Process Control: The Passive Systems Approach*: Springer-Verlag London.

[63] J. C. Willems, “Dissipative dynamical systems part I: General theory,” *Arch. Rational Mech. Anal.*, vol. 45, no. 5, pp. 321–351, 1972.

[64] J. C. Willems, “Dissipative dynamical systems part II: Linear systems with quadratic supply rates,” *Arch. Rational Mech. Anal.*, vol. 45, no. 5, pp. 352–393, 1972.

[65] V. Bevelevich, *Classical Network Synthesis*. New York, NY, USA: Van Nostrand, 1968.

[66] D.J. Hill and P.J. Moylan, “Stability results for nonlinear feedback systems,” *Automatica*, vol. 13, no. 4, pp. 377–382, 1977, doi: 10.1016/0005-1098(77)90020-6.

[67] G.L. Santosuosso, “Passivity of nonlinear systems with input-output feedthrough,” *Automatica*, vol. 33, no. 4, pp. 693–697, 1997, doi: 10.1016/S0005-1098(96)00200-2.

[68] J.-L. Wang, H.-N. Wu, T. Huang, S.-Y. Ren, and J. Wu, “Passivity and Output Synchronization of Complex Dynamical Networks With Fixed and Adaptive Coupling Strength,” *IEEE Transactions on Neural Networks and Learning Systems*, vol. 29, no. 2, pp. 364–376, 2018, doi: 10.1109/TNNLS.2016.2627083.

[69] J. Dannehl, C. Wessels, and F. W. Fuchs, “Limitations of Voltage-Oriented PI Current Control of Grid-Connected PWM Rectifiers With LCL Filters,” *IEEE Transactions on Industrial Electronics*, vol. 56, no. 2, pp. 380–388, 2009, doi: 10.1109/TIE.2008.2008774.

[70] M. J. Corley and R. D. Lorenz, “Rotor position and velocity estimation for a salient-pole permanent magnet synchronous machine at standstill and high speeds,” *IEEE Transactions on Industry Applications*, vol. 34, no. 4, pp. 784–789, 1998, doi: 10.1109/28.703973.

[71] J. Hu, L. Xu, and J. Liu, “Eddy Current Effects on Rotor Position Estimation for Sensorless Control of PM Synchronous Machine,” in *Conference Record of the 2006 IEEE Industry Applications Conference Forty-First IAS Annual Meeting*, 2006, pp. 2034–2039.

[72] Y. Okajima and K. Akatsu, “Harmonic current control for Interior Permanent Magnet Synchronous Machines applying current controller design method by using complex vectors,”

in *IECON 2016 - 42nd Annual Conference of the IEEE Industrial Electronics Society*, 2016, pp. 2815–2820.

[73] R. H. Park, "Two-reaction theory of synchronous machines generalized method of analysis-part I," *Transactions of the American Institute of Electrical Engineers*, vol. 48, no. 3, pp. 716–727, 1929, doi: 10.1109/T-AIEE.1929.5055275.

[74] A. Soyed, A. Kadri, O. Hassnaoui, and F. Bacha, "Voltage Oriented Control of Indirect Matrix Converter Applied to Wind Energy Conversion System using PMSM Generator," in *2020 7th International Conference on Control, Decision and Information Technologies (CoDIT)*, 2020, pp. 790–795.

[75] A. Tapia, G. Tapia, J. X. Ostolaza, and J. R. Saenz, "Modeling and control of a wind turbine driven doubly fed induction generator," *IEEE Transactions on Energy Conversion*, vol. 18, no. 2, pp. 194–204, 2003, doi: 10.1109/TEC.2003.811727.

[76] R. Kadri, J.-P. Gaubert, and G. Champenois, "An Improved Maximum Power Point Tracking for Photovoltaic Grid-Connected Inverter Based on Voltage-Oriented Control," *IEEE Transactions on Industrial Electronics*, vol. 58, no. 1, pp. 66–75, 2011, doi: 10.1109/TIE.2010.2044733.

[77] C. E. Cook and M. Bernfeld, *Radar Signals - An Introduction to Theory and Application*: Academic Press, 1967.

[78] T. Teodorescu, M. Liserre, and P. Rodriguez, *Grid Converters for Photovoltaic and Wind Power Systems*: IEEE, John Wiley & Sons, Ltd, 2011.

[79] X. Wang, "The Performance Improvements of Self-sensing Control for Permanent Magnet Synchronous Machines," Dissertation, TU Munich, Munich, 2014.

[80] R. Wu and G. R. Slemon, "A permanent magnet motor drive without a shaft sensor," *IEEE Transactions on Industry Applications*, vol. 27, no. 5, pp. 1005–1011, 1991, doi: 10.1109/28.90359.

[81] E. Robeischl, M. Schroedl, and M. Krammer, "Position-sensorless biaxial position control with industrial PM motor drives based on INFORM- and back EMF model," in *IEEE 2002 28th Annual Conference of the Industrial Electronics Society. IECON 02*, 2002, 668-673 vol.1.

[82] G. Foo and M. F. Rahman, "Sensorless direct torque and flux control of IPM synchronous motor drives using an extended rotor flux model," in *2009 Australasian Universities Power Engineering Conference*, 2009, pp. 1–6.

[83] D. Luenberger, "An introduction to observers," *Automatic Control, IEEE Transaction on*, pp. 596–602.

[84] J. Koppinen, J. Kukkola, and M. Hinkkanen, "Plug-In Identification Method for an LCL Filter of a Grid Converter," *IEEE Transactions on Industrial Electronics*, vol. 65, no. 8, pp. 6270–6280, 2018, doi: 10.1109/TIE.2017.2787546.

[85] J. Kukkola and M. Hinkkanen, "Observer-Based State-Space Current Control for a Three-Phase Grid-Connected Converter Equipped With an LCL Filter," *IEEE Transactions on Industry Applications*, vol. 50, no. 4, pp. 2700–2709, 2014, doi: 10.1109/TIA.2013.2295461.

[86] J. Kukkola and M. Hinkkanen, "State Observer for Grid-Voltage Sensorless Control of a Converter Under Unbalanced Conditions," *IEEE Transactions on Industry Applications*, vol. 54, no. 1, pp. 286–297, 2018, doi: 10.1109/TIA.2017.2749305.

[87] J. Kukkola and M. Hinkkanen, "State Observer for Grid-Voltage Sensorless Control of a Converter Equipped With an LCL Filter: Direct Discrete-Time Design," *IEEE Transactions*

on Industry Applications, vol. 52, no. 4, pp. 3133–3145, 2016, doi: 10.1109/TIA.2016.2542060.

[88] J. Kukkola and M. Hinkkanen, "State observer for grid-voltage sensorless control of a grid-connected converter equipped with an LCL filter," in *2014 16th European Conference on Power Electronics and Applications*, 2014, pp. 1–10.

[89] J. Kukkola and M. Hinkkanen, "Observer-Based State-Space Current Control for a Three-Phase Grid-Connected Converter Equipped With an LCL Filter," *IEEE Transactions on Industry Applications*, vol. 50, no. 4, pp. 2700–2709, 2014, doi: 10.1109/TIA.2013.2295461.

[90] F. M. M. Rahman, U. Riaz, J. Kukkola, M. Routimo, and M. Hinkkanen, "Observer-Based Current Control for Converters with an LCL Filter: Robust Design for Weak Grids," in *2018 IEEE 9th International Symposium on Sensorless Control for Electrical Drives (SLED)*, 2018, pp. 36–41.

[91] V. Pirsto, J. Kukkola, and M. Hinkkanen, "Multifunctional Cascade Control of Voltage-Source Converters Equipped With an LC Filter," *IEEE Transactions on Industrial Electronics*, vol. 69, no. 3, pp. 2610–2620, 2022, doi: 10.1109/TIE.2021.3065602.

[92] F. M. M. Rahman, J. Kukkola, V. Pirsto, M. Routimo, and M. Hinkkanen, "Observers for Discrete-Time Current Control of Converters Equipped With an LCL Filter," in *2020 IEEE Energy Conversion Congress and Exposition (ECCE)*, 2020, pp. 2884–2891.

[93] F. M. Mahafugur Rahman, J. Kukkola, V. Pirsto, M. Routimo, and M. Hinkkanen, "State-Space Control for LCL Filters: Comparison Between the Converter and Grid Current Measurements," in *2019 IEEE Energy Conversion Congress and Exposition (ECCE)*, 2019, pp. 1491–1498.

[94] V. Pirsto, J. Kukkola, F. M. Mahafugur Rahman, and M. Hinkkanen, "Real-time Identification Method for LCL Filters Used With Grid Converters," in *2019 IEEE Energy Conversion Congress and Exposition (ECCE)*, 2019, pp. 3729–3736.

[95] F. M. M. Rahman, V. Pirsto, J. Kukkola, M. Routimo, and M. Hinkkanen, "State-Space Control for LCL Filters: Converter Versus Grid Current Measurement," *IEEE Transactions on Industry Applications*, vol. 56, no. 6, pp. 6608–6618, 2020, doi: 10.1109/TIA.2020.3016915.

[96] E. I. Jury, *Theory and application of the z-Transform Method*. Malabar, Fla.: Krieger, 1982.

[97] F. Hans, M. Oeltze, and W. Schumacher, "A Modified ZOH Model for Representing the Small-Signal PWM Behavior in Digital DC-AC Converter Systems," in *IECON 2019 - 45th Annual Conference of the IEEE Industrial Electronics Society*, 2019, pp. 1514–1520.

[98] Rolf Fischer, *Elektrische Maschinen,* 13th ed. München: Carl Hanser Verlag, 2006.

[99] Jonas Mühlethaler, "Modeling and Multi-Objective Optimization of Inductive Power Components," *Dissertation ETH Zürich*, 2012.

[100] K. Detka and K. Górecki, "Modelling the power losses in the ferromagnetic materials," *Materials Science-Poland*, vol. 35, no. 2, pp. 398–404, 2017, doi: 10.1515/msp-2017-0050.

[101] K. Górecki and K. Detka, "Influence of Power Losses in the Inductor Core on Characteristics of Selected DC–DC Converters," *Energies*, vol. 12, no. 10, p. 1991, 2019, doi: 10.3390/en12101991.

[102] O. Jacobs, "The damping ratio of an optimal control system," *IEEE Transactions on Automatic Control*, vol. 10, no. 4, pp. 473–476, 1965, doi: 10.1109/TAC.1965.1098213.

9. Appendix

TABLE A.1

PARAMETERS OF THE ORIGINAL SETUP AND THE SCALED TEST BENCH REPRESENTATION

Parameter	5 MW Wind Turbine	25 V Lab test bench
L_f – filter inductance	25 µH	379 µH (400 µH intended)
R_f – filter resistance	0.3 mΩ	17.8mΩ (5 mΩ intended)
C_f – filter capacitance	4 mF	200 µF
V_{DC} – DC-link voltage	1100 V	40 V
V_G – grid voltage	690 V	25 V
I_N – base current	4500 A	10 A
C_{DC} – DC-link capacitance	92 mF	5.52 mF
f_{sw} – switching frequency	3 kHz	3 kHz
t_{dead} – dead time (half bridge switching)	appr. 2 µs	appr. 2 µs
Switches	1.7 kV Trench/Fieldstop IGBT 4	100 V HEXFET Power MOSFET

9.1. Full-State Discrete LCL Model and Transfer Function Coefficients

Coefficients for the full-state discrete LCL model of (4.17) and (4.18):

$$\mathbf{\Phi} = \mathrm{e}^{\mathbf{A}T_\mathrm{s}} = \begin{bmatrix} \phi_{11} & \phi_{12} & \phi_{13} \\ \phi_{21} & \phi_{22} & \phi_{23} \\ \phi_{31} & \phi_{32} & \phi_{33} \end{bmatrix} = \upsilon \begin{bmatrix} \dfrac{L_\mathrm{f} + L_\mathrm{G}\cos(\omega_\mathrm{Res}T_\mathrm{s})}{L_\mathrm{t}} & -\dfrac{\sin(\omega_\mathrm{Res}T_\mathrm{s})}{\omega_\mathrm{Res}L_\mathrm{f}} & \dfrac{L_\mathrm{G}[1-\cos(\omega_\mathrm{Res}T_\mathrm{s})]}{L_\mathrm{t}} \\ \dfrac{\sin(\omega_\mathrm{Res}T_\mathrm{s})}{\omega_\mathrm{Res}C} & \cos(\omega_\mathrm{Res}T_\mathrm{s}) & -\dfrac{\sin(\omega_\mathrm{Res}T_\mathrm{s})}{\omega_\mathrm{Res}C} \\ \dfrac{L_\mathrm{f}[1-\cos(\omega_\mathrm{Res}T_\mathrm{s})]}{L_\mathrm{t}} & \dfrac{\sin(\omega_\mathrm{Res}T_\mathrm{s})}{\omega_\mathrm{Res}L_\mathrm{f}} & \dfrac{L_\mathrm{G}+L_\mathrm{f}\cos(\omega_\mathrm{Res}T_\mathrm{s})}{L_\mathrm{t}} \end{bmatrix},$$

$$\mathbf{\Gamma}_\mathrm{inv} = \left(\int_0^{T_\mathrm{s}} \mathrm{e}^{\mathbf{A}\tau}\,\mathrm{e}^{-\mathrm{j}\omega_\mathrm{g}(T_\mathrm{s}-\tau)}\,\mathrm{d}\tau\right)\mathbf{B}_\mathrm{inv} = \begin{bmatrix} \gamma_\mathrm{inv1} \\ \gamma_\mathrm{inv2} \\ \gamma_\mathrm{inv3} \end{bmatrix} = \upsilon \begin{bmatrix} \dfrac{T_\mathrm{s}}{L_\mathrm{t}} + \dfrac{L_\mathrm{f}\sin(\omega_\mathrm{Res}T_\mathrm{s})}{\omega_\mathrm{Res}L_\mathrm{f}L_\mathrm{t}} \\ \dfrac{L_\mathrm{G}[1-\cos(\omega_\mathrm{Res}T_\mathrm{s})]}{L_\mathrm{t}} \\ \dfrac{T_\mathrm{s}}{L_\mathrm{t}} - \dfrac{\sin(\omega_\mathrm{Res}T_\mathrm{s})}{\omega_\mathrm{Res}L_\mathrm{t}} \end{bmatrix},$$

$$\mathbf{\Gamma}_\mathrm{g} = \left(\int_0^{T_\mathrm{s}} \mathrm{e}^{\mathbf{A}\tau}\,\mathrm{d}\tau\right)\mathbf{B}_\mathrm{g} = \begin{bmatrix} \gamma_\mathrm{g1} \\ \gamma_\mathrm{g2} \\ \gamma_\mathrm{g3} \end{bmatrix},$$

$$\gamma_\mathrm{g1} = \frac{\upsilon\left[-\omega_\mathrm{g}\omega_\mathrm{Res}\sin(\omega_\mathrm{Res}T_\mathrm{s}) + \mathrm{j}\omega_\mathrm{g}^2\cos(\omega_\mathrm{Res}T_\mathrm{s}) - \mathrm{j}\delta\right] - \mathrm{j}\omega_\mathrm{Res}^2}{\delta\,\omega_\mathrm{g}L_\mathrm{t}},$$

$$\gamma_\mathrm{g2} = \frac{\upsilon\left[\omega_\mathrm{Res}\cos(\omega_\mathrm{Res}T_\mathrm{s}) + \mathrm{j}\omega_\mathrm{g}\sin(\omega_\mathrm{Res}T_\mathrm{s})\right] - \omega_\mathrm{Res}}{\delta\omega_\mathrm{Res}L_\mathrm{G}C},$$

$$\gamma_\mathrm{g3} = \upsilon\frac{\omega_\mathrm{g}\omega_\mathrm{Res}L_\mathrm{f}\sin(\omega_\mathrm{Res}T_\mathrm{s}) - \mathrm{j}\delta L_\mathrm{G} - \mathrm{j}\omega_\mathrm{g}^2 L_\mathrm{f}\cos(\omega_\mathrm{Res}T_\mathrm{s})}{\delta\omega_\mathrm{g}L_\mathrm{G}L_\mathrm{t}} + \frac{\mathrm{j}\delta L_\mathrm{G} + \mathrm{j}\omega_\mathrm{g}^2 L_\mathrm{f}}{\delta\,\omega_\mathrm{g}L_\mathrm{G}L_\mathrm{t}},$$

$$\upsilon = \mathrm{e}^{-\mathrm{j}\omega_\mathrm{g}(T_\mathrm{s})},\ L_\mathrm{t} = L_\mathrm{f} + L_\mathrm{G},\ \delta = \omega_\mathrm{g}^2 - \omega_\mathrm{Res}^2. \tag{A.1}$$

$$C_1 = \gamma_{inv1}$$

$$C_2 = -R_{vir} \cdot \gamma_{inv1} \cdot \gamma_{inv3} - \gamma_{inv1} \cdot \phi_{22} - 2 \cdot \gamma_{inv1} \cdot \phi_{33} + \gamma_{inv2} \cdot \phi_{12} + \gamma_{inv3} \cdot \phi_{13}$$

$$\begin{aligned} C_3 = {} & R_{vir} \cdot \gamma_{inv1} \cdot \gamma_{inv3} \cdot \phi_{22} + R_{vir} \cdot \gamma_{inv1} \cdot \gamma_{inv3} \cdot \phi_{33} - R_{vir} \cdot \gamma_{inv2} \cdot \gamma_{inv3} \cdot \phi_{12} \\ & - R_{vir} \cdot \gamma_{inv3}^2 \cdot \phi_{13} + 2 \cdot \gamma_{inv1} \cdot \phi_{22} \cdot \phi_{33} - \gamma_{inv1} \cdot \phi_{23} \cdot \phi_{32} + \gamma_{inv1} \cdot \phi_{33}^2 - 2 \cdot \gamma_{inv2} \cdot \phi_{12} \cdot \phi_{33} \\ & + \gamma_{inv2} \cdot \phi_{13} \cdot \phi_{32} + \gamma_{inv3} \cdot \phi_{12} \cdot \phi_{23} - \gamma_{inv3} \cdot \phi_{13} \cdot \phi_{22} - \gamma_{inv3} \cdot \phi_{13} \cdot \phi_{33} \end{aligned}$$

$$\begin{aligned} C_4 = {} & \gamma_{inv1} \cdot \phi_{23} \cdot \phi_{32} \cdot \phi_{33} - \gamma_{inv2} \cdot \phi_{13} \cdot \phi_{32} \cdot \phi_{33} - \gamma_{inv3} \cdot \phi_{12} \cdot \phi_{23} \cdot \phi_{33} \\ & + \gamma_{inv3} \cdot \phi_{13} \cdot \phi_{22} \cdot \phi_{33} - \gamma_{inv1} \cdot \phi_{22} \cdot \phi_{33}^2 + \gamma_{inv2} \cdot \phi_{12} \cdot \phi_{33}^2 - R_{vir} \cdot \gamma_{inv3}^2 \cdot \phi_{12} \cdot \phi_{23} \\ & + R_{vir} \cdot \gamma_{inv3}^2 \cdot \phi_{13} \cdot \phi_{22} - R_{vir} \cdot \gamma_{inv1} \cdot \gamma_{inv3} \cdot \phi_{22} \cdot \phi_{33} + R_{vir} \cdot \gamma_{inv1} \cdot \gamma_{inv3} \cdot \phi_{23} \cdot \phi_{32} \\ & + R_{vir} \cdot \gamma_{inv2} \cdot \gamma_{inv3} \cdot \phi_{12} \cdot \phi_{33} - R_{vir} \cdot \gamma_{inv2} \cdot \gamma_{inv3} \cdot \phi_{13} \cdot \phi_{32} \end{aligned}$$

$$D_1 = R_{vir} \cdot \gamma_{inv1} - 2 \cdot R_{vir} \cdot \gamma_{inv3} - \phi_{11} - \phi_{22} - 2 \cdot \phi_{33}$$

$$\begin{aligned} D_2 = {} & -R_{vir}^2 \cdot \gamma_{inv1} \cdot \gamma_{inv3} + R_{vir}^2 \cdot \gamma_{inv3}^2 - R_{vir} \cdot \gamma_{inv1} \cdot \phi_{22} - R_{vir} \cdot \gamma_{inv1} \cdot \phi_{31} \\ & - 2 \cdot R_{vir} \cdot \gamma_{inv1} \cdot \phi_{33} + R_{vir} \cdot \gamma_{inv2} \cdot \phi_{12} - R_{vir} \cdot \gamma_{inv2} \cdot \phi_{32} + 2 \cdot R_{vir} \cdot \gamma_{inv3} \cdot \phi_{11} \\ & + R_{vir} \cdot \gamma_{inv3} \cdot \phi_{13} + 2 \cdot R_{vir} \cdot \gamma_{inv3} \cdot \phi_{22} + 2 \cdot R_{vir} \cdot \gamma_{inv3} \cdot \phi_{33} + \phi_{11} \cdot \phi_{22} + 2 \cdot \phi_{11} \cdot \phi_{33} \\ & - \phi_{12} \cdot \phi_{21} - \phi_{13} \cdot \phi_{31} + 2 \cdot \phi_{22} \cdot \phi_{33} - \phi_{23} \cdot \phi_{32} + \phi_{33}^2 \end{aligned}$$

$$\begin{aligned} D_3 = {} & R_{vir}^2 \cdot \gamma_{inv1} \cdot \gamma_{inv3} \cdot \phi_{22} + R_{vir}^2 \cdot \gamma_{inv1} \cdot \gamma_{inv3} \cdot \phi_{31} + R_{vir}^2 \cdot \gamma_{inv1} \cdot \gamma_{inv3} \cdot \phi_{33} \\ & - R_{vir}^2 \cdot \gamma_{inv2} \cdot \gamma_{inv3} \cdot \phi_{12} + R_{vir}^2 \cdot \gamma_{inv2} \cdot \gamma_{inv3} \cdot \phi_{32} - R_{vir}^2 \cdot \gamma_{inv3}^2 \cdot \phi_{11} - R_{vir}^2 \cdot \gamma_{inv3}^2 \cdot \phi_{13} \\ & - R_{vir}^2 \cdot \gamma_{inv3}^2 \cdot \phi_{22} - R_{vir} \cdot \gamma_{inv1} \cdot \phi_{21} \cdot \phi_{32} + R_{vir} \cdot \gamma_{inv1} \cdot \phi_{22} \cdot \phi_{31} + 2 \cdot R_{vir} \cdot \gamma_{inv1} \cdot \phi_{22} \cdot \phi_{33} \\ & - Rvir \cdot \gamma_{inv1} \cdot \phi_{23} \cdot \phi_{32} + R_{vir} \cdot \gamma_{inv1} \cdot \phi_{31} \cdot \phi_{33} + R_{vir} \cdot \gamma_{inv1} \cdot \phi_{33}^2 + R_{vir} \cdot \gamma_{inv2} \cdot \phi_{11} \cdot \phi_{32} \\ & - R_{vir} \cdot \gamma_{inv2} \cdot \phi_{12} \cdot \phi_{31} - 2 \cdot R_{vir} \cdot \gamma_{inv2} \cdot \phi_{12} \cdot \phi_{33} + R_{vir} \cdot \gamma_{inv2} \cdot \phi_{13} \cdot \phi_{32} \\ & + R_{vir} \cdot \gamma_{inv2} \cdot \phi_{32} \cdot \phi_{33} - 2 \cdot R_{vir} \cdot \gamma_{inv3} \cdot \phi_{11} \cdot \phi_{22} - 2 \cdot R_{vir} \cdot \gamma_{inv3} \cdot \phi_{11} \cdot \phi_{33} \\ & + 2 \cdot R_{vir} \cdot \gamma_{inv3} \cdot \phi_{12} \cdot \phi_{21} + R_{vir} \cdot \gamma_{inv3} \cdot \phi_{12} \cdot \phi_{23} - R_{vir} \cdot \gamma_{inv3} \cdot \phi_{13} \cdot \phi_{22} \\ & + R_{vir} \cdot \gamma_{inv3} \cdot \phi_{13} \cdot \phi_{31} - R_{vir} \cdot \gamma_{inv3} \cdot \phi_{13} \cdot \phi_{33}3 - 2 \cdot R_{vir} \cdot \gamma_{inv3} \cdot \phi_{22} \cdot \phi_{33} \\ & + R_{vir} \cdot \gamma_{inv3} \cdot \phi_{23} \cdot \phi_{32} - 2 \cdot \phi_{11} \cdot \phi_{22} \cdot \phi_{33} + \phi_{11} \cdot \phi_{23} \cdot \phi_{32} - \phi_{11} \cdot \phi_{33}^2 + 2 \cdot \phi_{12} \cdot \phi_{21} \cdot \phi_{33} \\ & - \phi_{12} \cdot \phi_{23} \cdot \phi_{31} - \phi_{13} \cdot \phi_{21} \cdot \phi_{32} + \phi_{13} \cdot \phi_{22} \cdot \phi_{31} + \phi_{13} \cdot \phi_{31} \cdot \phi_{33} - \phi_{22} \cdot \phi_{33}^2 + \phi_{23} \cdot \phi_{32} \cdot \phi_{33} \end{aligned}$$

$$\begin{aligned} D_4 = {} & -\phi_{11} \cdot \phi_{23} \cdot \phi_{32} \cdot \phi_{33} + \phi_{12} \cdot \phi_{23} \cdot \phi_{31} \cdot \phi_{33} + \phi_{13} \cdot \phi_{21} \cdot \phi_{32} \cdot \phi_{33} - \phi_{13} \cdot \phi_{22} \cdot \phi_{31} \cdot \phi_{33} \\ & - R_{vir} \cdot \gamma_{inv3} \cdot \phi_{11} \cdot \phi_{23} \cdot \phi_{32} - 2 \cdot R_{vir} \cdot \gamma_{inv3} \cdot \phi_{12} \cdot \phi_{21} \cdot \phi_{33} + R_{vir} \cdot \gamma_{inv3} \cdot \phi_{12} \cdot \phi_{23} \cdot \phi_{31} \\ & - R_{vir} \cdot \gamma_{inv3} \cdot \phi_{12} \cdot \phi_{23} \cdot \phi_{33} + R_{vir} \cdot \gamma_{inv3} \cdot \phi_{13} \cdot \phi_{21} \cdot \phi_{32} - R_{vir} \cdot \gamma_{inv3} \cdot \phi_{13} \cdot \phi_{22} \cdot \phi_{31} \\ & + R_{vir} \cdot \gamma_{inv3} \cdot \phi_{13} \cdot \phi_{22} \cdot \phi_{33} + R_{vir}^2 \cdot \gamma_{inv1} \cdot \gamma_{inv3} \cdot \phi_{21} \cdot \phi_{32} - R_{vir}^2 \cdot \gamma_{inv1} \cdot \gamma_{inv3} \cdot \phi_{22} \cdot \phi_{31} \\ & - R_{vir}^2 \cdot \gamma_{inv1} \cdot \gamma_{inv3} \cdot \phi_{22} \cdot \phi_{33} + R_{vir}^2 \cdot \gamma_{inv1} \cdot \gamma_{inv3} \cdot \phi_{23} \cdot \phi_{32} - R_{vir}^2 \cdot \gamma_{inv2} \cdot \gamma_{inv3} \cdot \phi_{11} \cdot \phi_{32} \\ & + R_{vir}^2 \cdot \gamma_{inv2} \cdot \gamma_{inv3} \cdot \phi_{12} \cdot \phi_{31} + R_{vir}^2 \cdot \gamma_{inv2} \cdot \gamma_{inv3} \cdot \phi_{12} \cdot \phi_{33} - R_{vir}^2 \cdot \gamma_{inv2} \cdot \gamma_{inv3} \cdot \phi_{13} \cdot \phi_{32} \\ & + R_{vir} \cdot \gamma_{inv1} \cdot \phi_{21} \cdot \phi_{32} \cdot \phi_{33} - R_{vir} \cdot \gamma_{inv1} \cdot \phi_{22} \cdot \phi_{31} \cdot \phi_{33} + R_{vir} \cdot \gamma_{inv1} \cdot \phi_{23} \cdot \phi_{32} \cdot \phi_{33} \\ & - R_{vir} \cdot \gamma_{inv2} \cdot \phi_{11} \cdot \phi_{32} \cdot \phi_{33} + R_{vir} \cdot \gamma_{inv2} \cdot \phi_{12} \cdot \phi_{31} \cdot \phi_{33} - R_{vir} \cdot \gamma_{inv2} \cdot \phi_{13} \cdot \phi_{32} \cdot \phi_{33} \\ & + 2 \cdot R_{vir} \cdot \gamma_{inv3} \cdot \phi_{11} \cdot \phi_{22} \cdot \phi_{33} + R_{vir}^2 \cdot \gamma_{inv3}^2 \cdot \phi_{11} \cdot \phi_{22} - R_{vir}^2 \cdot \gamma_{inv3}^2 \cdot \phi_{12} \cdot \phi_{21} \\ & - R_{vir}^2 \cdot \gamma_{inv3}^2 \cdot \phi_{12} \cdot \phi_{23} + R_{vir}^2 \cdot \gamma_{inv3}^2 \cdot \phi_{13} \cdot \phi_{22} - R_{vir} \cdot \gamma_{inv1} \cdot \phi_{22} \cdot \phi_{33}^2 \\ & + R_{vir} \cdot \gamma_{inv2} \cdot \phi_{12} \cdot \phi_{33}^2 - \phi_{12} \cdot \phi_{21} \cdot \phi_{33}^2 + \phi_{11} \cdot \phi_{22} \cdot \phi_{33}^2 \end{aligned} \tag{A.2}$$

9.2. Dynamic Plots

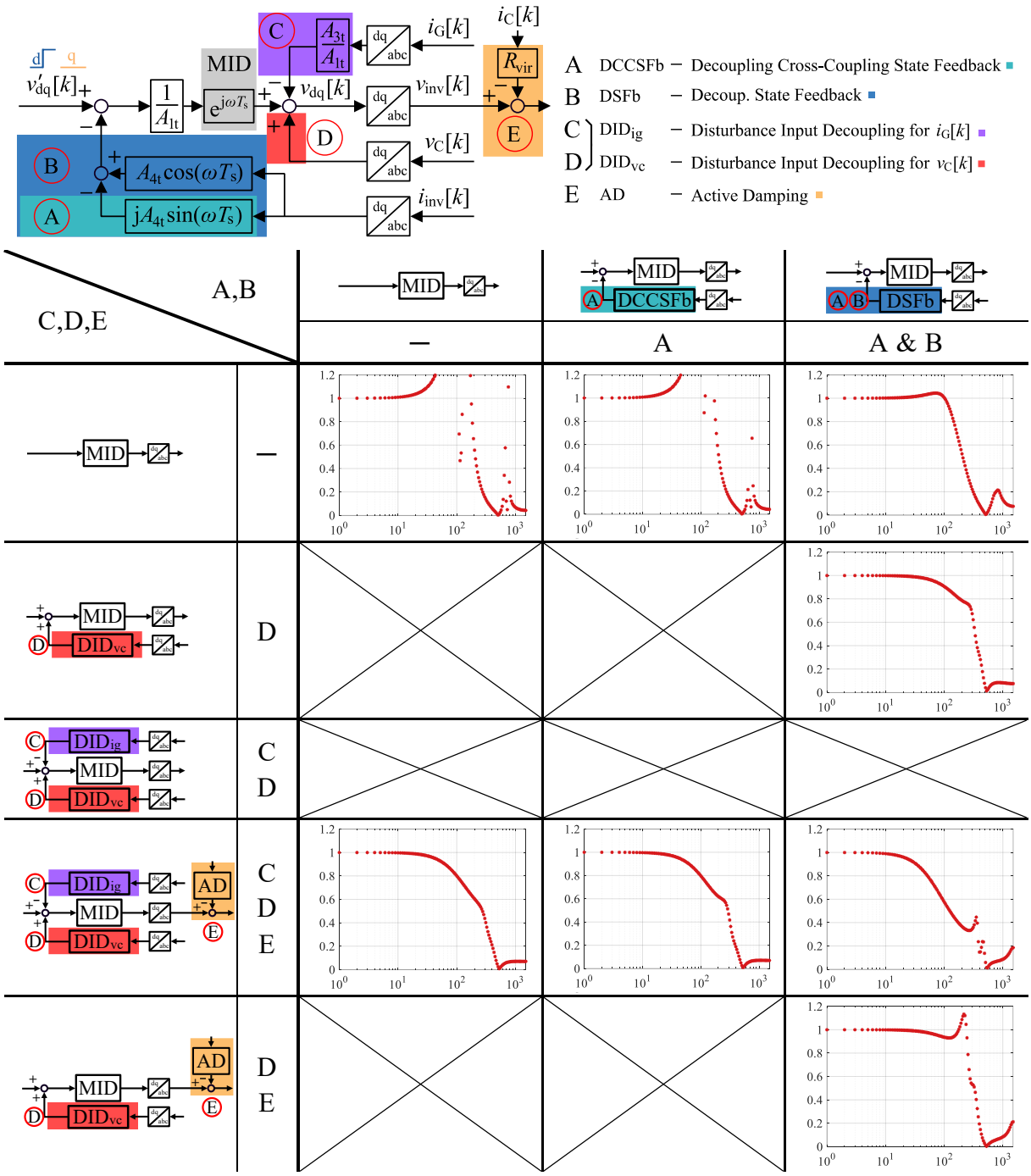

Figure 9.1: Closed-loop current control command tracking plots of the LC-filter plant with various decoupling techniques: A – decoupling cross-coupling state feedback, B – full decoupling state feedback, C – disturbance input decoupling for the grid current, D – disturbance input decoupling for the capacitor voltage, and E – active damping implementation; y-axis is the d-current reference over measurement, x-axis is the frequency in Hz. Crossed-out sections did not yield stable operation.

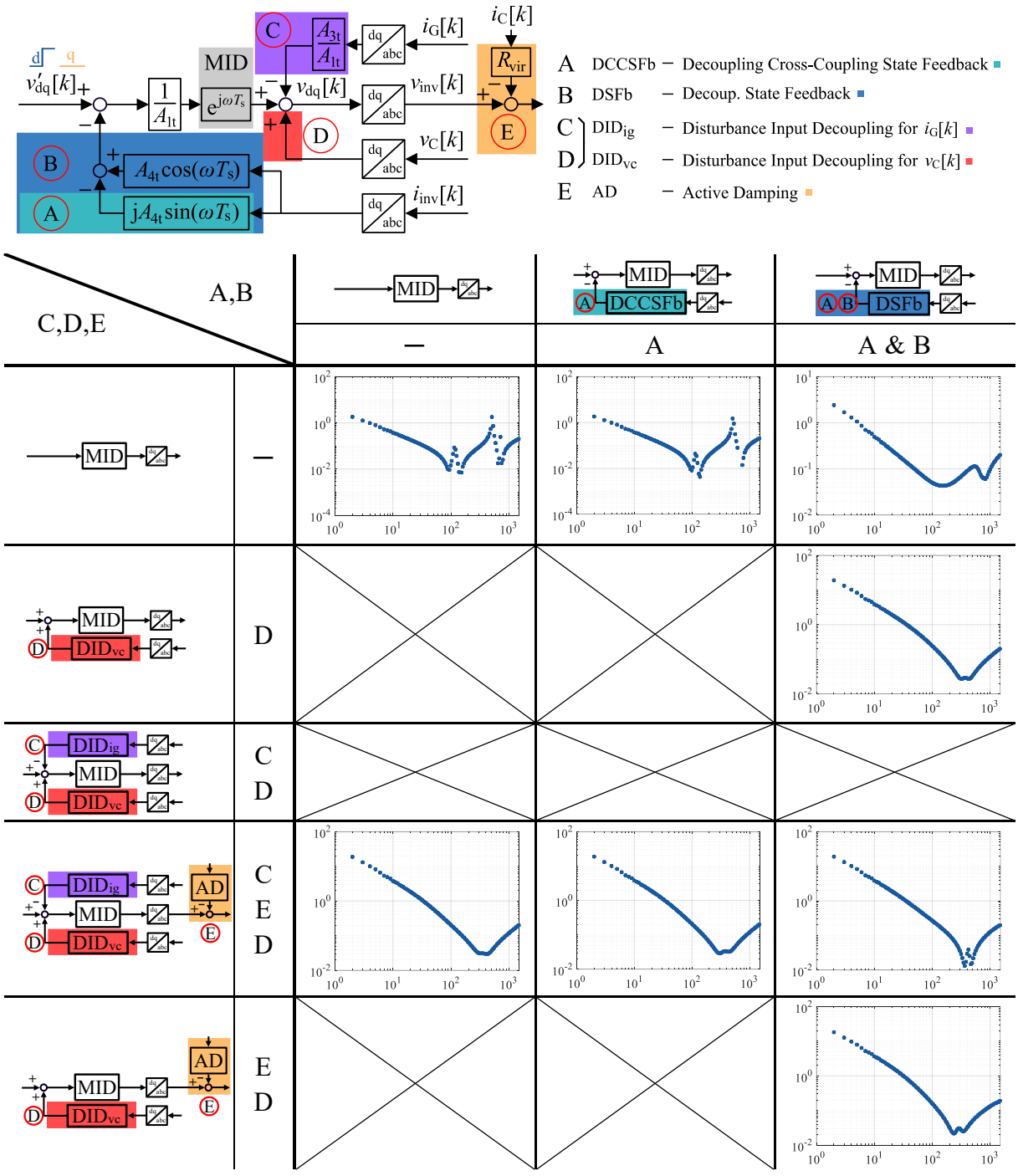

Figure 9.2: Closed-loop dynamic stiffness plot of the LC-filter plant with various decoupling techniques: A – decoupling cross-coupling state feedback, B – full decoupling state feedback, C – disturbance input decoupling for the grid current, D – disturbance input decoupling for the capacitor voltage, and E – active damping implementation; y-axis is the d-component of the disturbance voltage over the measured d-axis current in Ω, x-axis is the frequency in Hz. Crossed-out sections did not yield stable operation.

9.3. Additional Block-Diagrams

Non-complex decoupling techniques for continuous current control with plant:

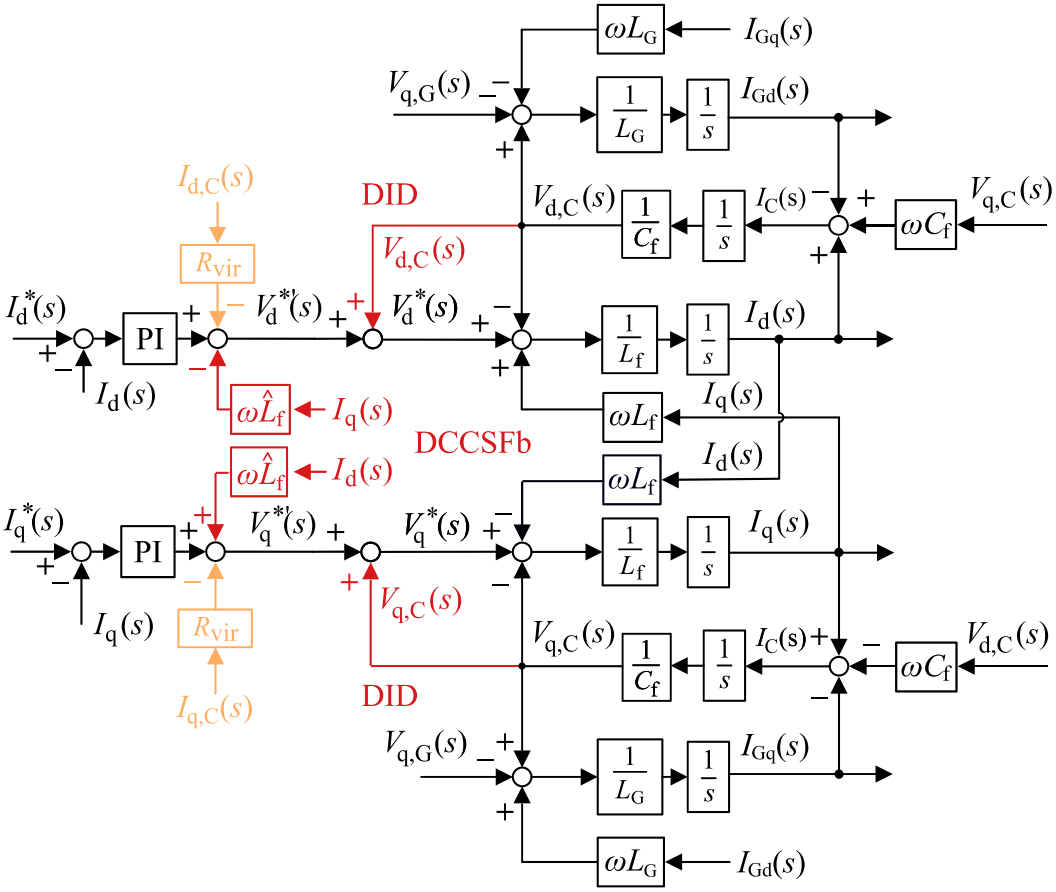

Figure 9.3: Control techniques with active damping for the LC-topology with voltage decoupling (DID – red) and virtual resistor implementation (R_{vir} – orange).

Non-complex decoupling techniques for discrete current control:

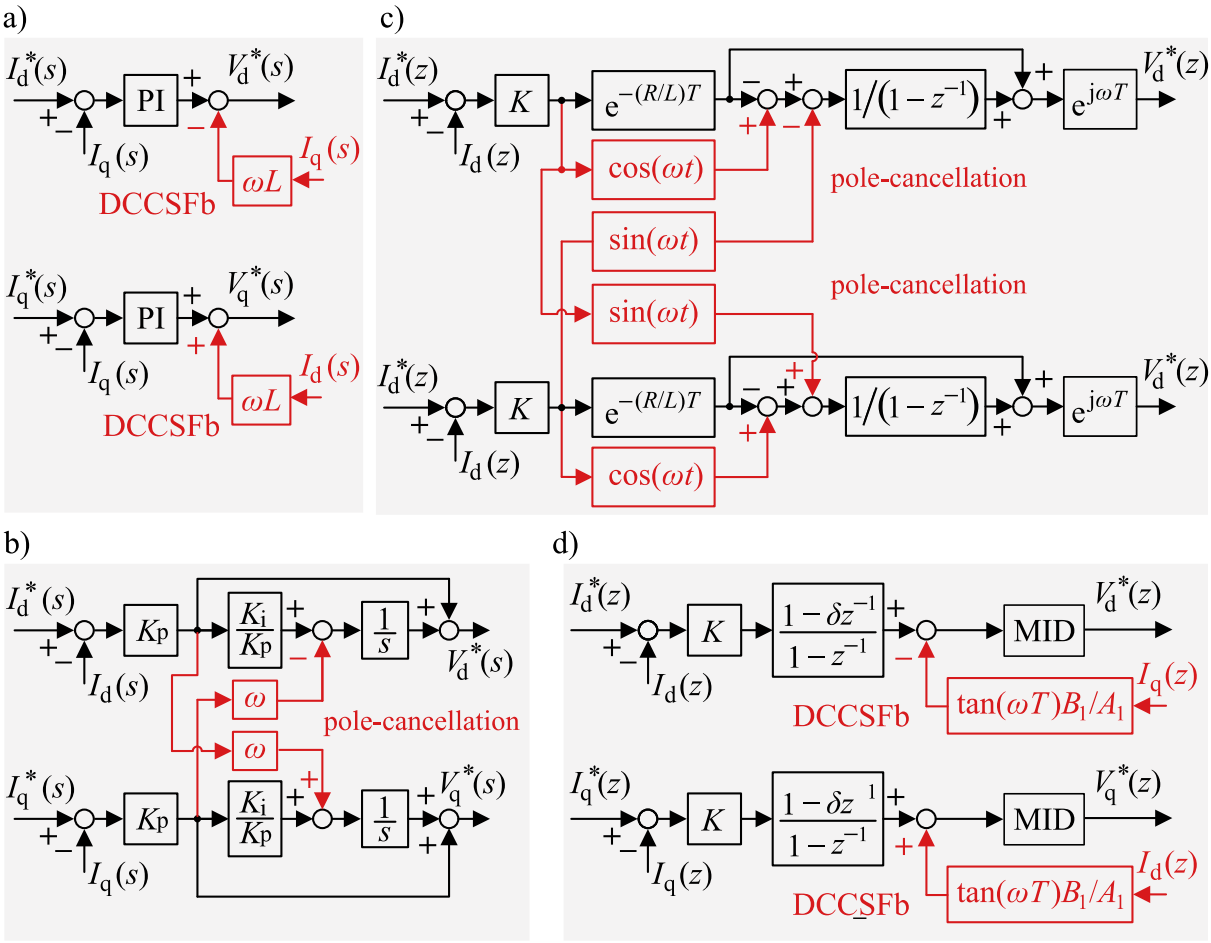

Figure 9.4: Decoupling techniques of the dq-current cross-coupling: a) continuous decoupling cross-coupling via active state feedback (DCCSFb) [26], b) continuous pole-cancelation via complex zero in the forward path [26], c) discrete decoupling cross-coupling (DCCSFb) w/ MID – *Manipulated Input Decoupling* [23] (connected to this work), d) discrete pole-cancelation via complex zero in the forward path [19]. The complex representation is shown in Figure 2.6.

Complex-formated and more compact representation of the overall control design with active damping and delay compensation via observers:

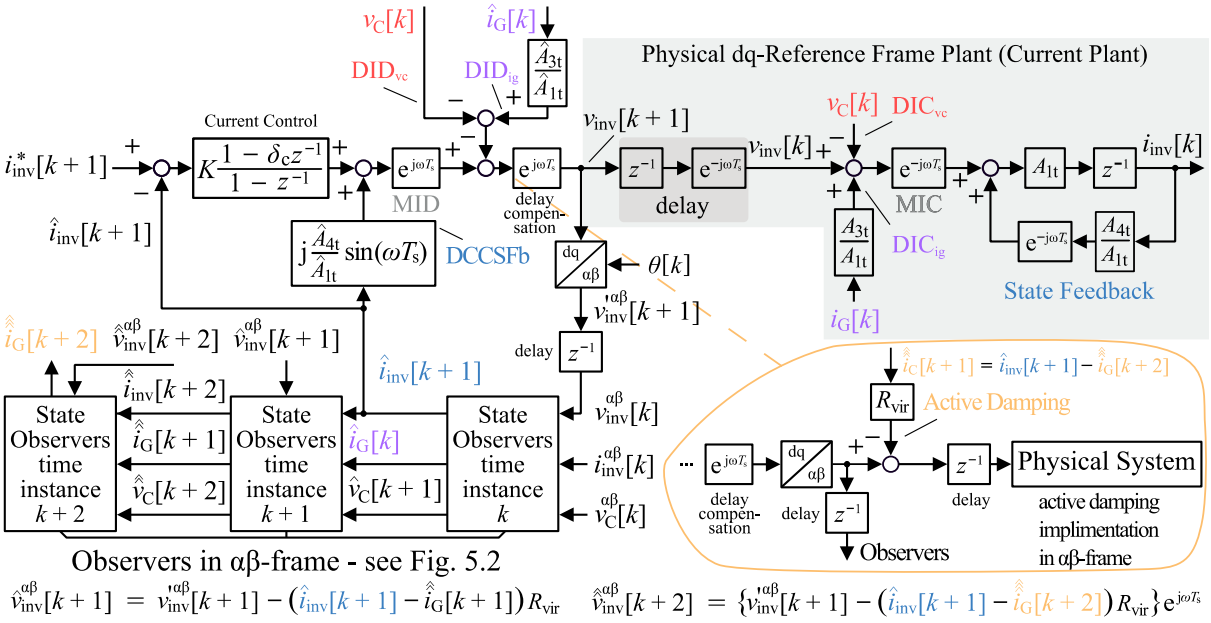

Figure 9.5: Block diagram of the current control structure with delay compensation via a cascaded Luenberger-style observer structure with active damping implementation and decoupling techniques: DCCSFb – Decoupling Cross-Coupling State Feedback, DID – Disturbance Input Decoupling (index: vc – capacitor voltage, ig – grid-current). A non-complex and more detaild version is displayed in Figure 5.4.

9.4. Simulation for the Pre-charge Resistor

Figure 9.6 shows the test results of the simulation of the start-up with pre-charge resistors for the filter capacitor. Using a very low pre-charge resistor (0.5 Ω) leads to roughly 1.5 times nominal current and voltage. The over-current would most likely not damage any components. However, the over-voltage could potentially charge up the DC-link. The critical limit of the DC-link voltage is the breakdown voltage of the transistors, which can be well below 1.5 times the nominal value. Choosing a very high resistance for the pre-charge, on the other hand, will excite the resonance too strongly after the bypassing, which yields two times nominal current and voltage in the case of 50 Ω. The optimal resistance (approx. 5 Ω for the test bench) keeps all overshoots in a tolerable band.

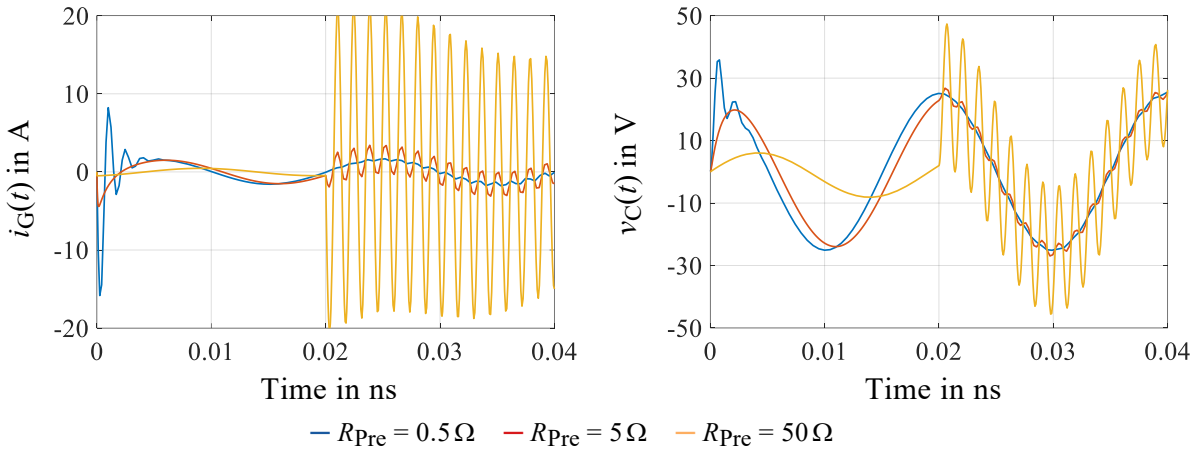

Figure 9.6: Simulation: Pre-charge resistor iterative test for the start-up. The contactor bypasses the pre-charge resistor at $t = 0.02$ s. $R_{Pre} = 5$ Ω leads to the lowest overshoots for voltage and current within a tolerable band.

9.5. Optimization Algorithm Example for Inductor Scaling

1. Search for Minimum of $V_{Fe.m} \cdot \delta_x$

   With limits:: $\delta_{lFe} < 30$, $\delta_N < 21$, $\delta_{Fe} = 4$ .. 16, $\delta_W = 4$ .. 50, $n_i = 450$ .. 1900, $n_u = 27$

   Results: $\delta_{Fe} = 4$, $\delta_W = 16$, $n_i = 670$ ($I_d = 6.7$ A), & $n_u = 27$ ($V_d = 25$ V)

   → $\boxed{\delta_{lFe} = 26\ ,\ \delta_x = 41}$

   ➔ $l_{Fe} = 6$ cm, $r_{Fe} = 4$ cm, $r_W = 1.5$ mm, $N = 12$

2. Search for Minimum of $V_{Fe.m} \cdot \delta_x$

   With limits: $\delta_{lFe} < 30$, $\delta_N < 21$, $\delta_{Fe} = 4$ .. 16, $\delta_W = 4$ .. 50, $n_i = 450$ .. 1900, $n_u = 27$ .. 50

   Results: $\delta_{Fe} = 4$, $\delta_W = 13$, $n_i = 480$ ($I_d = 9.4$ A), & $n_u = 40$ ($V_d = 17$ V)

   → $\boxed{\delta_{lFe} = 30\ ,\ \delta_x = 34}$

   ➔ $l_{Fe} = 5$ cm, $r_{Fe} = 4$ cm, $r_W = 1.8$ mm, $N = 9$

3. Search for Minimum of $V_{Fe.m} \cdot \delta_x$

   With limits: $\delta_{lFe} < 30$, $\delta_N < 21$, $\delta_{Fe} = 4$ .. 16, $\delta_W = 4$ .. 50, $n_i = 450$, $n_u = 27$

   Results: $\delta_{Fe} = 4$, $\delta_W = 13$, $n_i = 470$ ($I_d = 10$ A), & $n_u = 27$ ($V_d = 25$ V)

   → $\boxed{\delta_{lFe} = 21\ ,\ \delta_x = 34}$

   ➔ $l_{Fe} = 7.2$ cm, $r_{Fe} = 4$ cm, $r_W = 1.8$ mm, $N = 13$

9.6. Steinmetz Parameters of Magnetic Material

RTP – iron powder

RTF – ferrite

RTN – nanocrystalline

TABLE A.2
VALUES OF EXAMPLE STEINMETZ PARAMETERS

Core material	RTP		RTF		RTN	
Source / type	(-26) [100]	[101]	F867 [100]	[101]	M-070 [100]	[101]
K [$\mathrm{W \cdot s^{\alpha}/T^{\beta}/m^3}$]	103	103	10.76	2.76	2	0.05
α	1.15	1.15	1.24	1.24	1.69	1.69
β	2.07	2.07	2.28	2.28	2.2	2.2

- RTN low losses at low frequencies
- RTP and RTF better at higher frequencies
- RTP has lower losses at extremely high frequencies

Iron loss scaling from RTN to RTF for example of source [100]:

$$\frac{P_{\mathrm{Fe.RTN}}}{P_{\mathrm{Fe.RTF}}} = \frac{V_{\mathrm{Fe.RTN}}}{V_{\mathrm{Fe.RTF}}} \cdot \frac{K_{\mathrm{Fe.RTN}}}{K_{\mathrm{Fe2.RTF}}} \cdot f^{\alpha_{\mathrm{RTN}} - \alpha_{\mathrm{RTF}}} \cdot \Delta B^{\beta_{\mathrm{RTN}} - \beta_{\mathrm{RTF}}} \tag{A.3}$$

At resonance (1 kHz):

$$\frac{P_{\mathrm{Fe.RTN}}}{P_{\mathrm{Fe.RTF}}} = 4.16 \cdot \frac{V_{\mathrm{Fe.RTN}}}{V_{\mathrm{Fe2.RTF}}} \Delta B^{-0.08} \tag{A.4}$$

For the same volume:

$$\frac{P_{\mathrm{Fe.RTN}}}{P_{\mathrm{Fe.RTF}}} = 4.16 \cdot \Delta B^{-0.08} \tag{A.5}$$

$$\text{For } \Delta B < 55 \text{ MT: } P_{\mathrm{Fe.RTN}} > P_{\mathrm{Fe.RTF}} \tag{A.6}$$

Iron loss scaling at resonance (1 kHz) from RTF to RTP for example of source [100]:

$$\frac{P_{\mathrm{Fe.RTF}}}{P_{\mathrm{Fe.RTP}}} = \frac{V_{\mathrm{Fe.RTF}}}{V_{\mathrm{Fe.RTP}}} \cdot \frac{K_{\mathrm{Fe.RTF}}}{K_{\mathrm{Fe2.RTP}}} \cdot f^{\alpha_{\mathrm{RTF}} - \alpha_{\mathrm{RTP}}} \cdot \Delta B^{\beta_{\mathrm{RTF}} - \beta_{\mathrm{RTP}}} \tag{A.7}$$

At resonance (1 kHz):

$$\frac{P_{\text{Fe.RTF}}}{P_{\text{Fe.RTP}}} = 0.1934 \cdot \frac{V_{\text{Fe.RTF}}}{V_{\text{Fe.RTP}}} \Delta B^{0.21} \tag{A.8}$$

For the same volume:

$$\frac{P_{\text{Fe.RTF}}}{P_{\text{Fe.RTP}}} = 0.1934 \cdot \Delta B^{0.21} \tag{A.9}$$

$$\text{For } \Delta B > 2.5 \text{ kT: } P_{\text{Fe.RTF}} > P_{\text{Fe.RTP}} \tag{A.10}$$

Iron loss scaling at resonance (1 kHz) from RTN to RTP for example of source [100]:

$$\frac{P_{\text{Fe.RTN}}}{P_{\text{Fe.RTP}}} = \frac{V_{\text{Fe.RTN}}}{V_{\text{Fe.RTP}}} \cdot \frac{K_{\text{Fe.RTN}}}{K_{\text{Fe2.RTP}}} \cdot f^{\alpha_{\text{RTN}} - \alpha_{\text{RTP}}} \cdot \Delta B^{\beta_{\text{RTN}} - \beta_{\text{RTP}}} \tag{A.11}$$

At resonance (1 kHz):

$$\frac{P_{\text{Fe.RTN}}}{P_{\text{Fe.RTP}}} = 0.81 \cdot \frac{V_{\text{Fe.RTN}}}{V_{\text{Fe.RTP}}} \Delta B^{0.13} \tag{A.12}$$

For the same volume:

$$\frac{P_{\text{Fe.RTN}}}{P_{\text{Fe.RTP}}} = 0.81 \cdot \Delta B^{0.13} \tag{A.13}$$

$$\text{For } \Delta B > 5 \text{ T: } P_{\text{Fe.RTN}} > P_{\text{Fe.RTP}} \tag{A.14}$$

These materials have saturation limits between 500 mT to 1.5 T. Further, the harmonics at high frequencies due to switching and resonances do not feature magnetic flux density values of the same order of magnitude as the fundamental 50 Hz. Thus, much lower ΔB is expected. Therefore, RTFs feature the lowest damping at the resonant frequency. RTPs feature lower losses (damping) at these high frequencies than RTNs.

9.7. Additional Experimental Setup Pictures

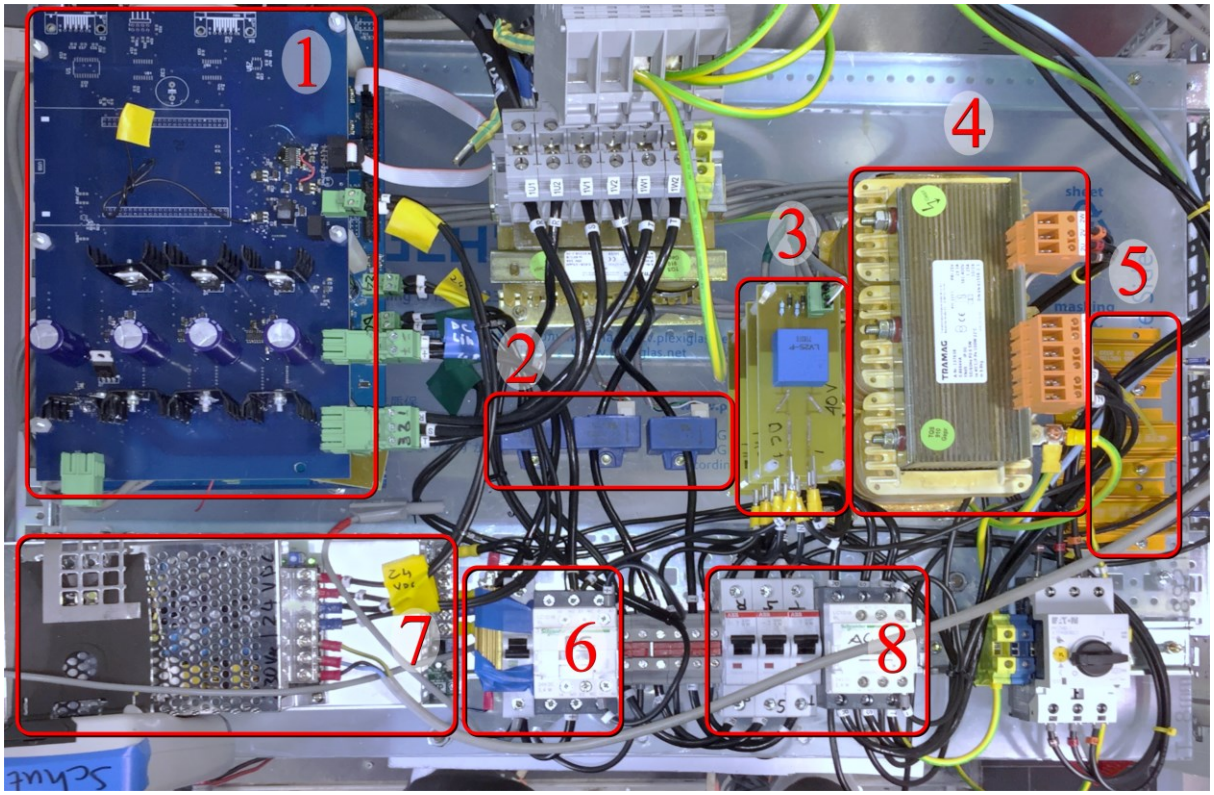

1 – Inverter board stacked on controller board	4 – transformer	7 – voltage power supply
2 – current measurement	5 – pre-charge resistor for filter-C	8 – contactor and MCB (protection)
3 – voltage measurement	6 – contactor and pre-charge resistor for DC-link	

Figure 9.7: Picture of the laboratory scaled 25 V low-power test bench – inverter, controller, and peripherals.

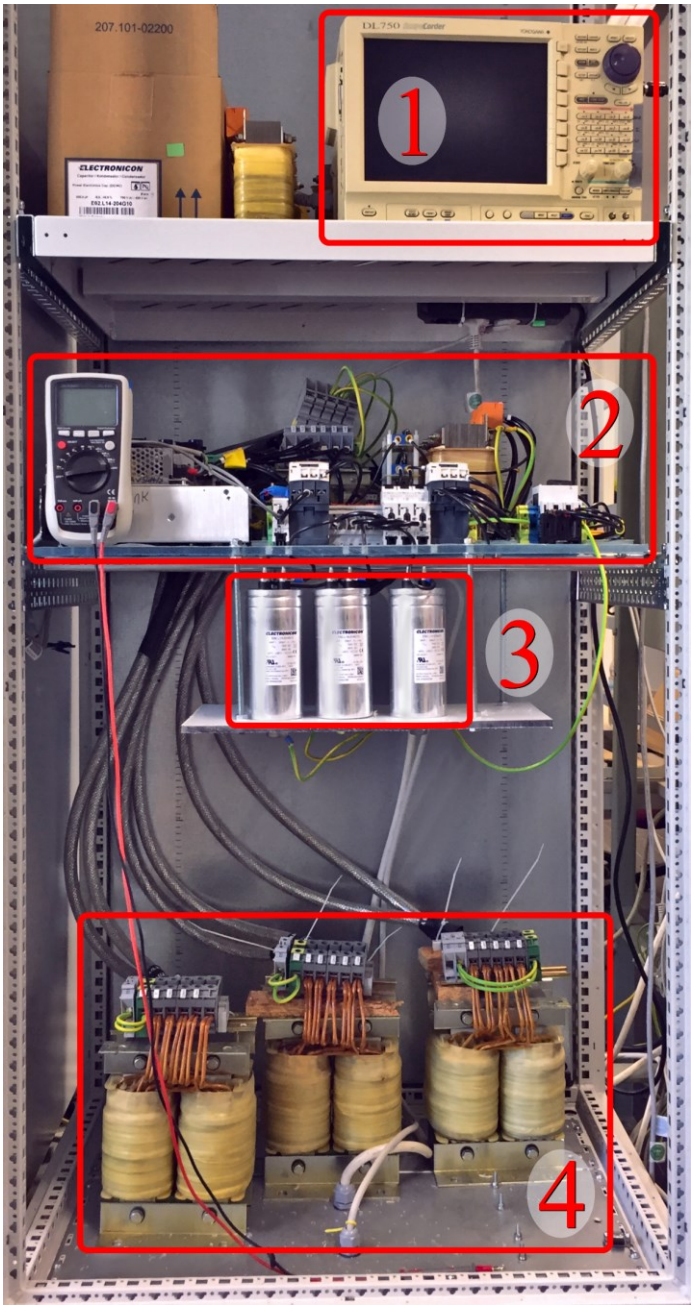

1 – Oscilloscope
2 – inverter, controller, and peripherals (Figure 9.6)
3 – Filter capacitors
4 – Filter inductors

Figure 9.8: Picture of the entire laboratory scaled 25 V low-power test bench (see Figure 6.1).

9.8. Reference Paper Active Damping – Gap in Literature

TABLE A.3
REFERENCE PAPER FOR ACTIVE DAMPING (ANALYSIS OF GAPS/ISSUES)

	f_R(kHz)	f_s(kHz)	f_s/f_R	SFb-based	Forward-path	Modelling technique	Delay modelling	Delay comp.	Experiment
[7]	1.22	3.5/5/7	4 – 2	no	Notch-Filter	quasi-continuous + discrete	yes	no	yes
[10]	?	?	?	i_c	no	quasi-continuous	no	no	no
[14]	0.3 - 0.35	5	14.2	HPF v_c	no	quasi-continuous	no	no	no
[18]	2.96	12	4.1 · 2	i_{inv} ·G_{lead} ·$G_{ad}(s)$	no	quasi-continuous	yes	yes	yes
[9]	3.3	12.8	3.8	i_{inv}	no	Discrete (approx.)	yes	no	yes
[5]	Damping resistor turned on & off (8 Diodes and 1 or 2 Switches)								
[17]	0.71	3	4.2	no	Resonant Control	quasi-continuous	no	no	no
[15]	1.8	5	3.8	HPF v_c	no	quasi-continuous	yes	no	yes
[8]	3.5	10	2.8	i_c	Notch-Filter	quasi-continuous	no	no	yes
[4]	Passive resistor for damping								
[13]	3.5	20	5.7	i_c	no	quasi-continuous	no	no	no
[12]	7	20	2.8	no	Notch-Filter	quasi-continuous	no	no	no
[6]	1.4	10	7.1	i_c (obs.)	no	quasi-continuous	yes	no	no
[16]	7	?	?	i_c, $v_{c,lag}$	no	quasi-continuous	no	no	no

Theses

1. The LCL resonance plant can be actively damped without information of the grid impedance within certain limits

2. Proper phase information of the states of the plant are of the essence. Otherwise the active damping will not be effective. Filtering and delays in the system distort the phase information significantly.

3. Observers can be utilized to compensate for delays.

4. The modelling and control design in the continuous domain help to give insights to the behavior and limits of the physical system. Solution approaches and conclusion can be drawn from these insights.

5. The continuous design and the consequent evaluation process cannot guarantee proper perfomance in a DSP-based application

6. The work illustrates a reduced order direct discrete modelling approach of the LC plant.

7. The real system with all inherent delays and implemented filters has to be taken into account for the simulation results to be meaningfull.

8. The timing and frequency of the sampling highly influence the performance, the limits, and consequently the feasibility of the envisaged system.

9. Inductive components scale down in power poorly. In the low-voltage test bench, the inductive components become much more resistive in comparison to the high-power original setup.

10. The harmonic impedance seen from the grid (dynamic stiffness) is the most important metric for design of control and evaluation of performance. This statement is especially true for active damping. This metric further provides information about passivity.

11. Notch-filter based active damping performs bad. This is very apperent in the dynamic stiffness. The state information is missing and thus very low to no dynamic stiffness is achieved at the resonance.

12. The active damping coefficient has to be chosen carefully. Too little values result in small impact. Whereas, too big damping coefficients yield to strong eigenvalue movement and thus destabalize the system.

13. Proper discrete decoupling techniques are of the essence to handle the higher-order plant (compared to L-Filter) with high dynamic performance.